AD-A109 945 SCIENCE APPLICATIONS INC IRVINE CA MATERIAL SCIENCES--ETC F/G 16/3
PERFORMANCE TECHNOLOGY PROGRAM (PTP-S II). VOLUME VI. A STATIST--ETC(U)
AUG 80 R B DIRLING F04701-77-C-0126
UNCLASSIFIED SAI-061-81-05-06 BMO-TR-80-53 NL

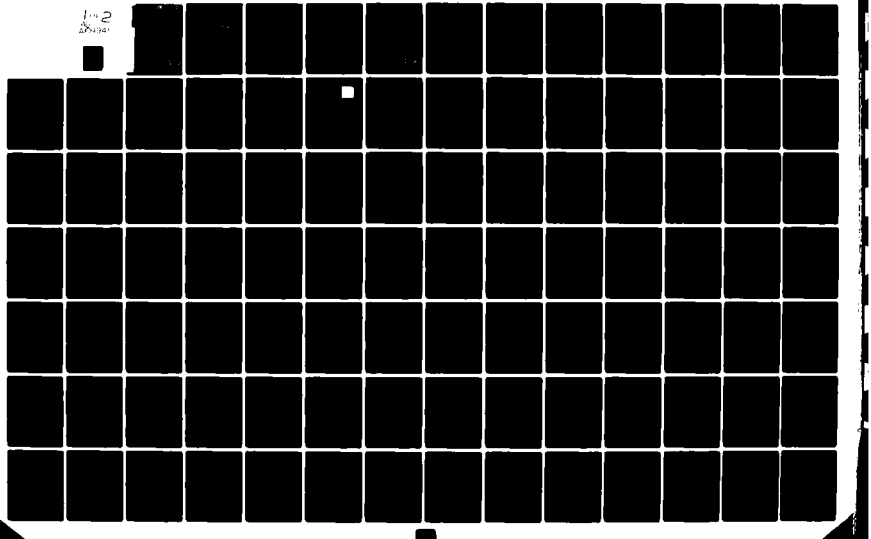

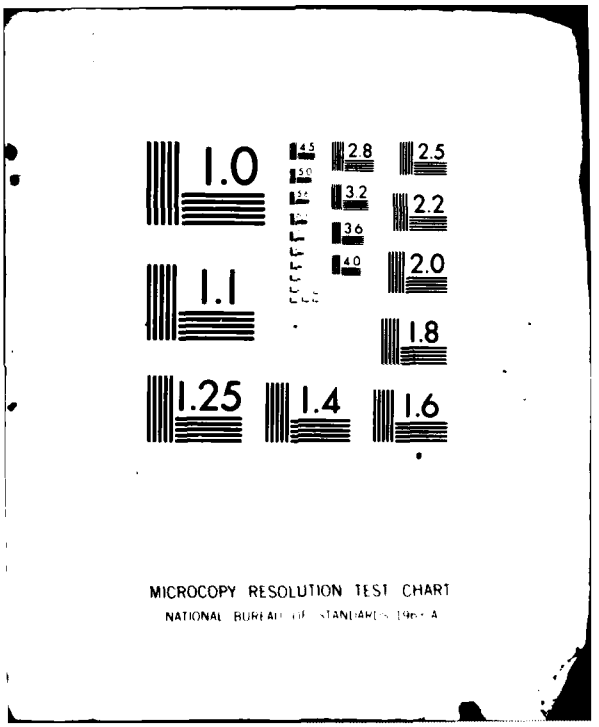
1.0
1.1
1.25
1.4
1.6
1.8
2.0
2.2
2.5
2.8
3.2
3.6
4.0
4.5
5.0
MICROCOPY RESOLUTION TEST CHART
NATIONAL BUREAU OF STANDARDS 1963-A

LEVEL II

BMO TR-80-53

SAI DOCUMENT NO. SAI-061-81-05-06

PERFORMANCE TECHNOLOGY PROGRAM (PTP-S II)

VOLUME VI.

A STATISTICAL MODEL OF NOSETIP SHAPE CHANGE FOR REENTRY VEHICLES.

SCIENCE APPLICATIONS, INC.
MATERIAL SCIENCES OPERATION
IRVINE, CALIFORNIA 92715

AUGUST, 1980

FINAL REPORT FOR PERIOD DECEMBER 1977 - SEPTEMBER 1979

CONTRACT NO. F04701-77-C-0126

AIR FORCE BALLISTIC MISSILE OFFICE
NORTON AIR FORCE BASE, CALIFORNIA 92409

NOTICE

This final report was submitted by Science Applications, Inc., 1200 Prospect Street, La Jolla, California 92037, under Contract Number F04701-77-C-0126, with the Ballistic Missile Office, AFSC, Norton AFB, California 92409. Major Kevin E. Yelmgren, BMO/MNRTE, was the Project Officer in charge. This technical report has been reviewed and is approved for publication.

Kevin E. Yelmgren

KEVIN E. YELMGREN, Major, USAF
Chief, Vehicle Technology Branch
Advanced Ballistic Reentry Systems

RICHARD W. SMITH, Colonel, USAF
Chief, Reentry Technology Division
Advanced Ballistic Reentry Systems

SECURITY CLASSIFICATION OF THIS PAGE *(When Data Entered)*

REPORT DOCUMENTATION PAGE

READ INSTRUCTIONS BEFORE COMPLETING FORM

1. REPORT NUMBER: BMO-TR-80-53	2. GOVT ACCESSION NO.: AD-A109945
3. RECIPIENT'S CATALOG NUMBER:	
4. TITLE *(and Subtitle)*: PERFORMANCE TECHNOLOGY PROGRAM (PTP-SII) Vol. VI, A Statistical Model of Nosetip Shape Change for Reentry Vehicles	5. TYPE OF REPORT & PERIOD COVERED: Final Report for Dec. 1977 - Sept. 1979
	6. PERFORMING ORG. REPORT NUMBER: SAI-061-81-05-06
7. AUTHOR(s): R. B. Dirling, Jr.	8. CONTRACT OR GRANT NUMBER(s): F04701-77-C-0126
9. PERFORMING ORGANIZATION NAME AND ADDRESS: Science Applications, Inc. 18872 Bardeen Ave. Irvine, California 92715	10. PROGRAM ELEMENT, PROJECT, TASK AREA & WORK UNIT NUMBERS:
11. CONTROLLING OFFICE NAME AND ADDRESS: Ballistic Missile Office Norton AFB, California 92409	12. REPORT DATE: August 1980
	13. NUMBER OF PAGES: 154
14. MONITORING AGENCY NAME & ADDRESS *(if different from Controlling Office)*:	15. SECURITY CLASS. *(of this report)*: Unclassified
	15a. DECLASSIFICATION DOWNGRADING SCHEDULE:

16. DISTRIBUTION STATEMENT *(of this Report)*

Approved for Public Release; Distribution Unlimited.

17. DISTRIBUTION STATEMENT *(of the abstract entered in Block 20, if different from Report)*

18. SUPPLEMENTARY NOTES

19. KEY WORDS *(Continue on reverse side if necessary and identify by block number)*

Reentry Vehicle
Nosetip
Shape Change
Asymmetric
Roll-Trim
Accuracy
Statistical

20. ABSTRACT *(Continue on reverse side if necessary and identify by block number)*

An analytical model capable of describing the asymmetric shape change of reentry vehicle nosetips during atmospheric entry is described. The analysis method is suitable for inclusion in a larger simulation model for the calculation of vehicle aerodynamics, trajectory, and impact point dispersion. The method employs Monte Carlo simulation of statistical distributions of roughness element sizes on the nosetip material in order to predict asymmetric transition front behavior and the resulting asymmetric nosetip shape change. Correlations of reentry vehicle flight test data and the results of selected parametric studies are also presented.

DD FORM 1 JAN 73 1473 EDITION OF 1 NOV 65 IS OBSOLETE

4 1-701

SECURITY CLASSIFICATION OF THIS PAGE *(When Data Entered)*

PREFACE

This report was prepared by Science Applications, Inc. (SAI), Irvine, California for the Space and Missile Systems Organization (SAMSO), El Segundo, California, under Contract No. F04701-77-C-0126. It is the final report describing work performed from 1 December 1977 to 29 September 1979 on the analytical modeling of asymmetrical nosetip shape change of reentry vehicles. Capts. E. Taylor and R. Chambers of SAMSO and Dr. R. Bishop of Aerospace provided technical direction for the Air Force. Their contributions to this study are gratefully acknowledged.

Mr. R. Dirling, Jr. was the SAI Principal Investigator for this effort. The principal contributors to the work were Mr. Dirling and Mr. Moreno White who provided analysis of arc-jet ablation test data.

TABLE OF CONTENTS

LIST OF FIGURES

LIST OF FIGURES (cont.)

LIST OF FIGURES (cont.)

LIST OF TABLES

NOMENCLATURE

a	nosetip indented ray parameter defined by Eq. (7), in
A^*	subsonic flow region area, in^2
b	nosetip indented ray parameter defined by Eq. (15)
B'	normalized blowing rate, $\dot{m}/\rho_e u_e C_H$
c_f	skin friction coefficient
C_H	Stanton number
f_1	geometric function defined by Eq. (50)
f_2	function defined by Eq. (96)
f_a	bow shock proximity influence function defined by Eq. (64)
f_e	entropy swallowing influence function defined by Eq. (58)
f_θ	severely intended ray influence function defined by Eq. (59)
H	gas enthalpy, Btu/lbm
k	roughness height, mil
$\bar{k}$	nosetip mean roughness height, mil
k_L	average material laminar roughness height, mil
k_s	equivalent sand roughness, mil
ℓ	distance from stagnation point to geometric center, in
$\dot{m}$	mass loss rate, lbm/ft^2-sec
P	gas pressure, lbf/ft^2
$\tilde{Q}$	integrated heating defined by Eq. (44), $psf^{\frac{1}{2}}$-s-Btu/lbm-$in^{\frac{1}{2}}$
r	radial distance from Z axis, in

R_1	stagnation region radius of curvature, in
R_2	indentation region radius of curvature, in
R_{max}	maximum turbulent recession augmentation factor due to entropy swallowing
R_N	initial nosetip radius, in
R_{N_e}	effective nosetip radius, in
R_{N_f}	nosetip shoulder radius, in
Re_2	Reynolds number behind normal shock
Re_k	roughness Reynolds number defined by Eq. (69)
Re_θ	momentum thickness Reynolds number
s	running length from stagnation point, in
$\dot{s}$	axial recession rate, in/s
Δs	nosetip recession, in
t	time, s
T	temperature, ^oR
u	gas velocity, ft/s
$\bar{x}$	x-coordinate of laminar region geometric center, in
x_s	x-coordinate of stagnation point, in
$\bar{y}$	y-coordinate of laminar region geometric center, in
y_s	y-coordinate of stagnation point, in
z	axial distance, in

z'_{To}	turbulent ray segment intercept on Z'-axis, in
γ_T	trim angle-of-attack, deg
α	trajectory entry angle, deg
δ	boundary layer thickness, mil
δ_1	boundary layer displacement thickness, mil
Δ	nosetip offset, in
Δ_s	shock standoff distance, in
ε	approximate nosetip eccentricity
η	compressible boundary layer normal coordinate defined by Eq. (73)
θ	local body surface inclination angle, deg
θ_e	body inclination angle downstream of pt. 2, deg
θ_3	body inclination angle at pts. 3 and 4 for severely indented rays, deg
Λ	boundary layer shape factor
μ_w	gas viscosity at wall
$\Delta\xi$	bow shock proximity influence parameter, in
ρ	gas density, lbm/ft^3
ρ_o	material bulk density, lbm/ft^3
σ_k	normalized roughness element height standard deviation
$\sigma_{\bar{k}}$	standard deviation of average laminar roughness, mil
ϕ	meridional angle, deg

ϕ_w	windward meridian, deg
ϕ_ψ	cant meridian, deg
$\phi_{d\Delta}$	meridian of offset change, deg
$\Delta\phi$	nosetip segment width, deg
$\Delta\phi_T$	total angular width of turbulent segments, deg
ψ	cant angle, deg

Subscripts

1	denotes nosetip stagnation point
2	denotes laminar shoulder
3	denotes end of concave region
4	denotes nosetip-frusta intersection point
c	denotes center point for concave region arc
f	frusta
i	denotes indented ray parameter, see Eqs. (8) and (9); also denotes i th ray
k	roughness
L	laminar boundary layer flow
m	median
o	denotes sphere-cone tangent point; also no blowing value
r	recovery
s	stagnation

ss	steady-state
tr	transition
W	wall
∞	freestream

Superscripts

-	average value
*	sonic
'	nosetip coordinates

SECTION 1

INTRODUCTION

The objective of this study has been to develop an analytical model of reentry vehicle nosetip shape change suitable for inclusion in a larger simulation model for the calculation of vehicle aerodynamics, trajectories, and impact point dispersion. Since the purpose of the simulation is to derive impact point statistics, the nosetip shape change model is required to include the statistical influence of boundary layer transition on developing asymmetric nosetip shapes, and must also be ameanable to Monte Carlo simulation for varying reentry vehicle configurations, missions, and nosetip materials. This latter requirement limits the complexity of the nosetip change model even though detailed numerical models for heat transfer, thermochemical ablation, and surface recession have been developed and employed with success in the axisymmetric prediction of nosetip recession during entry. The computer time requirements for these methods even with the simplest asymmetric shape representation (body-fixed, windward-leeward rays) are several orders-of-magnitude greater than that desired for statistical analysis of reentry vehicle dispersion.

The approach taken in the present study has been to retain physical and numerical sophistication only in those areas of nosetip shape change which directly affect the asymmetry of the shape development. Hence, roughness statistics, boundary layer transition, and surface representation in multiple meridional planes are emphasized in the model while laminar and turbulent recession rates are obtained from correlation equations involving freestream quantities and nosetip shape parameters. Section 2 describes the geometric nosetip representation used in the model, shape change modeling, and pertinent nosetip material properties affecting the development of asymmetric nosetip shapes.

Section 3 presents correlations of reentry vehicle flight test results and a summary of conclusions.

SECTION 2

NOSETIP SHAPE CHANGE MODELING

The primary mechanism leading to the development of asymmetrical nosetip shapes for ballistic reentry vehicles is increased local ablation rate in regions of turbulent boundary layer flow. Since the ratio of turbulent to laminar convective heating rates is larger than unity for roughness induced transition, transition to turbulent flow results in enhanced local recession rate and the development of gouges on the nosetip. This phenomenon has been observed in numerous ground and flight tests of graphitic nosetip materials. Figure 1 shows the recovered bulk graphite NRV reentry vehicle nosetip (Reference 1) and a carbon-carbon nosetip model tested in the Air Force Flight Dynamics 50 MW RENT arcjet facility. The qualitative similarity between the two nosetips is apparent. Both materials exhibit longitudinal gouges attributed to increased recession rate due to turbulent vortices. The laminar flow stagnation region is irregular in shape due to circumferentially nonuniform transition and is offset from the nosetip centerline.

The class of nosetip shapes illustrated by those in Figure 1 is an intermediate type developed as transition progresses toward the nosetip stagnation point. At earlier times isolated gouges associated with individual turbulent vortices are observed and at later times (and/or higher freestream Reynolds number) the laminar region may virtually disappear as transitional progresses very near to the stagnation point. The important features of nosetip shaping evident from these observations are the location and size of the laminar region relative to the nosetip centerline and the number and width of the turbulent gouges.

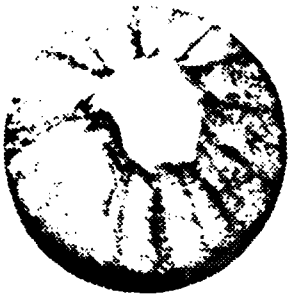

A. Recovered Flight Test Nosetip

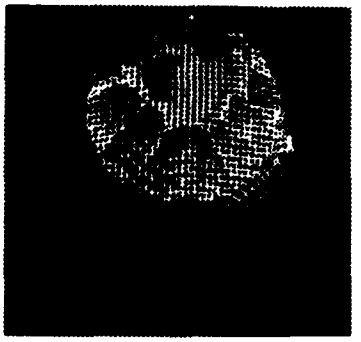

B. 50 MW Test Model

Figure 1. Typical Asymmetric Nosetip Shapes

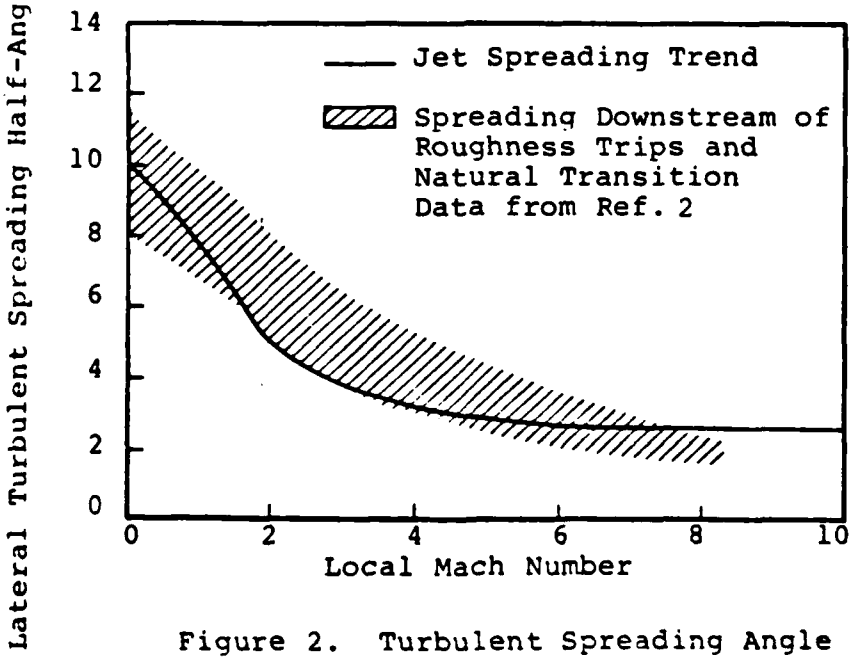

Figure 2. Turbulent Spreading Angle

Previous efforts to model asymmetric shape change have concentrated on the windward and leeward ray shape change by employing different transition location (or roughness values) for these rays. Detailed shape change calculations for windward and leeward side rays have been accomplished, although matching of the two solutions in the stagnation region and determining the stagnation point location is not trival. While this approach can define certain classes of asymmetric shapes, it is not sufficient to describe wind angle orientation changes or nosetip rolling moment coefficient. In order to adequately describe these features the full circumferential response of the nosetip must be considered.

2.1 GEOMETRIC REPRESENTATION

For the present model 20 rays are used to describe the nosetip. Initially, before ablation and transition occurs the 20 rays are spaced equally around the nosetip circumference and each ray represents the average nosetip profile over an 18-deg segment. The number of rays is chosen so that the 18-deg initial segment width matches previously published empirical and theoretical estimates of the size of turbulent wedges in subsonic flow (see Figure 2) and also correlates well with the number of gouges typically observed on ground test and recovered flight test nosetips. Each of the rays is characterized by several geometric parameters as described in the following paragraphs.

Since detailed heat transfer, ablation, and surface recession calculations are not practical for the present model, the conventional shape change code definition of the nosetip surface by many receding surface points is neither required nor desired. Instead each ray defining the nosetip surface is characterized by the location of four points and several circular arc and straight line segments.

2.1.1 Nosetip Ray Shapes

Figure 3 illustrates the nosetip ray shapes considered and defines the pertinent parameters. The ray geometric parameters are defined relative to the nosetip coordinates r', z' where the origin of the axes is at the stagnation point of the nosetip and the z' axis is parallel to the nosetip cant vector defined in Section 2.2.

Laminar ray segments are defined by a circular arc of radius R_1 passing thru the origin (point 1) and with center on the z'-axis. The laminar segment terminates at point 2 which will be either on the vehicle frusta (Figure 3a) for an all-laminar ray or at the "laminar island" corner (Figs. 3b, 3c, 3d, 3e). The equation defining the laminar segment is

$$r' = + \sqrt{R_1^2 - (R_1 - z')^2}, \quad 0 \leq z' \leq z'_2 \qquad (1)$$

Turbulent recession is generally described by a straight line from point 3 to point 4. The shape of the line segment is defined by a fixed body inclination angle θ_T, and the z'-axis intercept is denoted by z'_{To}:

$$r' = (z' - z'_{To}) \tan\theta_T, \quad z'_3 \leq z' \leq z'_4 \qquad (2)$$

z'_{To} is calculated from the total turbulent recession after transition occurs on the segment. For non-zero lengths this turbulent flow segment will always be terminated by intersection with the vehicle frusta at point 4 as shown in Figures 3b, 3c, and 3e. The segment begins at the laminar island corner for non-indented shapes (Figs. 3b and 3e) or downstream of the recompression region described next.

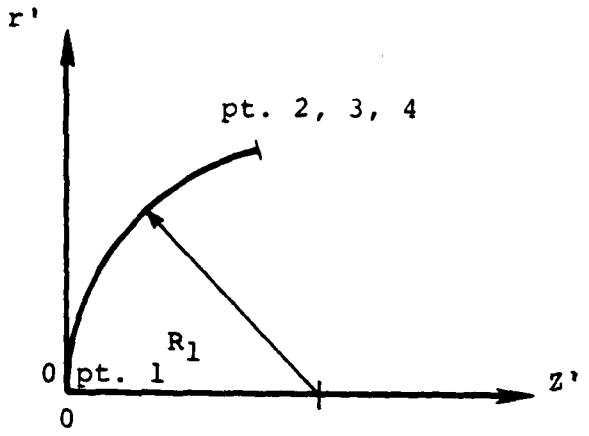

a. Laminar

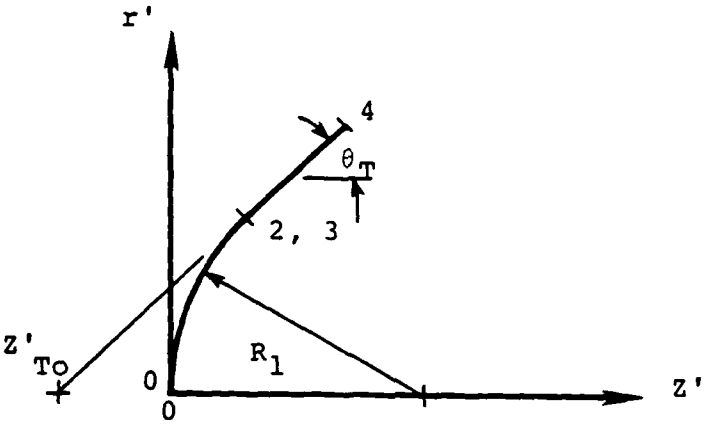

b. Transitional

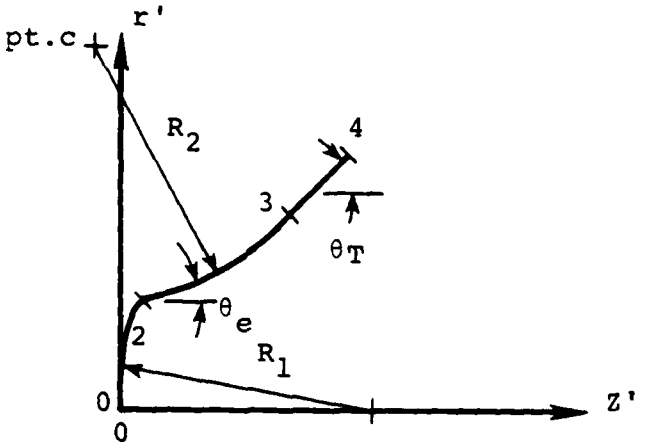

c. Indented

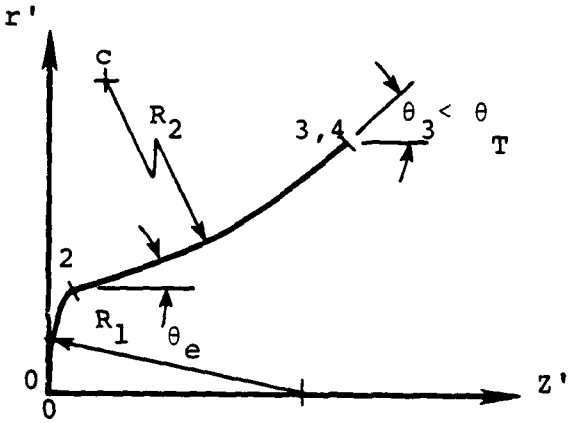

d. Severely Indented

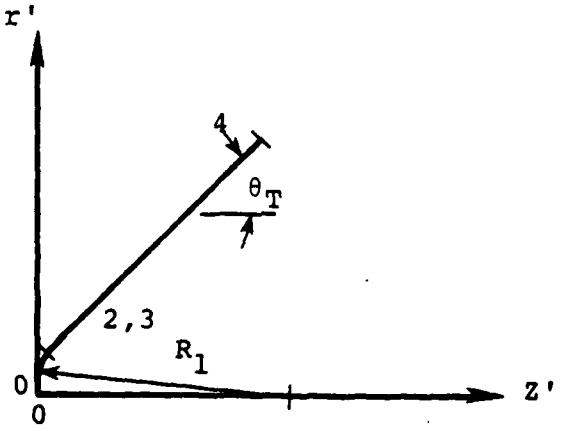

e. Equilibrium Turbulent

Figure 3. Geometrical Definition of Nosetip Rays

Figures 3c and 3d illustrate the modeling of indented nosetips by use of a circular arc segment from point 2 to point 3. The arc has its center at point c (r'_c, z'_c) and a radius, R_2, so that the equation

$$r' = r'_c - \sqrt{R_2^2 - (z' - z'_c)^2}, \quad z'_2 \leq z' \leq z'_3 \tag{3}$$

describes the segment. The three parameters, r'_c, z'_c and R_2 which define the segment are determined by the following geometric conditions:

a) the body inclination just downstream of the laminar island corner is equal to a fixed angle denoted by θ_e.

b) the arc is tangent to the turbulent flow segment (Figure 3c) if $r'_3 \leq r'_4$ or the arc passes through point 4 determined by the intersection of the turbulent flow segment with the frusta (Figure 3d).

For the indented shape given by the first case above the center location and radius of the recompression arc are

$$R_2 = a/\sin\,[(\theta_T - \theta_e)/2] \tag{4}$$

$$r'_c = r'_2 + R_2 \cos\theta_e \tag{5}$$

$$z'_c = z'_2 - R_2 \sin\theta_e \tag{6}$$

where

$$a = [(r'_i - r'_2)^2 + (z'_i - z'_2)^2]^{1/2} \tag{7}$$

and

$$z'_i = (r'_2 - z'_2\tan\theta_e + z'_{To}\tan\theta_T)/(\tan\theta_T - \tan\theta_e) \tag{8}$$

$$r'_i = (z'_i - z'_{To})\tan\theta_T \tag{9}$$

The location of point 3 is

$$r'_3 = r'_i + a\sin\theta_T \tag{10}$$

$$z'_3 = z'_i + a\cos\theta_T \tag{11}$$

For the severely indented case one has

$$r'_3 = r'_4 \tag{12}$$

$$z'_3 = z'_4 \tag{13}$$

$$R_2 = b/\{2\sin[(\theta_3 - \theta_e)/2] \tag{14}$$

where

$$b = [(r'_4 - r'_2)^2 + (z'_4 - z'_2)^2]^{1/2} \tag{15}$$

and the inclination of the recompression arc where it intersects with the frusta is

$$\theta_3 = 2\tan^{-1}[(r'_4 - r'_2)/(z'_4 - z'_2)] - \theta_e \tag{16}$$

The center of the circular arc is given by Eqs.(5) and (6).

The above equations describe permissible nosetip ray shapes in terms of several key shape change parameters R_1, r'_2 and z'_{To}; two fixed inclination angles, θ_e and θ_T; and the nosetip oriented coordinate system discussed below.

2.1.2 Offset and Cant

The 20 rays which describe the nosetip shape are referenced to nosetip coordinates (r', z') which reflect the

"average" asymmetry of the nosetip. The origin of the r', z' axis is the nosetip stagnation point defined by the radial offset of the stagnation point from the vehicle centerline, Δ (see Figure 4) and the total recession of the stagnation point, $\Delta s'$, along the instantaneous z'-axis. The z'-axis is inclined at the cant angle, Ψ, to the vehicle centerline. The parameters Δ and Ψ are functions of recession rate, transition location asymmetry, and vehicle angle-of-attack. Since they represent average nosetip asymmetries, approximate equations obtained by correlation of ground and flight test shape change results are used to describe their rate of change.

The position of the stagnation point of an asymmetric nosetip is difficult to estimate. Theoretically, for hypersonic flow stagnation occurs at that point on the surface which is inclined at 90-deg to the freestream velocity vector. In reality, especially at the lower altitudes where asymmetric nosetip shapes develop, the hypersonic flow limit is not attained and some curvature of the stagnation streamline may occur in the shock layer. Since the entire laminar flow region of the nosetip may be nearly flat, significant movement of the stagnation point due to streamline curvature may be expected. Also, the bow shock is probably significantly affected by the sonic point at the laminar region shoulder and this provides strong damping of any local surface slope anomalies. Based on these observations it is assumed that the stagnation point approaches the geometric center $(\bar{x}, \bar{y})$ of the subsonic flow region:

$$\bar{x} = \sum_{i=1}^{20} (\Delta\phi'_i)(r^*_i)^3 \sin\phi'_i / 6A^* + x_s \qquad (17)$$

$$\bar{y} = \sum_{i=1}^{20} (\Delta\phi'_i)(r^*_i)^3 \cos\phi'_i / 6A^* + y_s \qquad (18)$$

$$A^* = \sum_{i=1}^{20} (\Delta\phi'_i)(r^*_i)^2 / 2 \qquad (19)$$

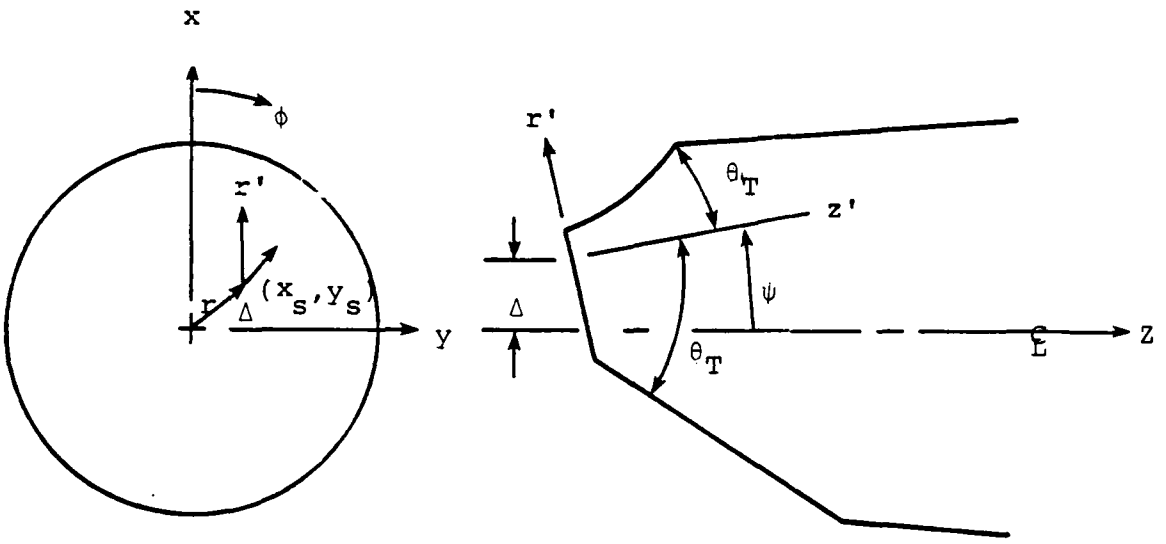

Figure 4. Definition of Nosetip Coordinates

$$r^*_i = r'_{2i}, \text{ turbulent flow}$$

$$= \min[r'_{4i}, R_l(1 + \varepsilon^2)^{-1/2}], \text{ laminar flow} \quad (20)$$

where A* is the area of subsonic flow and the subscript "i" refers to the "i" segment (or ray) of angular width, $\Delta\phi'_i$. Note that r* is defined in the nosetip coordinate system whereas $\bar{x}$ and $\bar{y}$ are in the vehicle coordinate system. Transition locations determine $(\bar{x}, \bar{y})$ directly through their influence on the laminar shoulder positions, r'_{2i}. However, the nosetip stagnation point only approaches $(\bar{x}, \bar{y})$ at a finite rate dependent on the nosetip turbulent recession rate, e.g.

$$\left.\frac{dx_s}{dt}\right|_{\Psi=0} = \dot{s}_T \sin\theta_e \left(\frac{\Delta\phi_T}{2\pi}\right)^2 \left(\frac{x-x_s}{\ell}\right) \quad (21)$$

$$\left.\frac{dy_s}{dt}\right|_{\Psi=0} = \dot{s}_T \sin\theta_e \left(\frac{\Delta\phi_T}{2\pi}\right)^2 \left(\frac{y-y_s}{\ell}\right) \quad (22)$$

where $\Delta\phi_T$ is the total angular width of turbulent flow

$$\Delta\phi_T = \sum_{\substack{i=1 \\ i=\text{laminar}}}^{20} \Delta\phi'_i$$

and

$$\ell = [(\bar{x} - x_s)^2 + (\bar{y} - y_s)^2]^{1/2} \quad (24)$$

In addition to the stagnation point movement due to the difference in $(\bar{x}, \bar{y})$ and (x_s, y_s), both quantities respond to nosetip angle of attack and cant:

$$\frac{dx_s}{dt} = \left.\frac{dx_s}{dt}\right|_{\Psi=0} + \dot{s}_L \sin\Psi\cos\phi_\Psi \quad (25)$$

$$\frac{dy_s}{dt} = \frac{dy_s}{dt}\bigg|_{\Psi=0} + \dot{s}_L \sin\alpha_T \sin\phi_w \Psi \tag{26}$$

$$\frac{d\bar{x}}{dt} = -\dot{s}_L \sin\alpha_T \cos\phi_w \tag{27}$$

$$\frac{d\bar{y}}{dt} = -\dot{s}_L \sin\alpha_T \sin\phi_w \tag{28}$$

that is, for non-zero nosetip cant the stagnation point will move parallel to the cant vector as the nosetip recedes while $(\bar{x}, \bar{y})$ moves parallel to the freestream velocity vector. The offset, Δ, is then

$$\Delta = (x_s^2 + y_s^2)^{1/2} \tag{29}$$

The nosetip cant vector has been observed in ground tests at angle-of-attack to become parallel to the freestream velocity vector as nosetip recession progresses. The rate of change of the cant angle is assumed to be proportional to an average nosetip recession rate

$$\bar{\dot{s}} = \sum_{\substack{i=1 \\ i\neq\text{turbulent}}}^{20} \dot{s}_L\left(\frac{\Delta\phi_i}{2\pi}\right) + \sum_{\substack{i=1 \\ i\neq\text{laminar}}}^{20} \dot{s}_T\left(\frac{\Delta\phi_i}{2\pi}\right) \tag{30}$$

and the difference in α_T and the cant angle and inversely proportional to nose radius

$$\frac{d\Psi_x}{dt} = -2\pi(\alpha_T \cos\phi_w + \Psi_x)\bar{\dot{s}}/R_N \tag{31}$$

$$\frac{d\Psi_y}{dt} = -2\pi(\alpha_T \sin\phi_w + \Psi_y)\dot{s}/R_N \qquad (32)$$

where Ψ_x and Ψ_y are the x and y components of the cant vector

$$\Psi = (\Psi_x^2 + \Psi_y^2)^{1/2} \qquad (33)$$

and

$$\phi_\Psi = \arctan(\Psi_y/\Psi_x) \qquad (34)$$

2.2 NOSETIP SHAPE CHANGE

Reentry vehicle nosetip shape change due to material ablation is primarily described by correlation equations for laminar and turbulent recession rates as a function of nosetip stagnation pressure and enthalpy and various nosetip shape parameters such as effective nose radius. These equations are used to compute the geometric parameters which define the line and arc segments describing the instantaneous nosetip shape.

2.2.1 Laminar Recession Rate

Mass loss rate at the nosetip stagnation point is a product of the laminar flow heat transfer rate and the mass transfer parameter B'. Since the heat transfer rate in laminar flow is proportional to $\sqrt{P_s/R_{N_e}}$, a correlation of $\dot{m}/\sqrt{P_s/R_{N_e}}$ as a function of stagnation enthalpy is suggested. Figure 5 presents data calculated for two typical vehicle trajectories using the SAI Combined Ballistic Reentry Assessment (COBRA) computer code, a fairly sophisticated shape change code which includes detailed roughwall heat transfer (Reference 3), thermochemical ablation (Reference 4), and boundary layer transition theories (Reference 5). For these trajectories only altitude points prior to boundary layer transition on the nosetip are considered and stagnation point heating augmentation is not included. The analytical results are well correlated by the equations

$$\dot{m}_{Lo} = 1.747\times10^{-6}\sqrt{P_s/R_{N_e}}\, H_s^{0.755}, \quad H_s \geq 2230 \qquad (35)$$

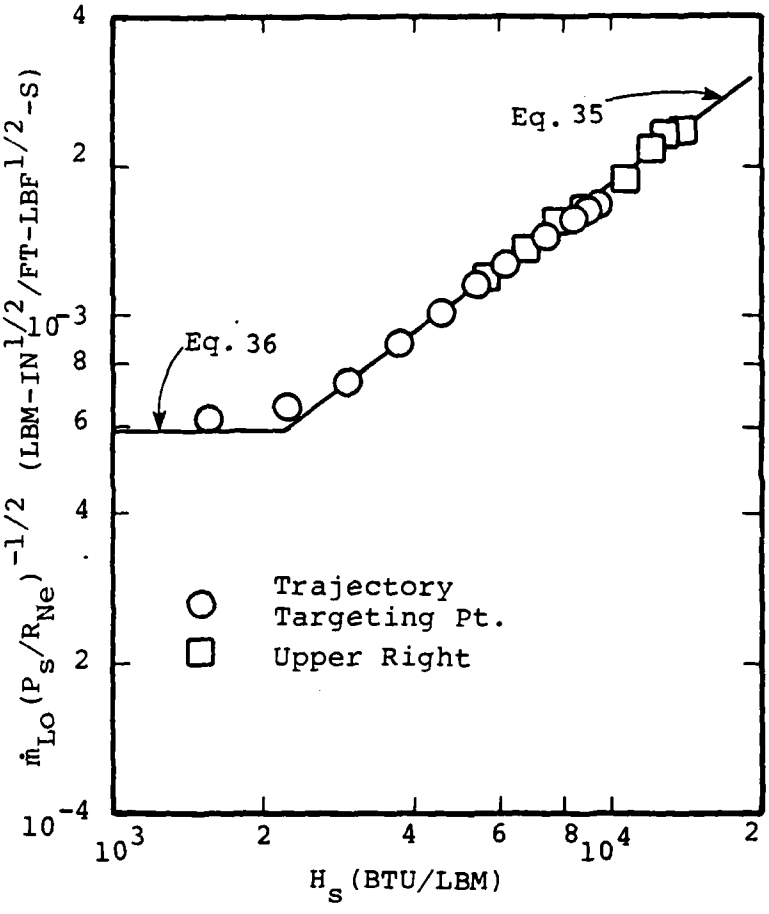

Figure 5. Laminar Flow Stagnation Point Mass Loss Rate

$$\dot{m}_{Lo} = 5.892 \times 10^{-4} \sqrt{P_s / R_{N_e}}, \quad H_s < 2230 \tag{36}$$

where $\dot{m}_{Lo}$ is the stagnation point laminar mass loss rate without heat transfer augmentation. The corresponding equations for B'_o (see Figure 6) which will be used in Section 4.3 for transition calculations are

$$B'_o = 4.632 \times 10^{-4} H_s^{0.755}, \quad H_s \geq 2230 \tag{37}$$

$$B'_o = 0.156, \quad H_s < 2230 \tag{38}$$

Laminar heating augmentation is the subject of considerable uncertainty at the present time. Several correlations have been developed (References 6 and 7). However, the physical mechanism (e.g., transition location proximity or roughness) responsible for the observed increase in stagnation region heating is still uncertain. The present study uses a correlation based on roughness disturbance of the approaching shock layer flow (Reference 8)

$$\frac{C_H}{C_{H_{Lo}}} = \max \left\{ 0.206 \left[Re_2 \left(\frac{k_L}{\Delta_s + k_L} \right)^{1.5} \right]^{0.28}; \ 1.0 \right\} \tag{39}$$

where Re_2 is the Reynolds number behind the bow shock based on body stagnation region radius of curvature (R_1) and Δ_s is the shock standoff distance. The shock standoff distance is calculated from the following correlation

$$\log_{10}\left(\frac{\Delta_s}{R_{N_e}}\right) = 0.1609 + 1.4891 \log_{10}\left(\frac{\rho_\infty}{\rho_s}\right) + 0.2323 \left[\log_{10}\left(\frac{\rho_\infty}{\rho_s}\right)\right]^2 \tag{40}$$

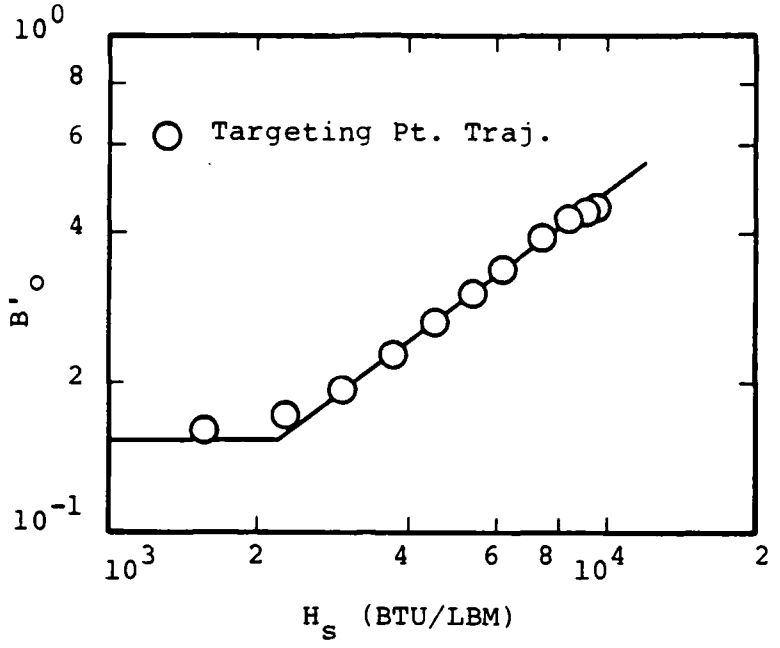

Figure 6. Laminar Flow Mass Loss Parameter

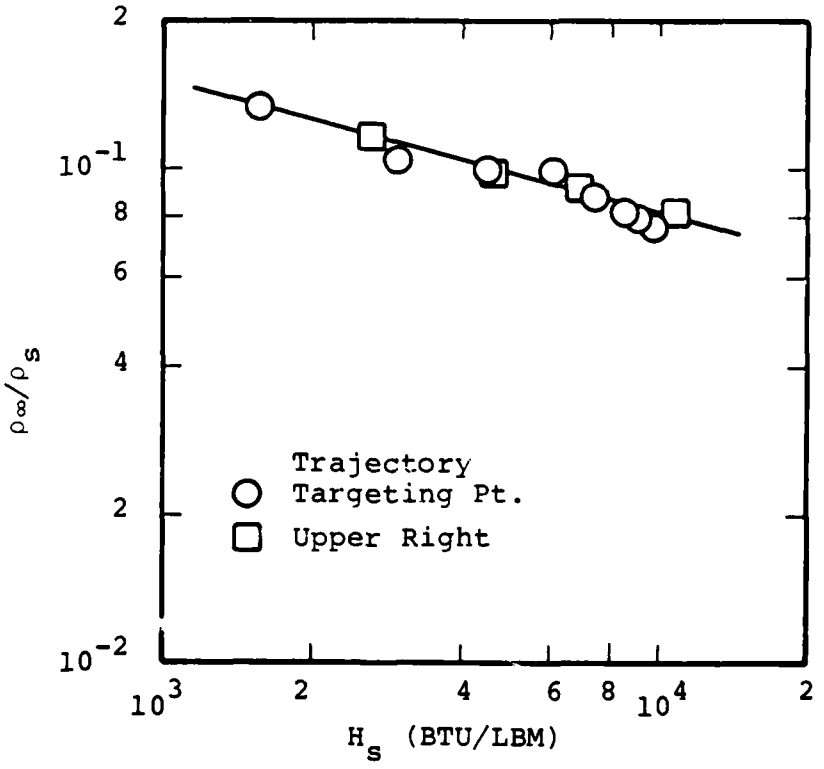

Figure 7. Normal Shock Density Ratio

Figures 7 and 8 show the correlations used for Re_2 and (ρ_∞/ρ_s)

$$\rho_\infty/\rho_s = 0.9144\ H_s^{-0.261} \tag{41}$$

$$Re_2 = 13000.\ (P_s/H_s)^{0.966} R_1 \tag{42}$$

A correction for high altitude transient heat conduction is also applied to the calculation of $\dot{s}_L$. The equation used is

$$\dot{s}_L/\dot{s}_{Lss} = 0,\ \tilde{Q} \leq 1.0$$

$$= \left\{\sin\left[\frac{\pi(\tilde{Q}-1)}{13.2}\right]\right\}^{0.44},\ 1 < \tilde{Q} < 14.2$$

$$= 1.0,\ \tilde{Q} \geq 14.2 \tag{43}$$

Where $\tilde{Q}$ is a measure of the integrated nosetip heating

$$\tilde{Q} = 10^{-6} \int_0^t (P_s/R_{N_e})^{1/2}\ H_s dt \tag{44}$$

Eq. 43 is based on several results obtained with the COBRA computer code for graphitic nosetip materials (See Figure 9).

The final equation for laminar recession rate which is used to obtain nosetip stagnation point recession is

$$\dot{s}_L = 12(\dot{s}_L/\dot{s}_{ss})(C_H/C_{H_{LO}})\dot{m}_{LO}/\rho_o \tag{45}$$

where ρ_o is the bulk density of the nosetip material. The nosetip stagnation point recession is then

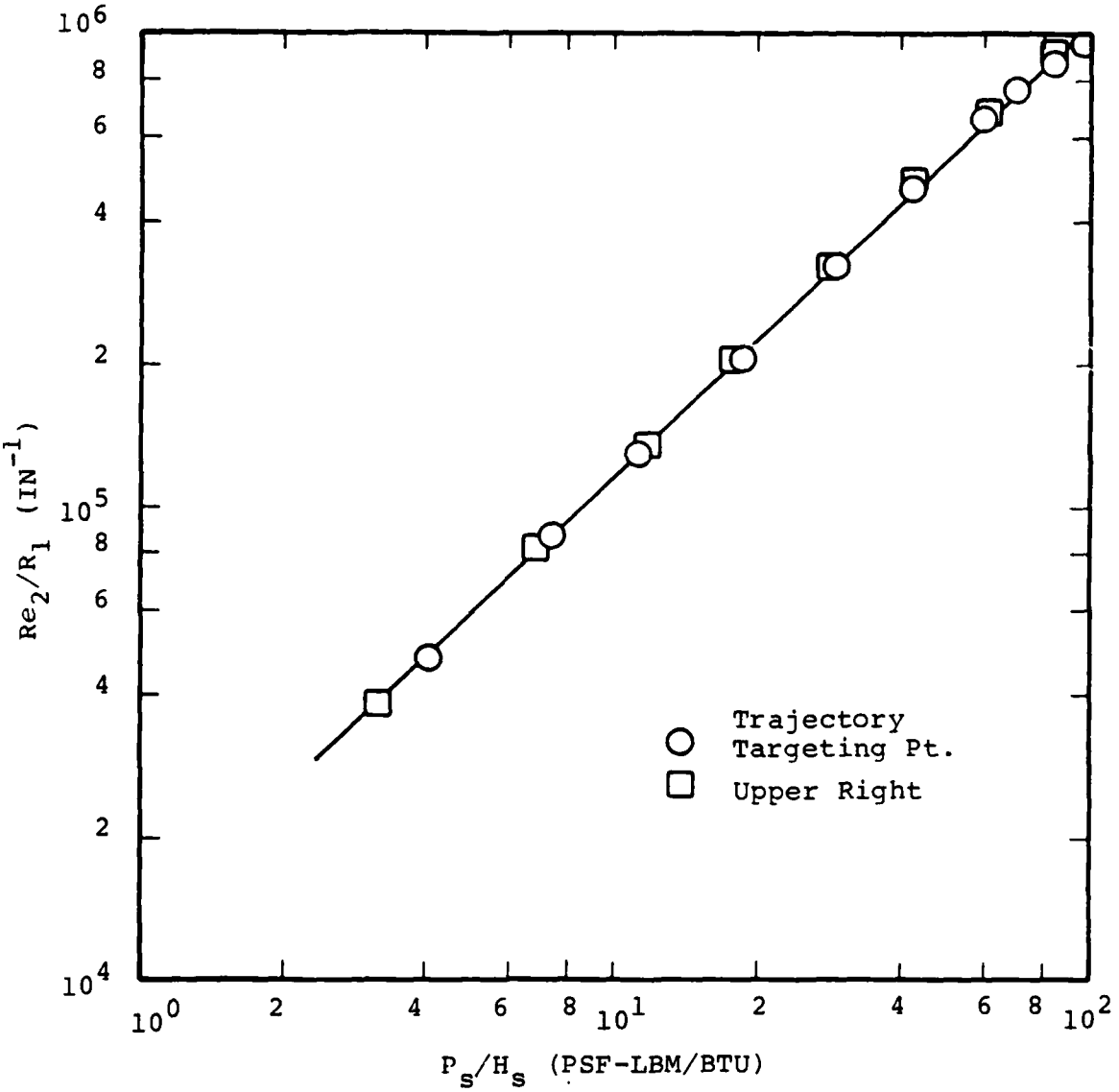

Figure 8. Reynolds Number Behind Normal Shock

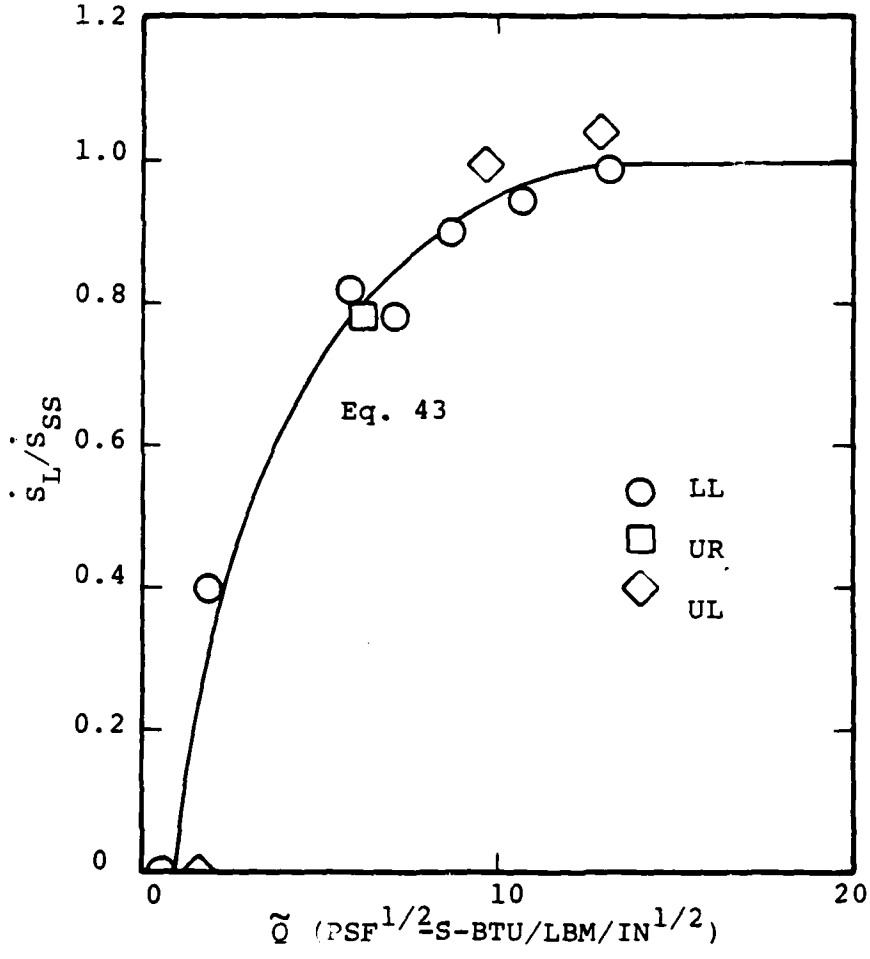

Figure 9. High Altitude Transient Ablation

$$z_1 = \int_o^t \dot{s}_L \cos \Psi dt \tag{46}$$

in vehicle fixed (unprimed coordinates) and

$$\Delta s = \int_o^t \dot{s}_L \, dt \tag{47}$$

is the total recession along the instantaneous nosetip axis (z'-direction). The later recession is used to define the laminar segment radius of curvature

$$R_1 = [R_N + \Delta + \Delta s/f_1(\tilde{\theta}_f)]/\varepsilon \tag{48}$$

where

$$\varepsilon = \exp(-\Delta s/2R_N) \tag{49}$$

$$f_1(\theta) = \frac{\cos\theta}{\tan\theta} + \sin\theta - 1$$

$$\tilde{\theta}_f = \theta_f + \Psi \tag{50}$$

and an average shoulder radius

$$R_{N_f} = R_N + \Delta s/f_1(\theta_f) \tag{51}$$

The equivalent nose radius, R_{N_e}, used to calculate the laminar recession rate is evaluated in the following manner. First, an average sonic point radius is obtained by considering each of the nosetip rays. For laminar rays defined by the radius of curvature, R_1, one has approximately

$$r^*_i = \min \{r'_{4i}; R_1(1 + \varepsilon^2)^{-1/2}\} \tag{52}$$

while for turbulent rays

$$r^*_i = r'_{2i} \tag{53}$$

The average sonic point radius is evaluated from the summation of values for each ray weighted by the angular width of each segment

$$\bar{r}^* = \frac{1}{2\pi} \sum_{i=1}^{20} r^*_i \Delta\phi'_i \qquad (54)$$

and the corresponding value of z' is

$$\bar{z}^* = R_1 - \sqrt{R_1^2 - \bar{r}^{*2}}$$

R_{N_e} is evaluated from a correlation of the experimental data of Reference 9

$$R_{N_e} = 0.9557\ R_1;\ \bar{z}^*/\bar{r}^* \geq 0.4142$$

$$= \bar{r}^*/(0.16 + 1.4\ \bar{z}^*/\bar{r}^*);\ 0.4142 > \bar{z}^*/\bar{r}^* > 0.268$$

$$= 1.87\bar{r}^*;\ \bar{z}/\bar{r}^* < 0.268 \qquad (55)$$

The last condition is required to account for the elliptical laminar region shape which develops during nosetip ablation.

2.2.2 Turbulent Recession Rate

Correlation of the recession rate of a nosetip in the turbulent boundary layer flow regime is complicated by the dependency of turbulent heat transfer rates on the specifics of the nosetip shape. Unlike the case of stagnation region laminar flow which is well characterized primarily by the single shape parameter of equivalent nose radius, turbulent flow heat transfer may depend on several cylindrical radii such as the laminar shoulder radius (r'_2) and the nosetip shoulder radius (r'_4) and also on the inclination of the turbulent section, the degree of indentation, etc. The present modeling approach is derived from correlation and analysis of a series of more detailed COBRA computer code results and supporting

sensitivity studies. The same procedure as in laminar flow is followed, i.e., a basic mass loss rate correlation for turbulent flow is developed and then various modifying factors are imposed to account for selected shape change features.

The recession rate desired is the axial recession rate of the biconic turbulent gouge faces. These rates were obtained from three COBRA results without entropy swallowing and correlated using the assumption that $\dot{s}_{To}$ is proportional to the factor $P_s^{0.8}(k_s/R_{N_f})^{.2}$ where k_s is the equivalent sand roughness of the material for turbulent flow. Figure 10 shows that this approach provides a reasonable fit to the calculated data via the equation

$$\dot{s}_{To} = 6.339\text{x}10^{-6}\ P_s^{0.8}\ H_s^{0.615}\ (k_s/R_{N_f})^{0.2}/\rho_o,\ H_s > 1965$$

$$\dot{s}_{To} = 6.722\text{x}10^{-6}\ P_s^{0.8}\ (k_s/R_{N_f})^{0.2}/\rho_o,\ H_s \leq 1965 \qquad (56)$$

As for laminar flow a constant B' region corresponding to diffusion controlled oxidation is apparant at low values of stagnation enthalpy.

The increase in local turbulent recession rate due to entropy swallowing is included by using a correlation of the increased boundary layer edge mass flow rate due to the change in entropy for streamlines crossing an oblique shock. Figure 11 presents data for the boundary layer edge mass flux ratio for a sharp 45-deg body for typical reentry trajectories. The mass flux ratio is nearly independent of nosetip stagnation pressure and is well fit by the equation

$$\rho_e u_e/(\rho_e u_e)_o = 0.803\ H_s^{0.1334}\ P_s^{0.00435} \qquad (57)$$

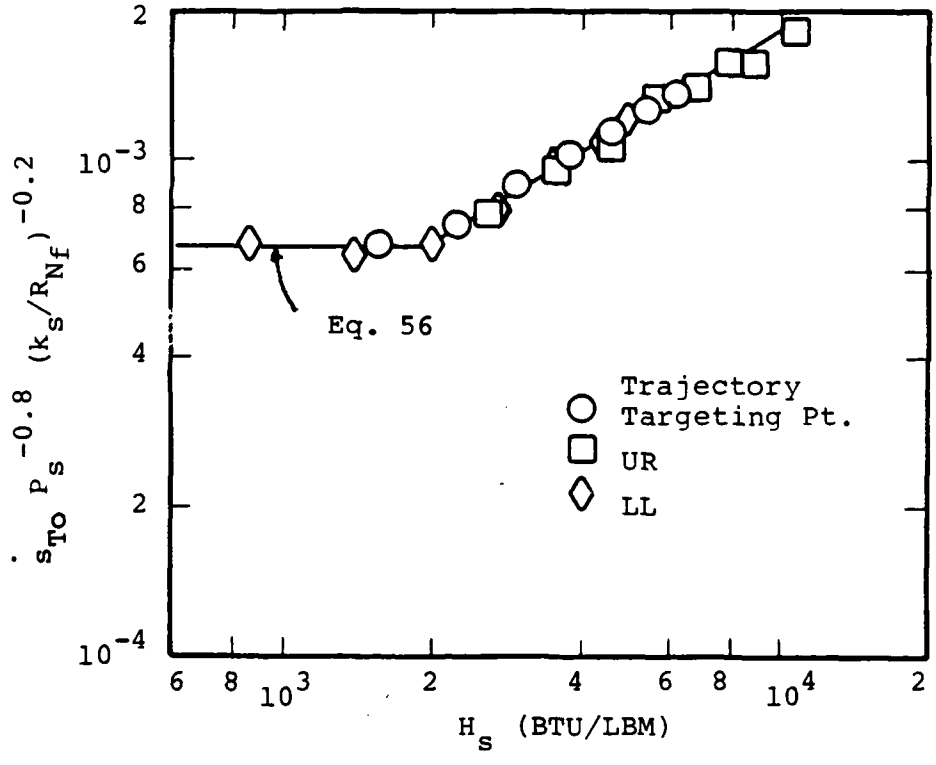

Figure 10. Turbulent Flow Recession Rate

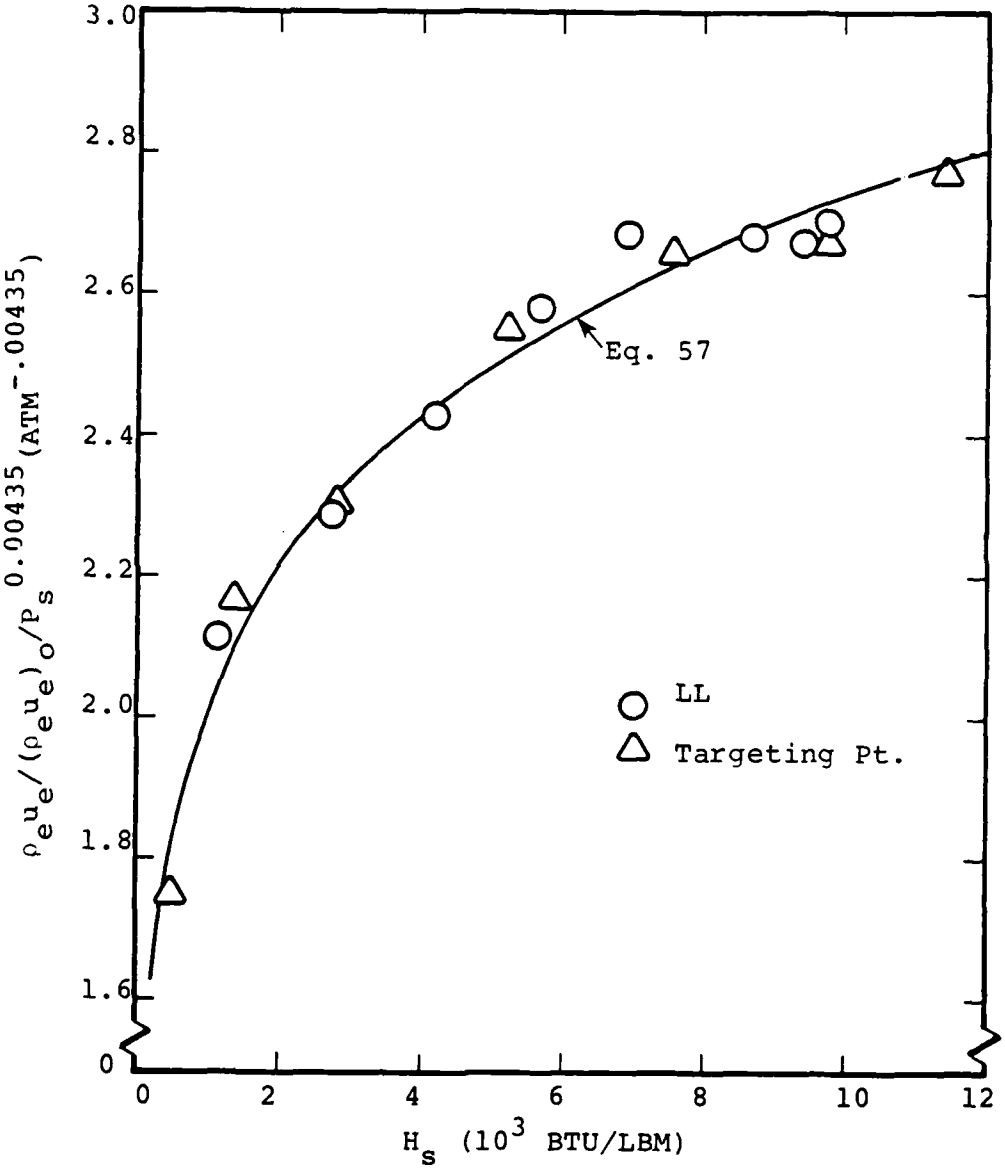

Figure 11. Mass Flow Increase for 45° Body

Additional results have been calculated for body angles of 40 and 50-deg and the same trajectories yielding the following correlation equations

$$\underline{40°} \qquad \rho_e u_e/(\rho_e u_e)_o = 1.588\ H_s^{0.0676} P_s^{-0.022}$$

$$\underline{50°} \qquad \rho_e u_e/(\rho_e u_e)_o = 3.951\ H_s^{-0.0386} P_s^{-0.022}$$

These results are compared with those for the 45-deg body for the targeting point trajectory in Figure 12. Only limited sensitivity to body angle is indicated, primarily below the altitude of 20,000 feet where stagnation enthalpy decreases rapidly for this trajectory. For instance, the maximum deviation of the mass flux ratio from the 45-deg results is +24 per cent evidenced by the 50-deg body at zero altitude. The maximum increase in turbulent recession rate due to entropy swallowing is then

$$R_{max} = [\rho_e u_e/(\rho_e u_e)_o]^{0.8}$$

assuming $\dot{s}_T$ is directly proportioned to $\rho_e u_e C_H$ and neglecting the slight effect of changes in boundary layer edge viscosity due to entropy swallowing.

The actual increase in turbulent recession rate depends on the average entropy of the streamlines intersecting the turbulent boundary layer and hence on the shape of the bow shockwave. Detailed calculations of the bow shockwave shape and boundary layer mass entrainment are not feasible for the present model and a approximate relation dependent on the ratio of the effective nosetip radius and the average shoulder radius is used.

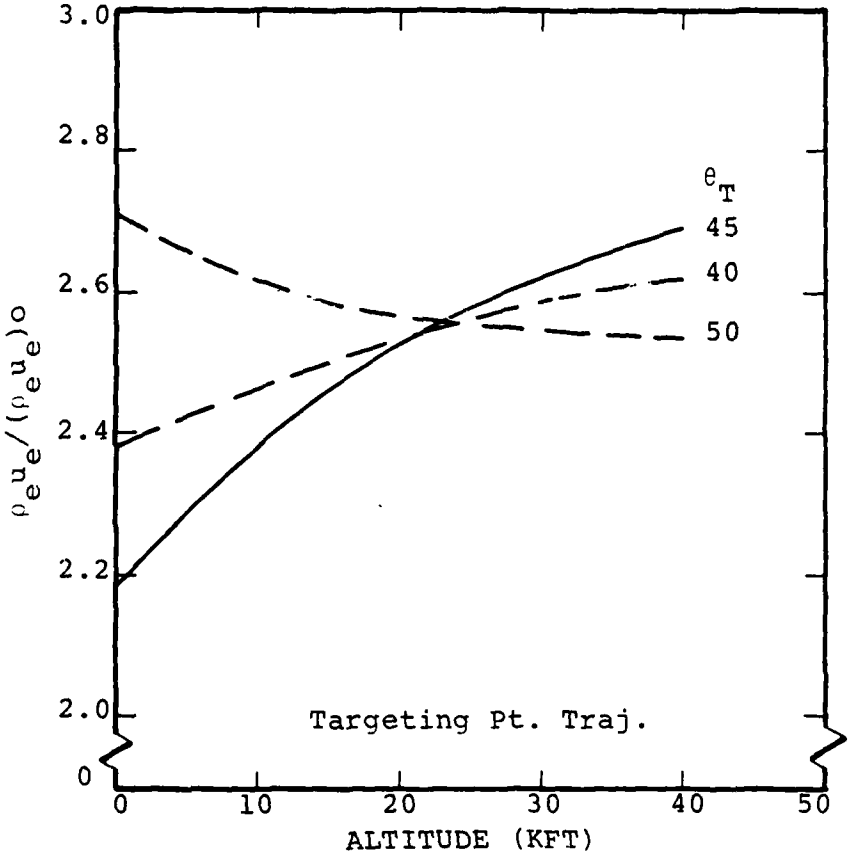

Figure 12. Effect of Body Slope on Mass Flow

$$f_e = 1 + (R_{max}-1)\exp[-6.45(R_{N_e}/R_{N_f})^{1.5}] \qquad (58)$$

where f_e is the ratio of turbulent axial recession with and without entropy swallowing. This relationship indicates that little effect of entropy swallowing is predicted until the ratio R_{N_e}/R_{N_f} is less than 0.4 (see Figure 13); that is, until the nosetip has sharpened sufficiently to cause the bow shock to become significant oblique close to the stagnation point.

The turbulent recession rate given by $\dot{s}_{T_o} f_e$ represents an average equilibrium axial recession rate for axisymmetric nosetip shapes which are not severely idented. Modifications to this average rate for individual turbulent gouges are believed to occur due to asymmetric effects and for severely indented gouges. For nosetip rays which are severely indented (i.e., where θ_{3i} is less than the equilibrium turbulent angle θ_T - see Figure 3d) the turbulent recession rate is assumed to be reduced because of the lower average surface pressure resulting from the reduced body inclination angle. Assuming again that turbulent recession rate varies directly as surface pressure to the 0.8 power, the reduction in axial recession rate for severely indented rays is given by the factor

$$f_{\theta i} = (\sin\theta_{3i}/\sin\theta_T)^{0.6} \qquad (59)$$

The correction for asymmetric nosetip shape is less easily quantified. Examination of the recovered nosetip from the NRV flight test vehicle shown in Figure 1 indicates that the intersections of the turbulent gouges with the conical frusta occur at a uniform axial station even though asymmetric transition is evident. Similar results have been observed to occur in arc-jet ablation tests soon after all nosetip rays have experienced turbulent flow. However, prior to that time when only isolated gouges occur, large differences in these

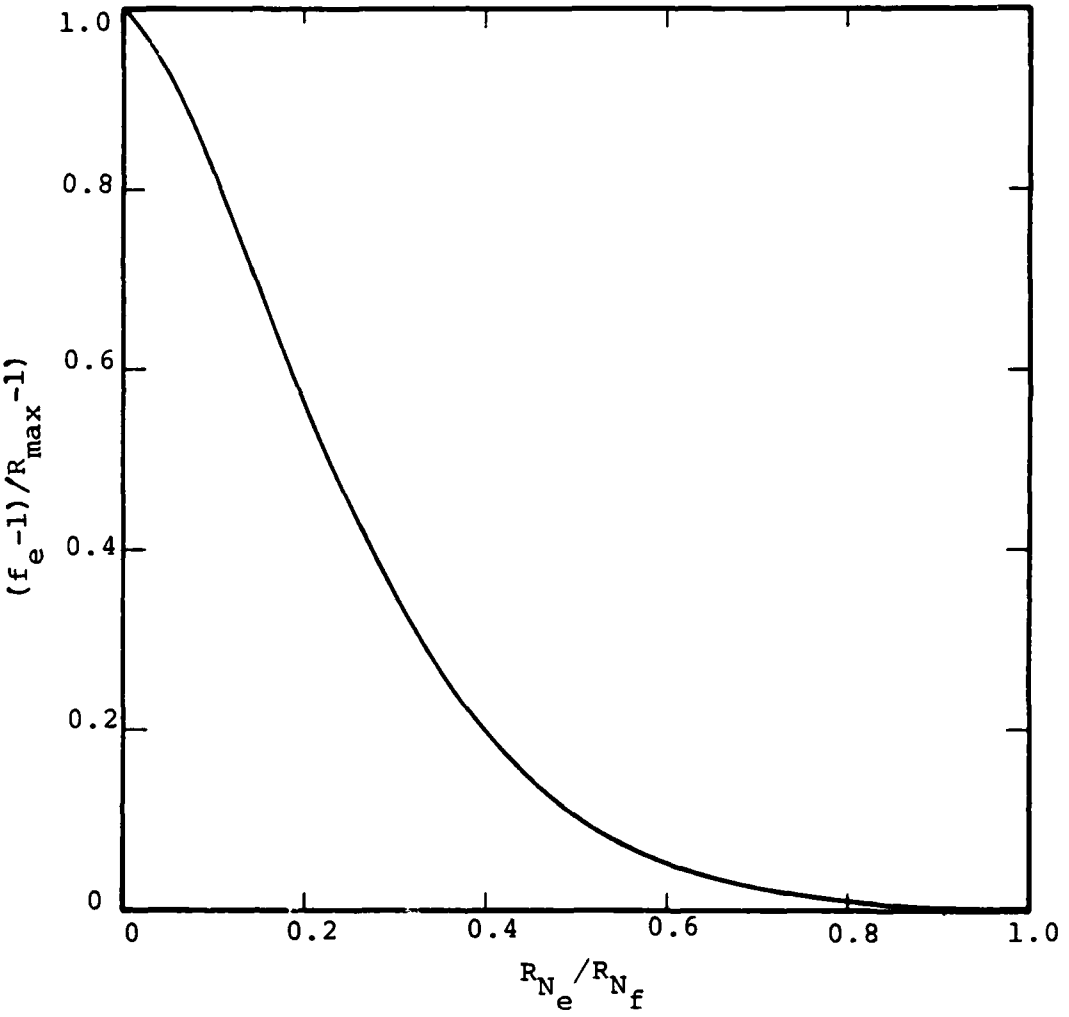

Figure 13. Recession Rate Increase Due Entropy Swallowing

intersection points are observed. Hence, the bow shockwave apparently performs a body smoothing function as the effective nose radius decreases and the shockwave becomes more oblique and closer to the body surface. Development of the three-dimensional flow field influence coefficients required to determine the effect on surface pressure and edge velocity gradient is beyond the scope of the present effort. A simple empirical approach has been developed to account for this effect by modifying the turbulent recession rate of each gouge based on the deviation of its frusta intersection station from an average intersection station corrected for nosetip cant. The average intersection station is calculated from an angular weighted average of the gouge intersection sections in vehicle coordinates

$$\bar{z}_4 = \sum_{i=1}^{20} z_{4i} \Delta\phi'_i / 2\pi \tag{60}$$

and the deviation from the average is

$$\Delta\xi_i = (z_{4i} - z_{fi})/R_{N_e} \tag{61}$$

where

$$z_{fi} = \bar{z}_4 - [r_{4o} + (\bar{z}_4 - z_{4o})\tan\theta_f]\sin\Psi\cos(\theta'_i - \theta_\Psi) \tag{62}$$

and the initial sphere-cone tangent point is

$$r_{4o} = R_N\cos\theta_f$$

$$z_{4o} = R_N(1 - \sin\theta_f) \tag{63}$$

The deviation is normalized by the nosetip effective radius to account for the reduced effectiveness of the bow shock in smoothing the intersection stations prior to nosetip sharpen-

ing. The final expression obtained through comparison with the NRV nosetip and several other flight test measurements to be discussed in Section 3 is the following

$$f_{ai} = (1 + \Delta\xi_i)^{-1.6|\Delta\xi_i|/\Delta\xi_i} \tag{64}$$

where f_{ai} is the ratio of axial turbulent recession rates with and without the bow shock smoothing effect. Equation(64) indicates that gouges which intersect the frusta aft of the average value ($\Delta\xi_i > 0$) will experience a somewhat lower recession rate than those intersecting forward of the average ($\Delta\xi_i < 0$). All $\Delta\xi_i$ will eventually be reduced to zero after sufficient recession of the sharpened nosetip occurs.

Equation(65) is the final expression for the axial turbulent recession rate

$$\dot{s}_{Ti} = f_e \, f_{\theta i} \, f_{ai} \, \dot{s}_{To} \tag{65}$$

It includes the effects of the nosetip material properties of bulk density and sand roughness, entropy swallowing, and three-dimensional asymmetries and is calculated for each of the nosetip segments, respectively. Integration of the turbulent recession rate with time for each turbulent segment yields the parameter z'_{To} which defines the turbulent gouge location in nosetip coordinates

$$z'_{Toi} = z'_{Totri} + \int_{t_{tri}}^{t} \left\{ \dot{s}_{Ti} - \dot{s}_L + \cot\theta_T \left[\left(\frac{dx_s}{dt}\right)^2 + \left(\frac{dy_s}{dt}\right)^2 \right]^{1/2} \cos(\phi'_i - \phi_{d\Delta}) \right\} dt \tag{66}$$

where

$$\phi_{d\Delta} = \arctan \left(\frac{dy_s}{dt} \Big/ \frac{dx_s}{dt} \right)$$

is the angle of the direction of offset movement. The last term of the integrand of Equation(66) corrects for the movement of the offset location so that in vehicle coordinates

$$\frac{dz_{Toi}}{dt} = \dot{s}_{Ti}$$

The integral in Equation(66) is evaluated from the time of transition (t_{tri}) of each segment. The initial z' axis intercept at transition, z'_{Totri}, is determined by requiring that the turbulent flow line segment be initially tangent to the hemispherical laminar segment unless the tangency point would be at a value of r' greater than the laminar segment-frusta intersection point. This point is defined by the equations

$$r'_{Tro} = \min \{ r'_4, R_1 \cos\theta_T \}$$

$$z'_{tro} = R_1(1 - \sin\theta_T)$$

and the required intercept is

$$z'_{Totri} = z'_{tro} - r'_{tro}\cot\theta_T \qquad (67)$$

The turbulent gouges formed early in the nosetip transition process have also been observed to grow in angular width as well as depth as nosetip recession proceeds. The present nosetip shape change model includes the growth in angular width by increasing the width of the turbulent gouges, $\Delta\phi_i$, proportional to the turbulent ablation rate until either the turbulent gouge segments meet adjacent turbulent segments or adjacent laminar segments experience boundary layer transition. Adequate representation of the turbulent width growth rate has been obtained with the equation.

$$\frac{d\Delta\phi'_i}{dt} = \dot{s}_{Ti}\sin\theta_T/R_N \qquad (68)$$

where $\dot{s}_{Ti}\sin\theta_T$ is the turbulent ablation rate normal to the gouge surface. The rate given by Equation(68) is one-half the maximum rate for a uniformly expanding half-cylindrical gouge and reflects the lower pressure on the gouge sides compared to the bottom.

2.2.3 Boundary Layer Transition

Boundary layer transition from laminar to turbulent flow continues to be the subject of considerable research. The most recent review is contained in Reference 10 which compares five semi-empirical roughwall transition laws with experimental transition data obtained in ballistic-range experiments. The conclusion of the review was that the correlation of Reference 5 "best represents the physics of roughness dominated transition on blunt bodies in hypersonic flow". The transition law of Reference 5 was derived from Mach 5 wind tunnel data for roughened surfaces with no blowing (see Figure 14) and is based on the concept of a critical Reynolds number for vortex shedding from the top of a roughness element, i.e.,

$$[Re_k]_{tr} = [\rho_k u_k\, k/\mu_w]_{tr} = \text{constant} \qquad (69)$$

Note that the Reynolds number is to be evaluated at the roughness height k in the boundary layer while the viscosity is evaluated at the wall temperature. As seen in Figure 14 this approach successfully correlated the zero-ablation, wind tunnel test data when the body curvature effect proposed by Van Driest (Reference 12) is used to evaluate an effective k for use in Equation(69)

$$k = k_m(1 + 350k_m/R_N)^{-1} \qquad (70)$$

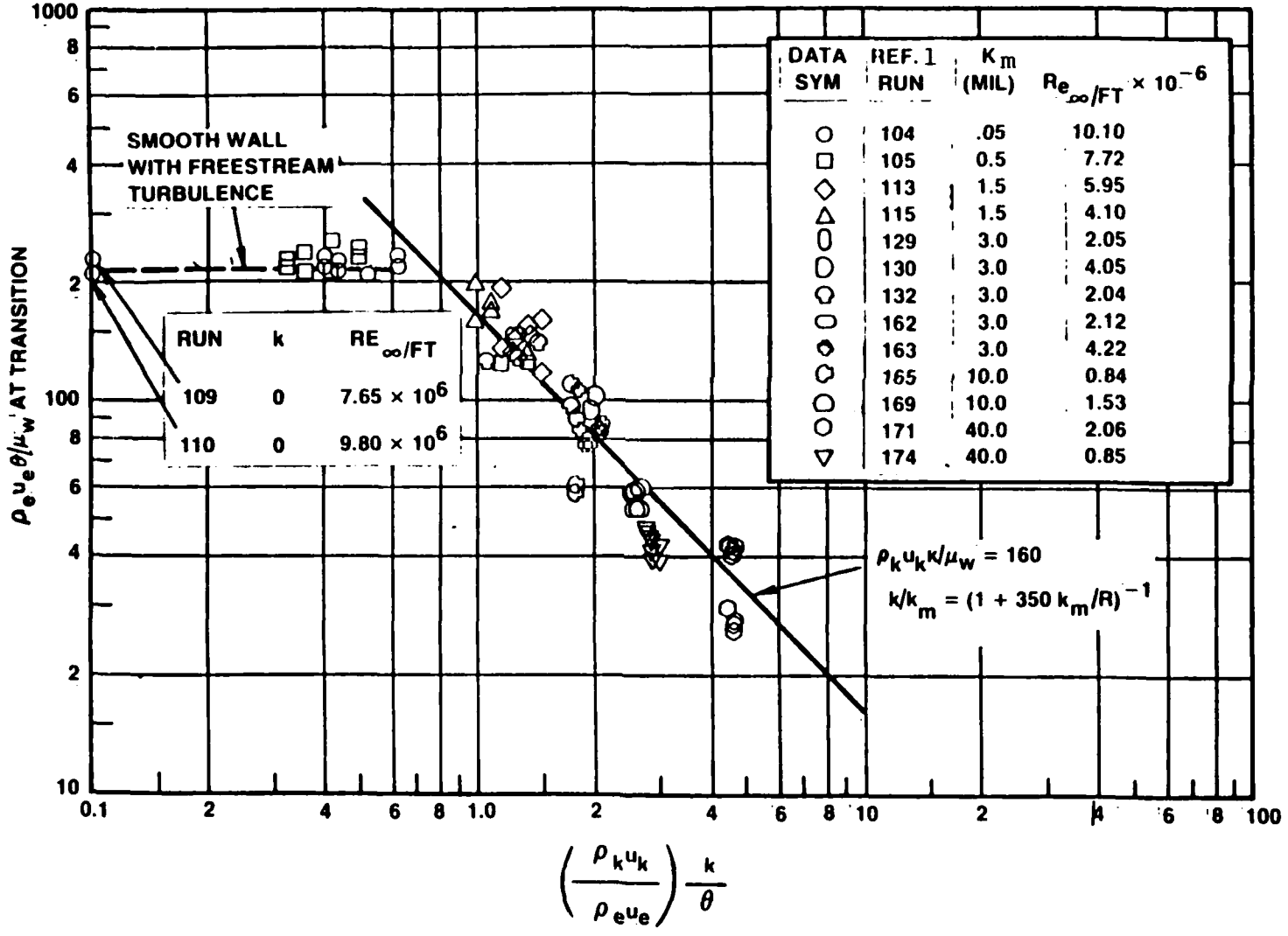

Figure 14. Transition Criteria for Rough Surfaces

where k_m is the actual roughness height of the surface. The best-fit value of the constant in Equation(69) was found to be 160 for the data of Reference 11.

The conclusion presented in Reference 10 noted above was obtained from comparison of the five transition laws with ballistics-range experimental data. Details of the ballistic-range data were obtained from D.C. Reda (Reference 13). Calculations were performed using the COBRA computer code for 56 independent transition point measurements encompassing five materials (three bulk graphites and two carbon-carbons) three nose radii, and 28 shots. It was found that the use of the curvature correction yielded a fairly good fit of the data when the value of the constant in Equation(69) was equal to 150. However, a better correlation was obtained if the curvature-correction term was ignored, i.e., if $k=k_m$, and the constant's value was approximately 190. The calculations were independently checked at by M. L. Finsen of PSI (see Reference 10) and were found to be within 5%.

Several points should be made concerning these results. First, the curvature-correction term approximately accounts for the increased stability of the laminar boundary layer due to the slightly positive value of dp/dy in a boundary layer on a convex body with accelerating flow and no-blowing. The experiments of both Van Driest and Reference 11 did not include surface blowing, hence the curvature-correction term is appropriate. The ballistics-range experiments, however, include surface blowing effects from ablation of the graphite materials (primarily due to diffusion-controlled oxidation). Surface blowing changes the sign of dp/dy to negative in the laminar boundary layer and therefore negates the effect of curvature on stability. This may explain the improved cor-

relation of the ballistics-range data when the curvature-correction term is not used.

Second, the effect of freestream turbulence on laminar boundary layer stability may influence the value of the constant in Equation(69) slightly. While the principal effect of freestream turbulence has been observed to be a reduction in transition Reynolds number for smooth walls, some effect on rough walls has also been postulated. In fact, based on the turbulence model calculations of Reference 14 an increase in the constant by about 50 per cent is expected when comparing zero turbulence freestream predictions with 2% turbulence intensity predictions. The latter figure was chosen in that study because transition predictions for that level of turbulence intensity most nearly matched the wind tunnel experimental data of Reference 11. These calculations included the curvature effect implicitly but were for zero blowing. The increase in the constant from 160 to 190 observed in the ballistics-range experiments may therefore be due to the reduction in turbulence intensity associated with free flight experiments.

The third point of interest is the observation in Reference 10 that the carbon-carbon materials tested were more effective in tripping the laminar boundary layer than optical measurements of their surface roughness would indicate while bulk graphite materials were not. This may be due to the complex surface roughness pattern developed on woven composite materials as opposed to the more uniform, distributed random roughness developed on bulk graphites as proposed in Reference 10. Alternately, the difference may be due to the difference in ablation response of the more oriented graphitic structure of composite materials compared to turbostatic bulk graphite. The graphite fibers with their highly oriented crystallographic structure are

known to cause substantial variations in ablation response (especially in the oxidation regime) resulting in significant preferential etching of fiber bundles and, by extension, a non-uniform blowing distribution.

In summary, while significant progress has been made in developing an adequate rough surface transition law for graphitic nosetip materials, several important issues remain; not the least of which is quantifying a laminar roughness height value for use in any proposed law. For the present investigation, the method of Reference 5 will be adapted with measured roughness heights uncorrected for enhanced tripping effectiveness. This approach has resulted in good agreement with flight test recession data for both bulk graphite and carbon-carbon composite materials (Reference 8 and 15).

In order to apply Equation(69) to the prediction of boundary layer transition, boundary layer profiles of velocity and density, wall temperature, and sonic point momentum thickness and Reynolds number are required. The approach taken here is similar to that described in Reference 8. In order to evaluate the local mass flux at the tip of the roughness element, $\rho_k u_k$, the laminar boundary layer velocity and density profiles are determined by assuming that distributed roughness does not appreciably modify the smooth wall boundary layer profiles prior to transition. The Pohlhausen fourth-degree velocity profile is used for flows with pressure gradient, e.g.,

$$u/u_e = 2\eta - 2\eta^3 + \eta^4 + \Lambda[\tfrac{1}{6}\,\eta(1-\eta)^3] \qquad (71)$$

where the shape factor,

$$\Lambda = \frac{\rho_e}{\rho_w}\,\frac{\delta_1^2}{\nu_e}\,\frac{du_e}{ds}$$

has the value 4.72 in the stagnation region of a sphere and

$$\delta_1 = \int_o^\delta \frac{\rho}{\rho_e}\,dy \qquad (72)$$

$$\eta = \frac{1}{\delta_1} \int_o^y \frac{\rho}{\rho_e} dy \qquad (73)$$

In order to evaluate the density profile, compressible laminar boundary layer similar solutions with pressure gradient have been examined. It was found that if the zero-pressure gradient ($\Lambda = 0$) compressible velocity profile given by Equation(71) is used in conjunction with the Crocco relation an acceptable approximation to the temperature profile results. Hence, the density profile is approximately

$$\frac{\rho}{\rho_e} = \left(\frac{T}{T_e}\right)^{-1} = \left[\frac{T_w}{T_e} + \frac{T_r - T_w}{T_e} \tilde{u} + \frac{T_e - T_r}{T_e} \tilde{u}^2\right]^{-1} \qquad (74)$$

where

$$\tilde{u} = 2\eta - 2\eta^3 + \eta^4$$

The above relations for the velocity and density profiles are easily related to the compressible boundary layer momentum thickness by

$$\theta/\delta_1 = \frac{37}{315} - \frac{\Lambda}{945} - \frac{\Lambda^2}{9072} = 0.110 \qquad (75)$$

for Λ equal to 4.72. From Equation(73) one has

$$\frac{\delta}{\delta_1} = \int_o^1 \frac{\rho_e}{\rho} d\eta = \int_o^1 \frac{d\eta}{\frac{T_w}{T_e} + \left(1 - \frac{T_w}{T_e}\right)(2\eta - 2\eta^3 + \eta^4)} \qquad (76)$$

for $T_r \sim T_e$ in the stagnation region. Carrying out the integration yields the following approximate result

$$\delta/\delta_1 = 0.7 + 0.3\ T_w/T_e \qquad (77)$$

and with Equation(75)

$$\delta/\theta = 6.364 + 2.727\ T_w/T_e \qquad (78)$$

In order to evaluate η numerical calculations have been carried out as a function of y/θ and T_w/T_e. Figure 15 presents the results of these calulations. For y/θ values greater than 0.1 η is seen to be adequately fit by the expression

$$\eta = (\delta/\theta)^{-n}\ (y/\theta)^{n} \qquad (79)$$

where use has been made of the condition that η equals one when y equals δ. The exponent n is a function of wall temperature ratio and is adequately expressed as

$$n = 0.66 + 0.34\ T_w/T_e \qquad (80)$$

Therefore given a values of k, θ, Re_θ and T_w/T_e the roughness Reynolds number is

$$Re_k = \frac{\rho_k u_k k}{\mu_w} = \left(\frac{\rho_k}{\rho_e}\right)\ \left(\frac{u_k}{u_e}\right)\left(\frac{T_e}{T_w}\right)^{0.7}\left(\frac{k}{\theta}\right)\ Re_\theta \qquad (81)$$

where the 0.7 power-law variation for viscosity has been used.

The boundary layer properties and wall temperature ratio required for the evaluation of Equation(81) are obtained by correlation of detailed shape change results from the COBRA computer code. Figure 16 shows the correlation obtained for the wall temperature ratio of graphitic materials.

$$T_w/T_e = 47.75\ H_s^{-0.5} \qquad (82)$$

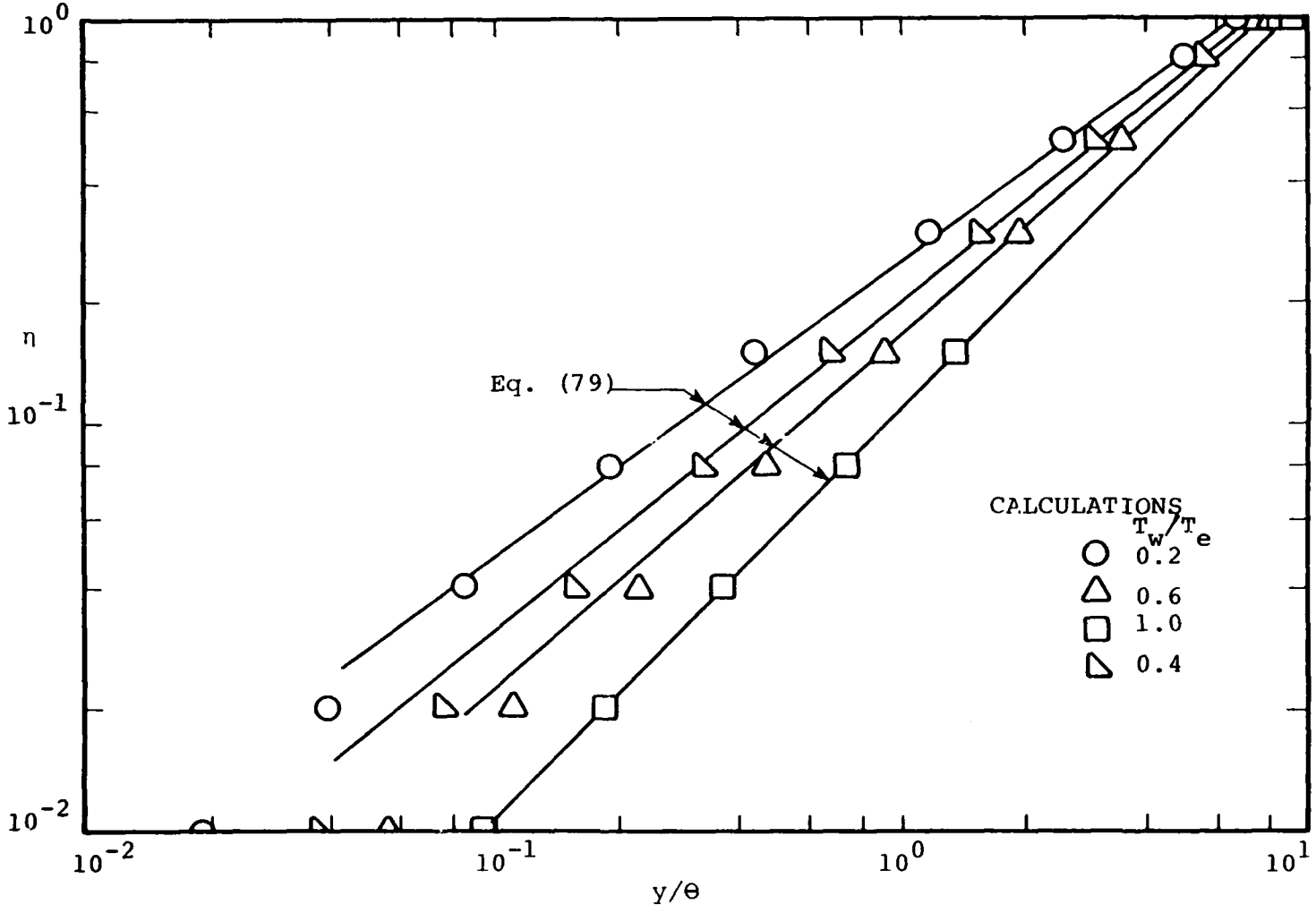

Figure 15. Compressible Boundary Layer Profiles (M = 0)

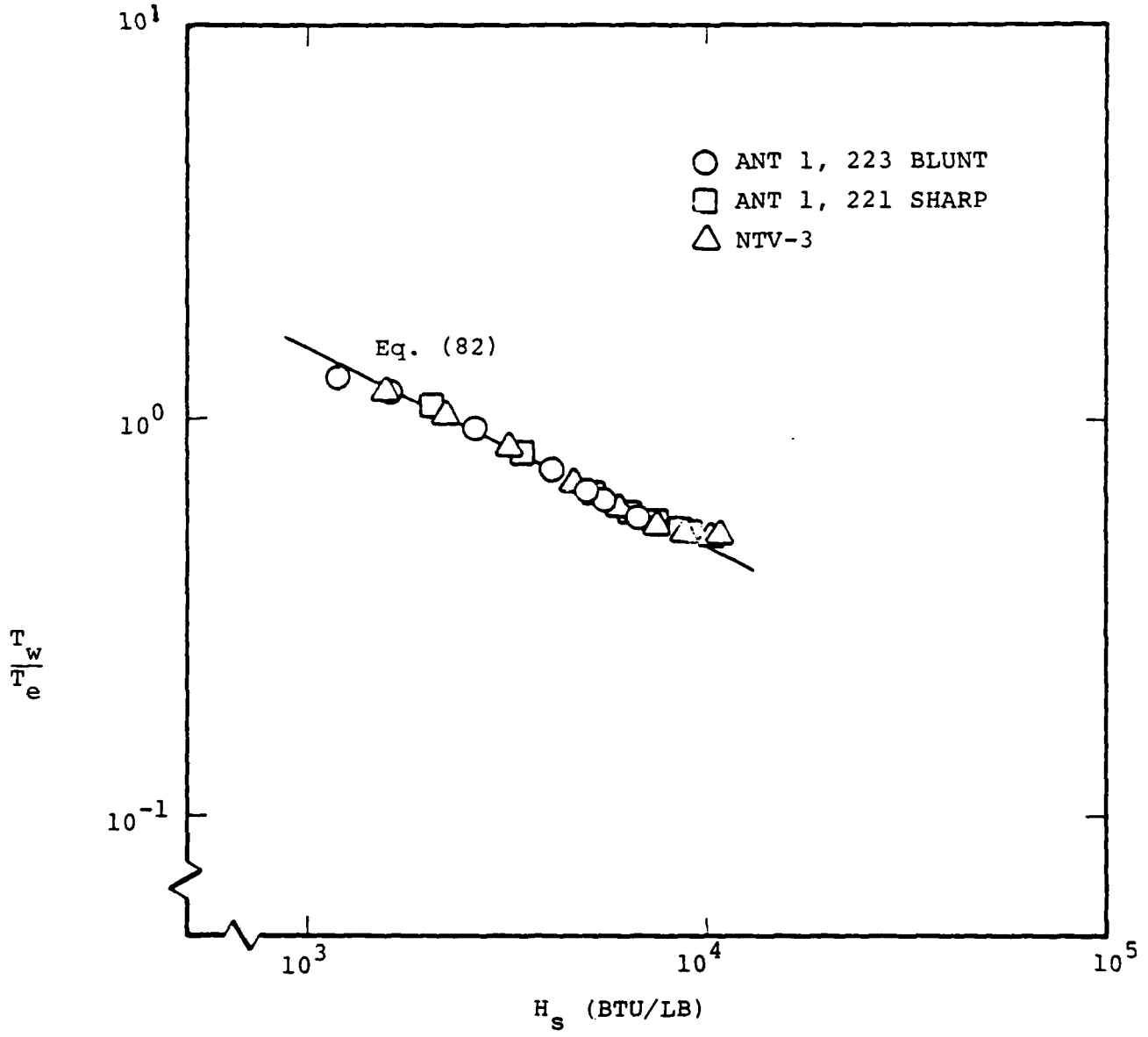

Figure 16. Wall Temperature Ratio Correlation

The high-altitude low-temperature transient heat-up regime is omitted from this figure since the wall temperature ratio which is important for transition predictions is only required at much lower altitudes.

Sonic point boundary layer properties are given by

$$Re^*_\theta = 30.79(P_s/R_{N_e})^{0.5} H_s^{-0.437} \quad (83)$$

$$\theta^* = 5.482(R_{N_e}/P_s)^{0.5} H_s^{0.392} \quad (84)$$

Figure 17 shows the correlation of the sonic point unit Reynolds number obtained using these two equations.

The location of boundary layer transition is determined by the condition that Re_k equals 160 provided that the maximum value of Re_k prior to the nosetip sonic point is greater than or equal to 200. To satisfy this condition the variation of Re_k with running length (s) measured from the stagnation point is required. The approach taken is to represent the variation of θ and $\rho_e u_e$ as simple polynominal functions of s/R_{N_e}, i.e.,

$$\theta/\theta^* = 0.73 + 0.488\ (s/R_{N_e})^{2.45} \quad (85)$$

$$\rho_e u_e/(\rho_e u_e)^* = 2.04\ (s/R_{N_e}) - 1.145\ (s/R_{N_e})^{2.67} \quad (86)$$

as seen in Figure 18. The sonic point is fixed at a s/R_{N_e} value of 0.785 via these equations.

In principle Equations(85) and (86) are sufficient to allow the calculation of Re_k for any value of s/R_{N_e} up to the sonic point. However, satisfying both the transition location and onset condition ($Re_{kmax} \geq 200$) requires a significant number of iterations on s/R_{N_e}. Since the transition location must be

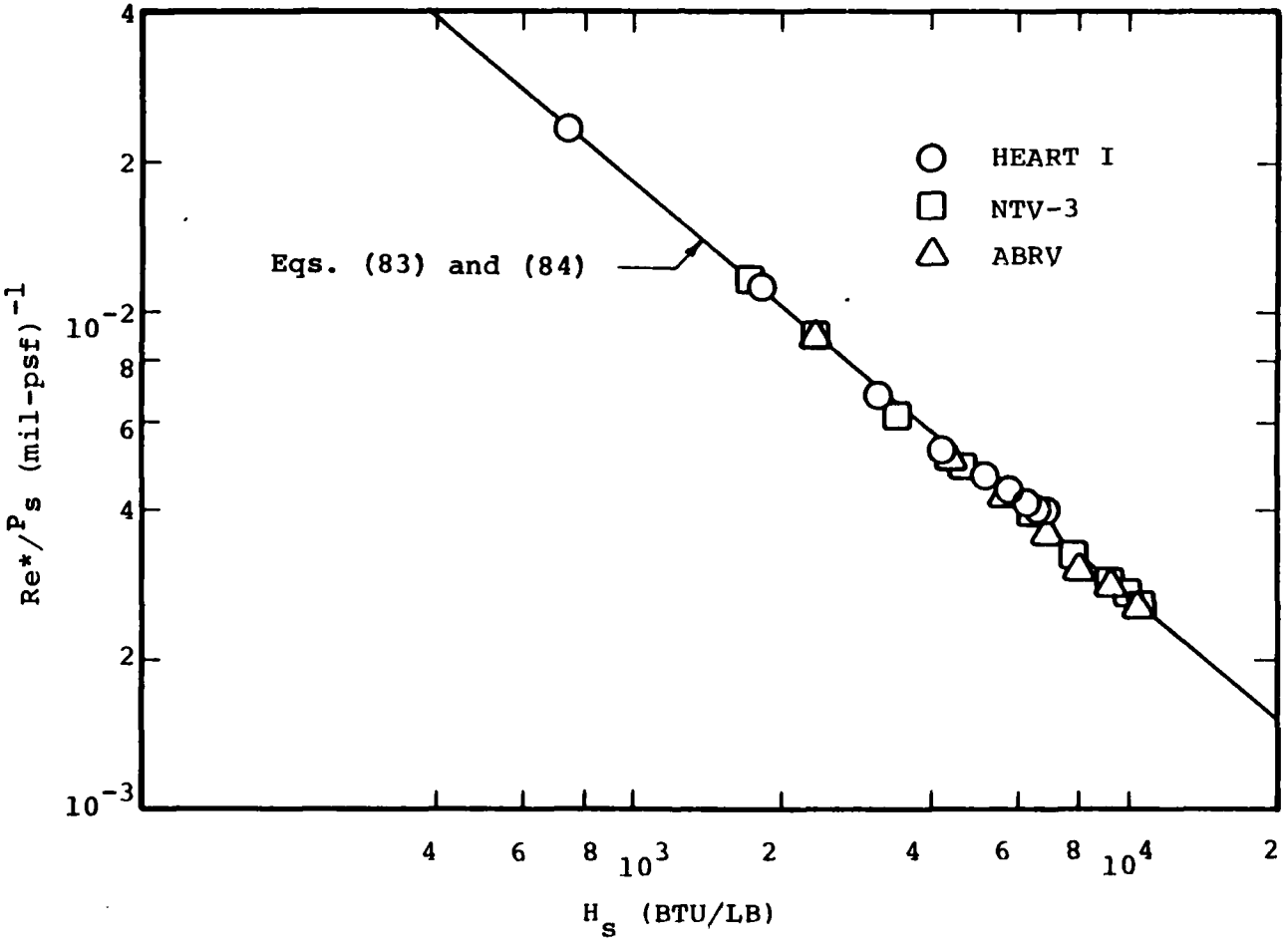

Figure 17. Sonic Point Unit Reynolds Number Correlation

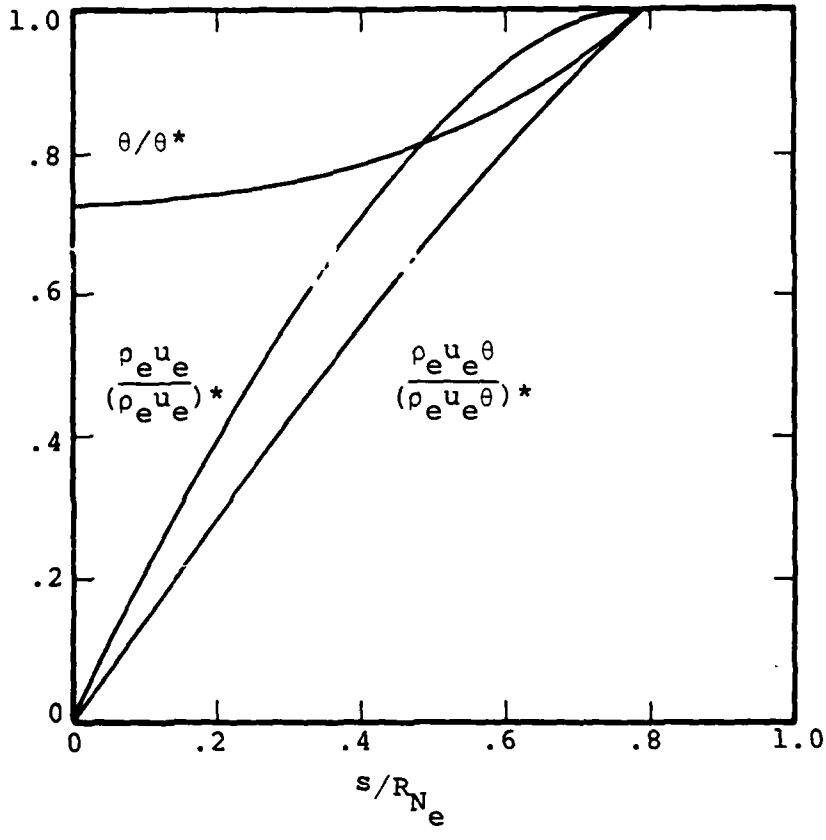

Figure 18. Laminar Stagnation Region Boundary Layer Properties

determined for all 20 nosetip rays considered, a more direct approximate method is employed. Consideration of the calculated data (see Reference 5) shown in Figure 19 indicates that the distribution of local roughness Reynolds number can be reasonably fit by a quadratic function, i.e.,

$$Re_k = a(s/R_{N_e}) - b(s/R_{N_e})^2 \tag{87}$$

The maximum value of Re_k is determined by the vanishing of the derivative of Re_k with s

$$Re_{kmax} = \frac{a^2}{4b} \tag{88}$$

at the location

$$s_o/R_{N_e} = \frac{a}{2b} \tag{89}$$

The transition location where Re_k equals 160 is found to be given by the equation

$$s_{tr} = s_o[1-\sqrt{1-160/Re_{kmax}}] \tag{90}$$

The method is completed by determining the values of a and b in Equation(87) by evaluating the value of Re_k using the full equations at an additional location chosen to be half the sonic point running length. Denoting this value by Re_{kl} one has

$$a = (4Re_{kl} - Re_k^*)/(s^*/R_{N_e}) \tag{91}$$

$$b = (4Re_{kl} - 2Re_k^*)/(s^*/R_{N_e})^2 \tag{92}$$

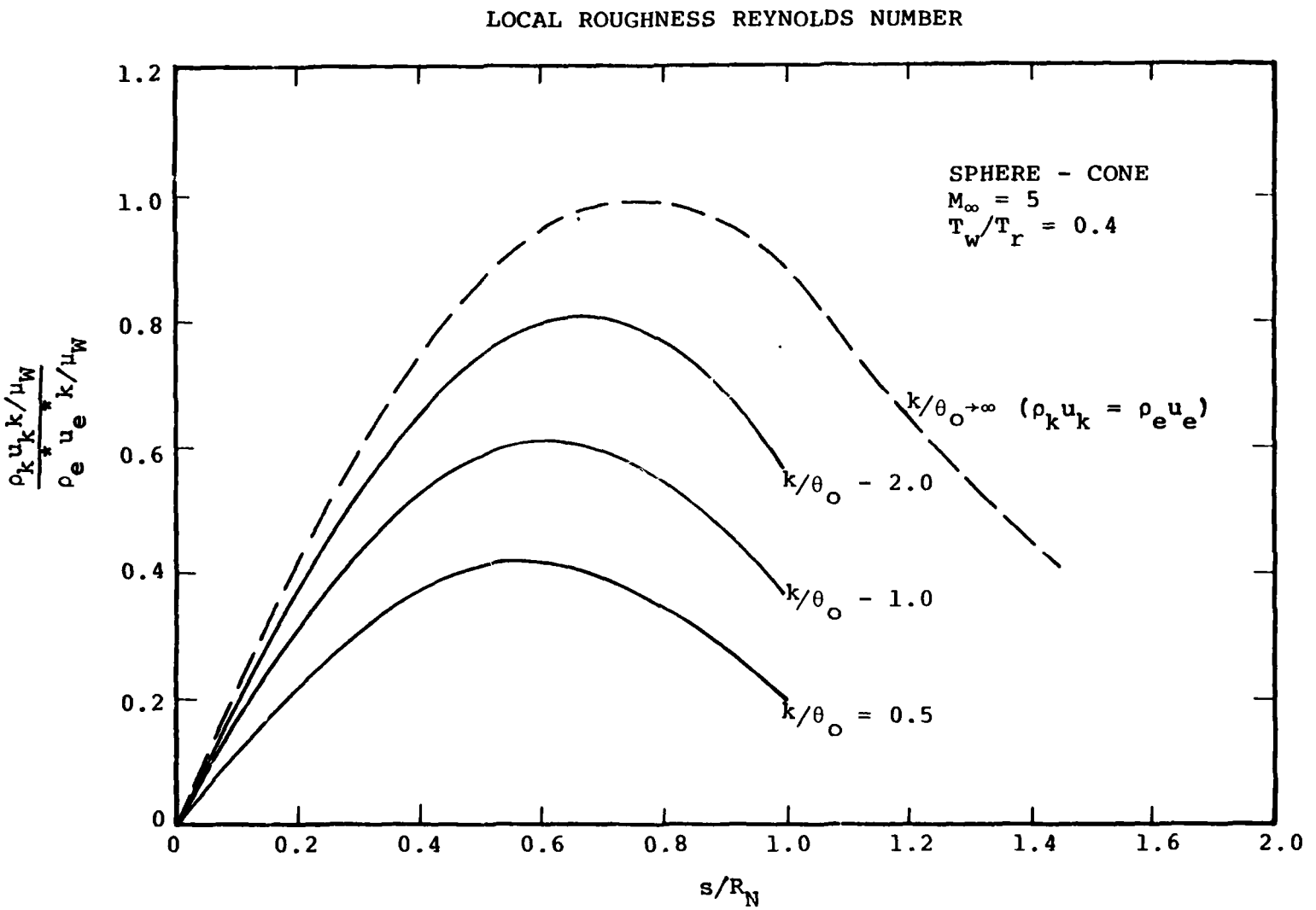

Figure 19. Roughness Reynolds Number Distribution

The effect of blowing is included via the procedure of Reference 5 by reducing the velocity at the top of the roughness elements by the ratio of laminar skin friction with and without blowing. In the present method, since blowing rate is nearly indendent of running length in the stagnation region, this is accomplished by reducing Re_{kmax} accordingly

$$Re_{kmax}|\dot{m} \neq 0 = (c_f/c_{f_o}) Re_{kmax}|\dot{m} = 0 \qquad (93)$$

where from Reference 16

$$c_f/c_{f_o} = 1 - 0.68\ B'_o + 0.08\ B'^2_o \qquad (94)$$

and B'_o is the mass transfer coefficient defined by Equation(37). The final expersion for the boundary layer transition location is

$$r'_{tr} = R_{N_e} \sin \left\{ (s_o/R_{N_e}) \left[1 - \sqrt{1 - \frac{160}{(c_f/c_{f_o}) Re_{kmax}}} \right] \right\} \qquad (95)$$

if the condition

$$(c_f/c_{f_o}) Re_{kmax} \geq 200$$

is satisfied

In general it has been found that the development of the laminar island is dependent on both the location of transition and the shape and recession rate of the nosetip. In particular, the laminar island shoulder radius, r'_2, is not necessarily equal to the transition location, r'_{tr}, because

of the finite rate at which turbulent recession forms turbulent gouges. In the present model this is accounted for by limiting the rate of change of r'_2, the laminar island shoulder radius. At initial boundary layer transition r'_2 is set equal to r'_{tro} (see Section 2.2.2). Since the transition location given by Equation(95) will be less than r'_{tro}, the laminar region radius decreases until it equals the transition radius, r'_{tr}. The rate of change in r'_2 has been related to the laminar and turbulent recession rates through the nosetip surface inclination just aft of r'_2, i.e.,

$$\theta_2 = \arctan(\dot{s}_L/\dot{s}_{To})$$

where entropy swallowing is not included in the turbulent corner recession rate since the bow shock does not become oblique until downstream of this point. Assuming the previous functional relationships for turbulent recession rate, the rate of decrease of r_2 due to turbulent recession of the surface just downstream of r_2 is $f_2\dot{s}_{To}$ where

$$f_2 = \frac{\sin^{1.6}\theta_2}{\sin^{0.6}\theta_T \cos\theta_2}\left(\frac{R_{N_f}}{\bar{r}^*}\right)^{0.2} \qquad (96)$$

and $\bar{r}^*$ is the average radius for subsonic flow defined by the angular weighted average of r^*_i (see Section (2.2.1)

$$\bar{r}^* = \sum_{i=1}^{20} (\Delta\theta'_i)\ r^*_i/2\pi$$

In order to compensate for changes in the nosetip axis system origin, the shift in Δ must be accounted for as in Equation(66),

so that r'_2 is given by

$$r'_{2i} = r'_{troi} - \int_{t_{tri}}^{t} \left\{ f_2 \dot{s}_{To} + \left[\left(\frac{dx_s}{dt} \right)^2 + \left(\frac{dy_s}{dt} \right)^2 \right]^{1/2} \cos(\theta'_i - \theta_{d\Delta}) \right\} dt \qquad (97)$$

Equation(97) applies until r'_{2i} equals the transition location given by Equation(95); thus r'_{tri} is the minimum value for the laminar shoulder radius.

2.3 MATERIAL REPRESENTATION

The occurance of boundary layer transition is directly related to the size (and perhaps the shape and pattern) of the surface roughness developed on graphitic nosetip materials under laminar ablation conidtions. In addition convective heat transfer rates are dependent on surface roughness; in particular, the turbulent heating rate increases as the equivalent sand roughness of the surface increases. Description of the nosetip material surface roughness characteristics is, therefore, of critical importance for the present model development.

It is well-known that the heights of surface roughness elements developed over the surface during ablation are not equal at any instant in time (Reference 4, 5, 8 and 17). Optical measurements on post-test ablation models which have been sectioned and mounted using metallurgical techniques (see References 18 and 19 for a good description of this technique) have indicated that a wide range of element heights are present. For instance, Figures 20 and 21 (from Reference 19) present microroughness measurements made on samples of two different fine-weave carbon-carbon materials - a rough 223 PAN material processed to yield high altitude transition (HAT) and a relatively smooth PAN fine-weave pierced fabric (FWPF) material.

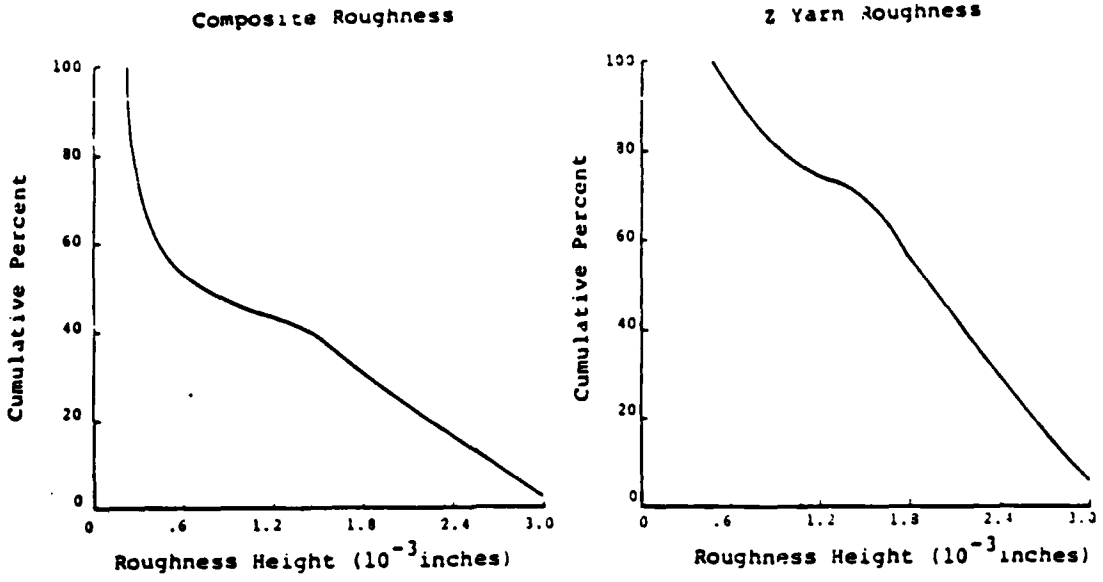

Figure 20. Microroughness Height Distribution For HAT 5 (223 PAN, HAT, Turbulent)

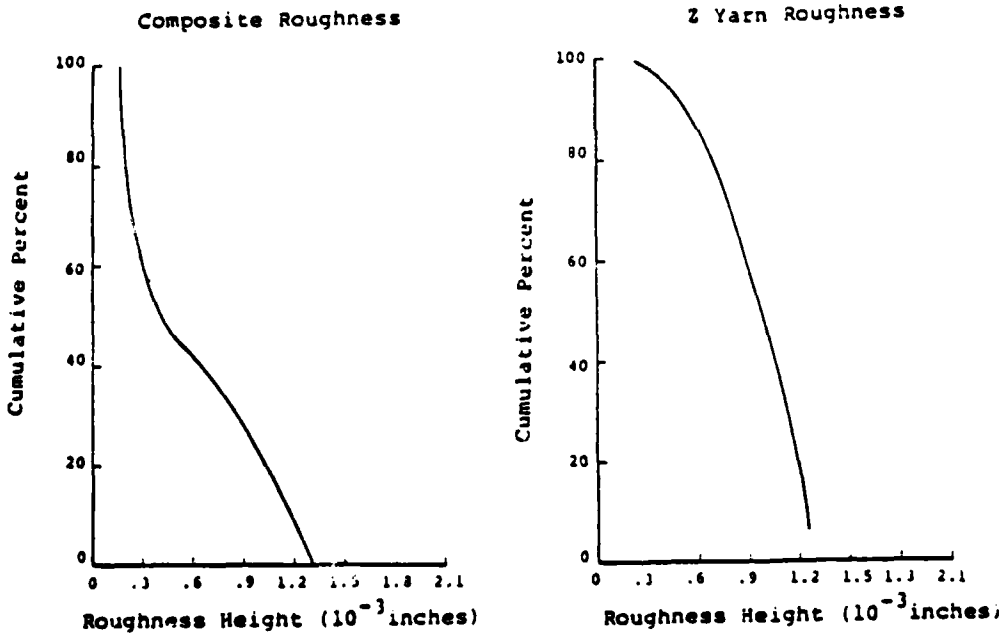

Figure 21. Microroughness Height Distribution For PF928-HS2 (FWPF PAN, Laminar)

These cumulative relative frequency graphs indicate the cumulative percent of roughness elements which have a height greater than a given value. The composite roughness height is defined for woven composite material as the frequency weighted average of roughne heights measured on each of the three exposed constituent materials, z-yarn ends, transverse yarns, and matrix material. The differences in the maximum and median values of roughness height and the width of the distributions are readily apparent.

This section describes the pertinent material properties which are included in the asymmetric shape change model with particular emphasis on the surface roughness modeling.

2.3.1 Laminar Roughness

The nonuniformity in ablation surface roughness element heights dictates the asymmetry of the transition front and the resulting asymmetric nosetip shape change. Both direct measurements of transition front asymmetries (see Reference 20) and transition pressure variability (see Reference 21) support this hypothesis. In the present model laminar roughness height values (k_i) are assigned to each of the initial 20 nosetip segments individually in order to simulate the nonuniformity of the surface roughness height distribution. The values of k_i are sampled from a population distribution which represents the specific nosetip material to be analyzed. During early reentry as nosetip stagnation pressure increases each nosetip segment experiences transition onset and movement according to the segment's value of k_i and the transition law discussed in Section 2.2.3. This section presents the techniques used to represent the laminar roughness element height populations and discusses selected material data studies related to transition and roughness characteristics.

As indicated earlier surface roughness characteristics of graphitic materials tested under laminar flow conditions have been extensively measured from post-test ablation models.

Measurements on bulk graphite materials have generally indicated a nearly Gaussian distribution of roughness element heights. Similar measurements for surface roughness patterns developed on woven carbon-carbon composite materials have exhibited a more complex distribution. Each surface constituent develops a roughness distribution pattern consisting of element heights, shapes, and spacings unique to that constituent. For instance, as might be expected, exposed z-yarn ends exhibit relatively large, thin, closely-spaced elements consisting primarily of groups of filaments. Transverse yarn elements tend to be rounded and of small size with nearly equal heights and widths. Exposed matrix pocket elements are irregular in shape and variable in size.

At the present time there is no specific hypothesis regarding the influence of roughness element shape and spacing on the ability of a roughness pattern to cause transition. Wind tunnel transition data such as that used to develop the transition law previously discussed generally is obtained using uniformly-sized roughness elements in a close-packed, sand grain roughness type pattern. For distributed roughness of multiple-size elements such as bulk graphite, good agreement of transition predictions with data has been noted using some measure of the average roughness height. This could be reasonably expected since the character of the surface roughness developed does indeed resemble that of sand grain roughness. For woven carbon-carbon materials, however, there is little similarity between the surface roughness pattern actually developed and that used for the experimental data on which transition laws are based. This observation has prompted Reda to suggest that the roughness height of woven composite materials for use in various transition laws be derived from experimental (ballistic-range) measurements of the materials' effectiveness in causing transition (Reference 10) much the same as the equivalent sand roughness of various distributed-roughness surfaces was originally obtained by Schlichting.

The resolution of these uncertainties is beyond the scope of the present investigation. As noted earlier, good agreement of predictions based on an average roughness height with experimental data have been obtained for carbon-carbon materials. While this may be a fortuitous result, for the present model the laminar roughness height distribution will be used uncorrected for element shape or spacing effects.

Roughness Statistics - The laminar roughness height population will be represented by a normal distribution having an average height denoted by $\bar{k}$ and a normalized standard deviation of σ_k. Because of the uncertainties noted above, it does not appear warranted to represent the slightly skewed height distributions actually measured by other than a normal distribution. In addition, measured ballistics-range transition front asymmetries have been shown to be almost normally distributed (Reference 20).

The variation of the average laminar roughness is also included in the material modeling. It has been observed that billets (and models from the same billet) of carbon-carbon material exhibit different transition behaviors. For instance, Figure 22 shows average composite microroughness measured from 23 post-test ablabtion models tested in the AFFDL 50 MW arc-jet ablation facility (Reference 18). All of the models were from standard process 223 FWCC having T-50 yarns. The distribution is approximately normal except that the minimum measured microroughness is 0.15 mils. Evidently sufficient varibility in processing exists to yield variations in the key microstructural quantities such as permeability, CVD content, etc. over a size scale on the order of the nosetip stagnation region. Inclusion of this variance in the simulation model introduces an additional vehicle dispersion source by varying the altitude of mean nosetip transition (defined by the occurrence of ten turbulent gouges) and, hence, the altitude of nosetip sharpening, drag change, and total stagnation point recession.

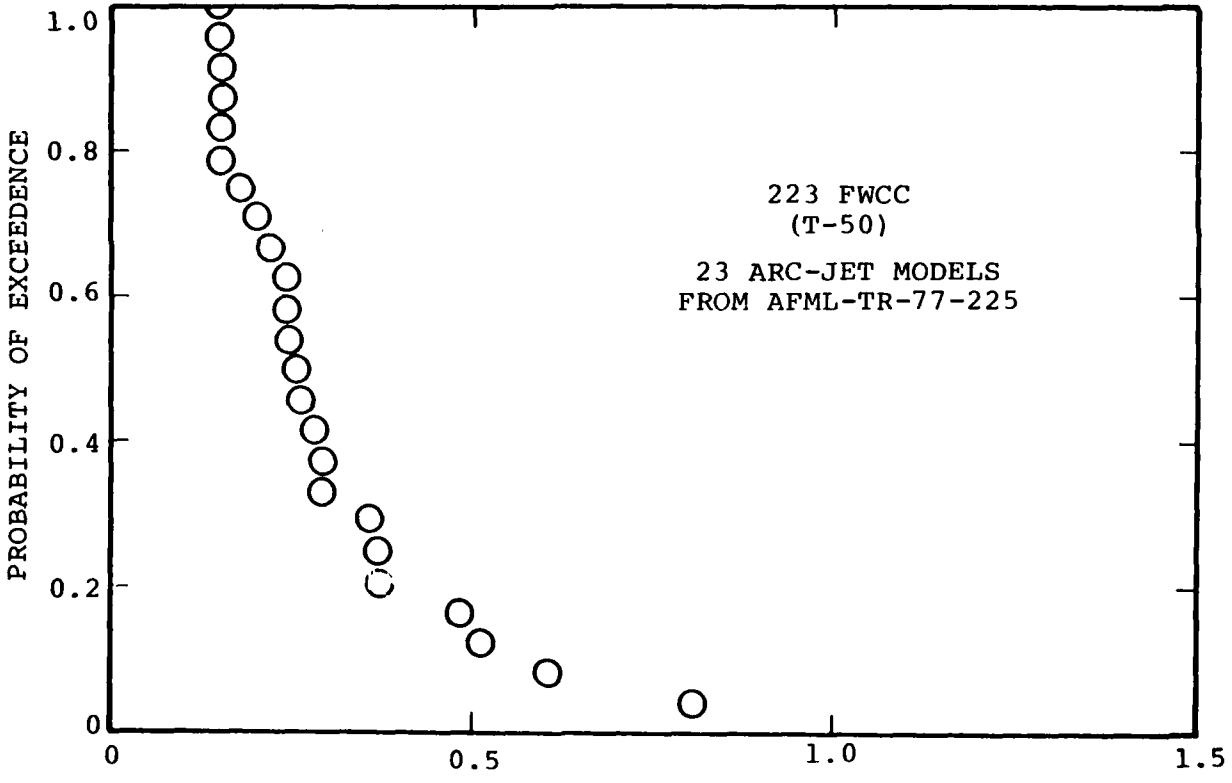

Figure 22. Variation of Average Laminar Roughness

The laminar roughness height data is represented in the model by the following equations

$$\bar{k}_j = k_L + \sigma_{\bar{k}} X_j \tag{98}$$

$$k_i = \bar{k}_j (1 + \sigma_k X_i) \tag{99}$$

where k_L is the average material laminar roughness height averaged over many nosetips, $\bar{k}_j$ is the average roughness element height for the j^{th} vehicle (nosetip) in a flight population, k_i is the roughness of the i^{th} nosetip segment, $\sigma_{\bar{k}}$ is the standard deviation of the material's average roughness, σ_k is the normalized standard deviation of the element heights, and X_i represents random deviates drawn from a normally distributed population (zero mean, variance of one).

Roughness Variation with Time - The choice of representing a nosetip segment by a single roughness value implicitly assumes that that value is representative of the critical location (or running length) where transition onset occurs. If one were to monitor an incremental surface area for a length of time, one would see a succession of roughness element height distributions as individual roughness elements grow, reach a maximum height, and then diminish as gross surface recession occurs. For sufficiently large surface areas which include a large number of roughness elements, the height distributions would approach a constant function consistent with average steady-state laminar ablation. However, as the size of the area monitored (and hence the number of elements) decreases the distributions will be significantly different from the steady-state function because of the small sample size.

There are several difficulties associated with modeling the effect of the time variance of roughness height distributions on nosetip transition. The incremental surface area appropriate to consider for derivation of individual element statistics is not known. Also, the time rate of growth of roughness elements has not been measured directly. In order to make a preliminary assessment of time varying roughness the following model was considered.

First, assume that the rate of roughness element creation and destruction is a factor of ten less than the surface recession rate. The average time for a new surface roughness element distribution is then equal to approximately twenty times the average laminar roughness height divided by the laminar ablation rate, $\dot{s}_L$. Typical values of $\dot{s}_L$ at the stagnation point of a 0.75 inch nose radius vehicle are 60 mil/sec at 65 aft altitude to 80 mil/sec at 40 kft, and the rate of vehicle descent is about 10 kft/sec. For a 0.5 mil average roughness height the time between new roughness element distributions is then approximately 0.15 seconds or 1.5 kft of altitude change. Hence, for nosetip transition occuring over about 15 kft ten surface roughness realizations might be obtained. It might be noted that for a material with larger average roughness (e.g. a HAT material) during the transition period $\dot{s}_L$ is lower and k_L is higher than above so that fewer surface roughness realizations are obtained.

Now consider the effect of ten surface roughness realizations during the transition period as opposed to one. Let the underlying roughness element height distribution be Gaussian with a mean of zero and standard deviation of one. If sets of 10 values are chosen at random from the underlying normal distribution, the distribution of the maximum value in each set is shown in Figure 23 by the symbols (fifty sets of 10 values were used). Also shown by the dashed line is the

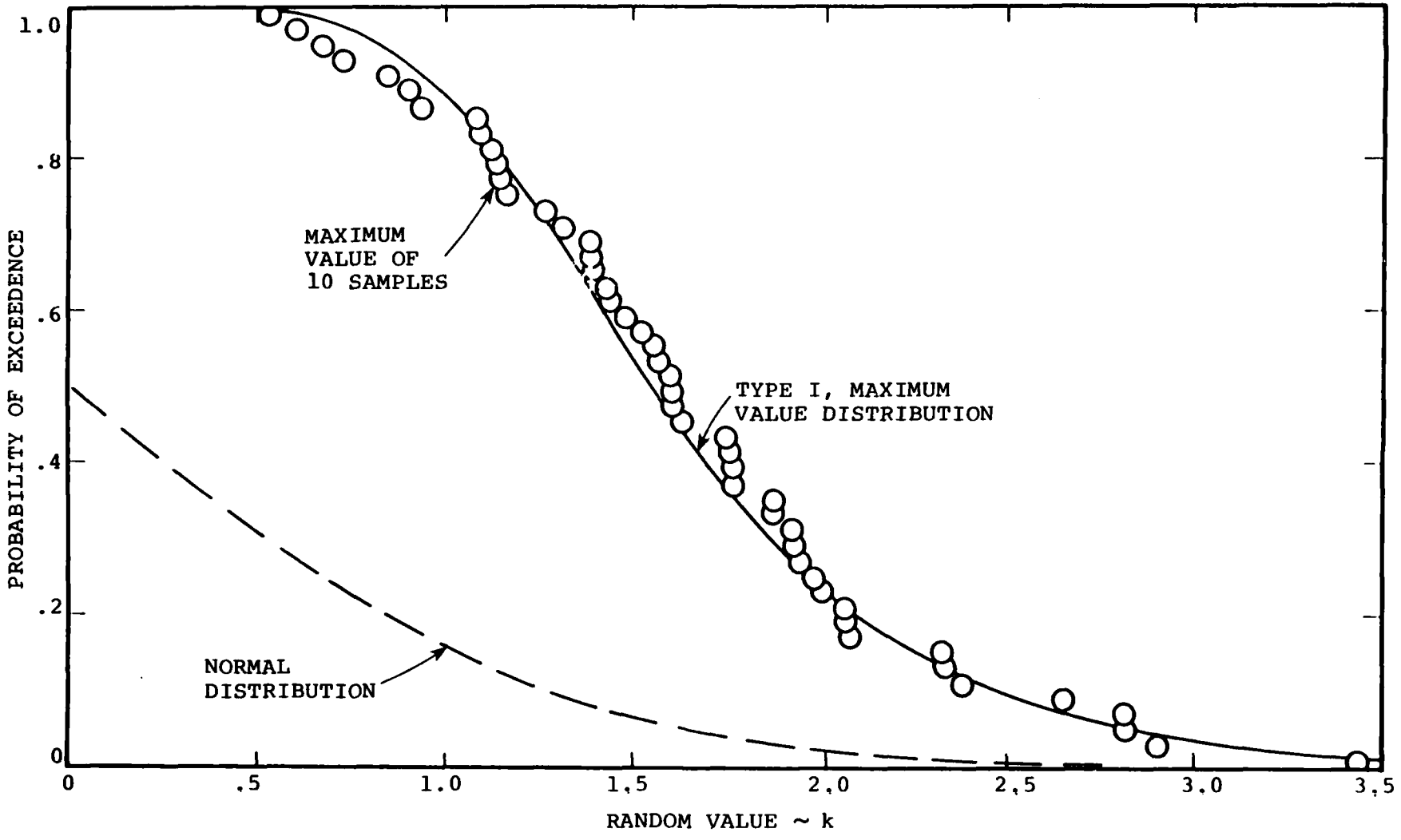

Figure 23. Maximum Value Statistics

underlying normal distribution. As expected the data shows that the maximum value of 10 samples has an expected value significantly larger than the expected value (zero) of the underlying normal distribution and a standard deviation somewhat smaller. Table 1 presents the mean and standard deviation for the distribution of the maximum value in a set of values.

Table 1

MAXIMUM VALUE DISTRIBUTION PARAMETERS

N	Mean Value	Standard Deviation
1	0	1.00
5	1.21	0.76
10	1.66	0.63
20	1.95	0.54
40	2.24	0.46

The mean value shifts continuously to higher values as the number of samples in the set increases while the standard deviation decreases like $N^{-0.2}$. Returning to the set of ten realizations, the expected value for the maximum roughness height experienced is at a probability of exceedence for the underlying distribution of about 0.05 which is near the values of 0.15 used by some investigators to correlate average transition altitudes from flight test vehicles. In fact, for about 0.15 probability of exceedence, Table 1 indicates that four realizations are required.

Figure 23 also indicates that for as little as 10 samples in a set, the Type I, maximum value distribution adequately describes the data. This distribution is derived for an underlying distribution having an exponential right-hand (maximum values) tail and a large number of samples in the set. The equations describing the distribution are the following:

$$f(x) = \frac{1}{a} \exp\left[-\left(\frac{x-b}{a}\right) - \exp\left(-\frac{x-b}{a}\right)\right]$$

$$F(x) = \int_{-\infty}^{x} f(x)\,dx = \exp\left[-\exp\left(-\frac{x-b}{a}\right)\right]$$

where a and b are constants. The expected value and variance of the distribution are $b = 9.577a$ and $1.645a^2$, respectively. Figure 24 shows the probability of exceedence (1- F) and f(x) and points out the skewness of the distribution.

Application of the maximum value distribution to 50MW ramp test data is shown in Figure 25. The data points are derived from five post-test models which had approximately 50 percent of their circumference covered by turbulent flow (~10 gouges per model). The measured data used was the radial location of the transition point for each gouge (r_t/R_n). A non-dimensional roughness height, $\tilde{k}$, was computed from the equation

$$\tilde{k} = (r_t/R_N)^{-2/3}$$

which approximates the functional dependency of the transition law for rough surfaces. The figure indicates that the type I, maximum value distribution describes the measured data fairly well.

The conclusions reached from the preliminary analysis conducted are the following: (1) Multiple realizations of surface roughness distributions developed on a reentry vehicle nosetip may be modeled if growth and decay rates for the roughness element heights are assumed. (2) Multiple realizations bias the mean roughness height which causes transition to occur at a value higher than the mean roughness height measured on post-test ablation models and reduces the effective standard deviation somewhat.

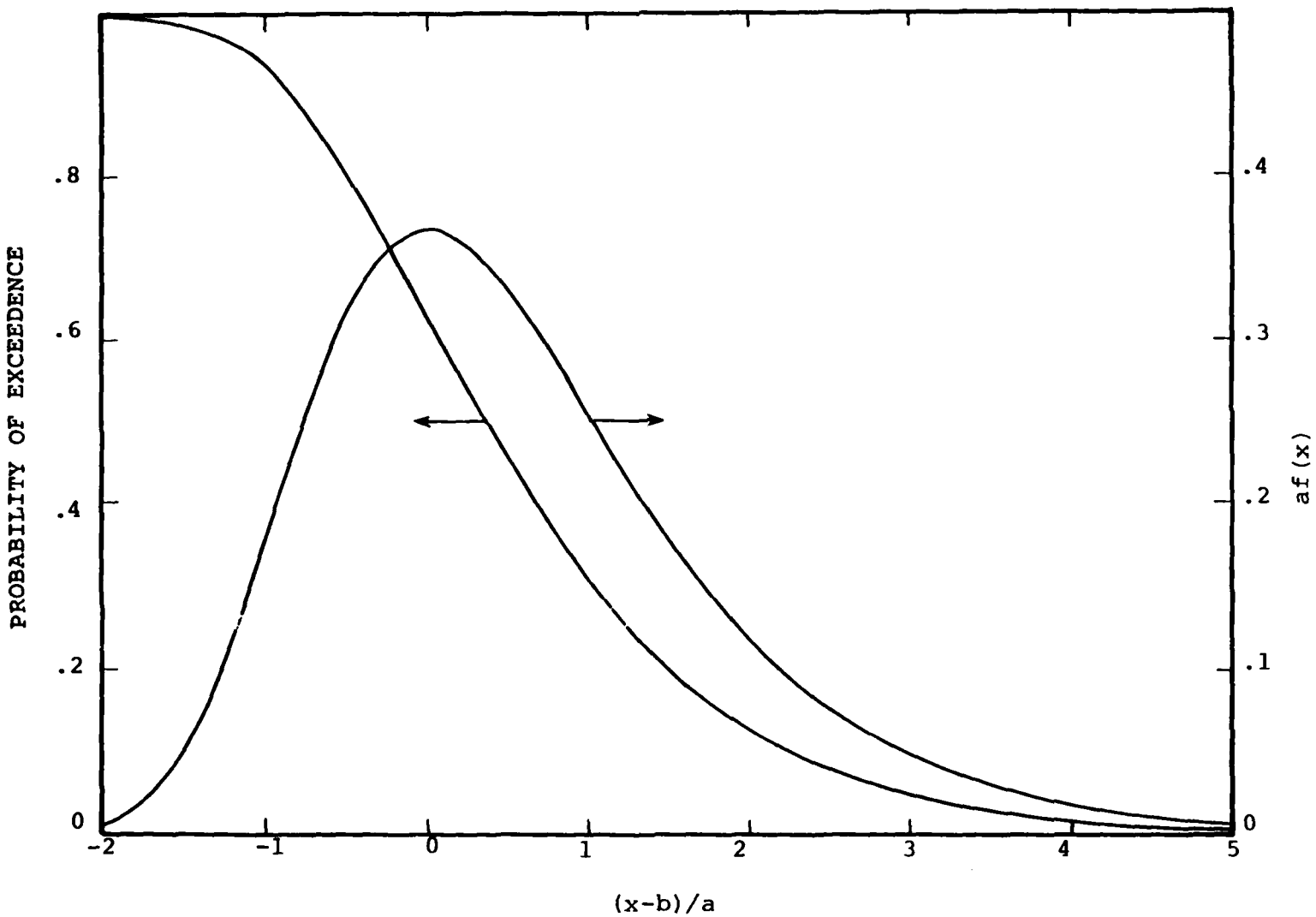

Figure 24, Type I Maximum Value Statistics

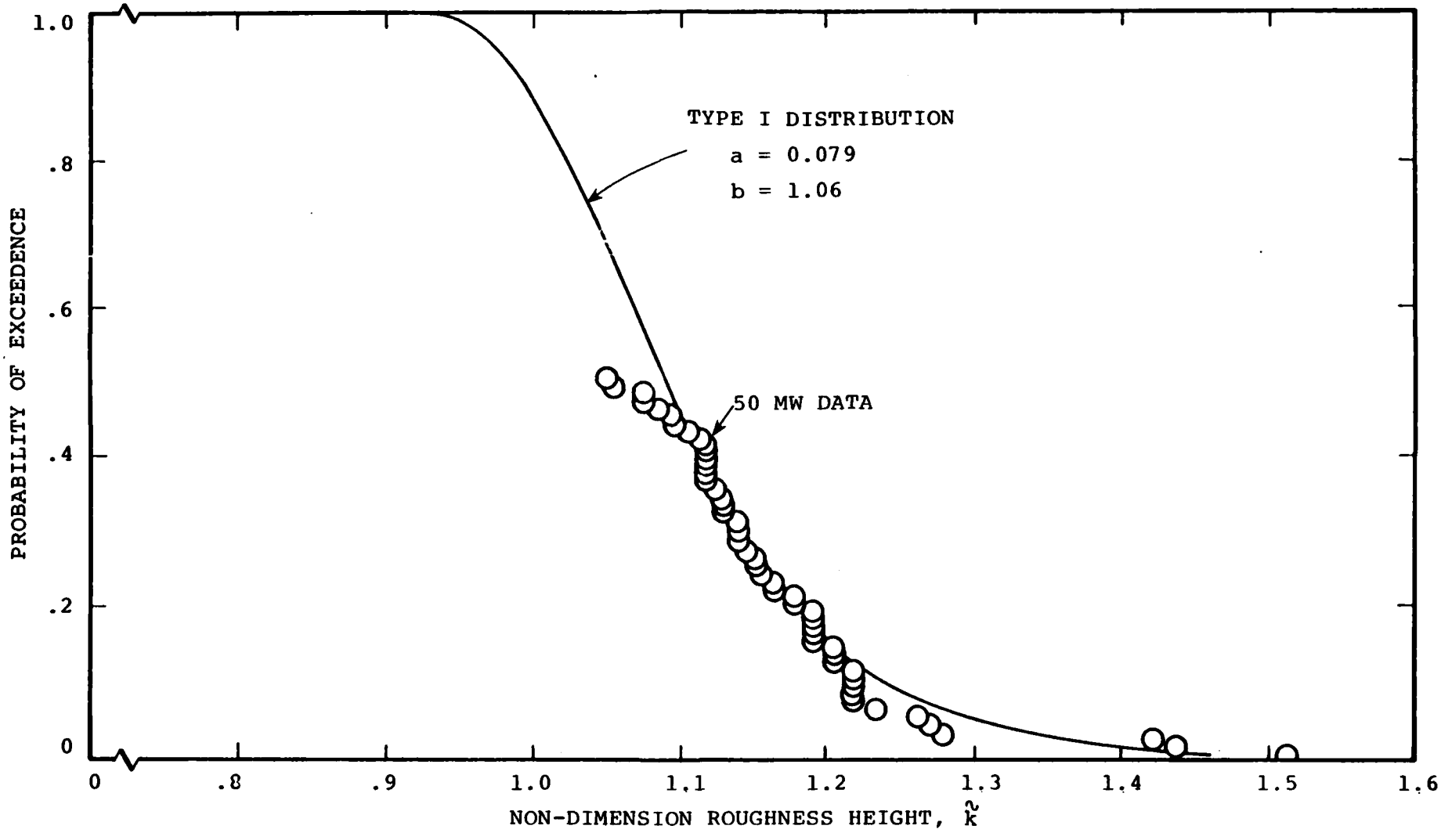

Figure 25. Derived Roughness Distribution

The inclusion of time varying roughness heights for each of the twenty nosetip segments considered in the asymmetric shape change analysis was investigated for several flight test cases (see Section 3). The assignment of a single random roughness value which is constant throughout reentry for a nosetip segment was found to overwieght the probability of nosetip segments remaining laminar. That is, if an initial low roughness height assignment for a segment occurred, that segment would tend to remain laminar unless adjacent turbulent segments grew in angular width sufficiently to completely overlap the laminar segment. Comparison with data for both the bulk graphite and carbon-carbon nosetip flight tests indicated that the persistence of laminar nosetip segements was significantly less probable than indicated by the constant roughness height model. In the modeling incorporating time varying roughness, laminar segment persistence was significantly reduced.

Based on these results time varying roughness has been incorporated in the present model by reassigning roughness heights for each laminar segment after a critical amount of stagnation point recession has occured. It is assumed that the rate of growth of roughness elements on the surface is given by

$$\frac{dk}{dt} = \pm \dot{s}_L/10 \qquad (100)$$

This rate had been previously obtained based on analysis of arc-jet ablation film data and also yielded the most consistent results for the two flight test cases considered. Equation(100) indicates that on the average a new roughness height is created after an amount of surface recession given by

$$\Delta s_{cr} = 20\ \bar{k} \qquad (101)$$

where $\bar{k}$ is the average laminar roughness height and it is assumed that the previous roughness element's height is reduced to zero before the new roughness element begins to appear. Inclusion of time varying roughness in the model significantly increases the probability of complete transition for the two flight test cases considered and provides a much better correlation of the shape change flight data.

Preferential Transition Locations - The symmetry of transition on a composite nosetip may be significantly influenced by weave geometry. For a typical 3-D orthogonal construction, transition usually occurs first on those rays at 45-deg to the principal weave axes (Reference 22). This phenomena was investigated as part of an effort to define several parameters related to asymmetric transition and turbulent gouge growth rate. The effort considered 223 fine weave carbon-carbon (FWCC) materials with either T-50 or PAN fibers. The primary data sources were peaked enthalpy ramp tests conducted in the AFFDL 50MW arc-jet facility.

The probability of preferential transition near 45° to the transverse weave axes was studied using 16 mm movies (Reference 23) and drawings of post-test model ablated shapes (References 24, 25 and 26). In the analysis of the post-test drawings the sequence of transition gouge appearance was assumed to be given by the radial position of the start of the gouge relative to the model centerline. This assumption appears to be valid when comparing the drawings with the corresponding movies. A summary of the combined movie and post-test drawing data indicating the position of the first transition gouge is shown in Figure 26. The ordinate is number of gouges and the abscissa is the angular distance of the gouge from the nearest transverse weave axis. This data shows that approximately 40 per cent of the initial gouges occur within $\pm$ 5-deg of the 45-deg position. The post-test drawings were further analyzed at later times when approximately 10 gouges had occurred covering

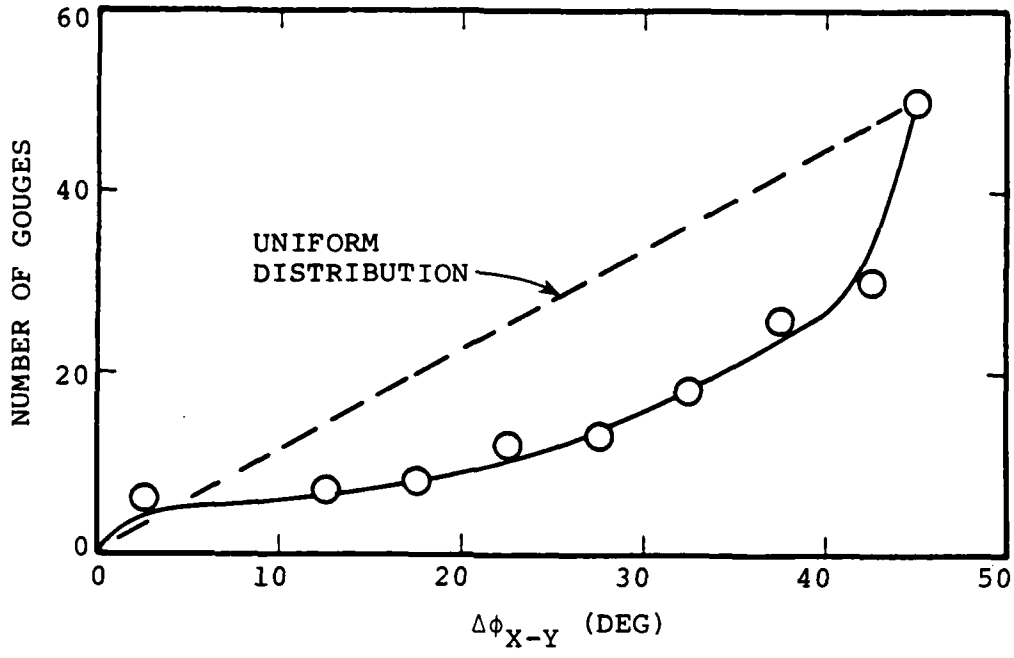

Figure 26. Position of First Gouge

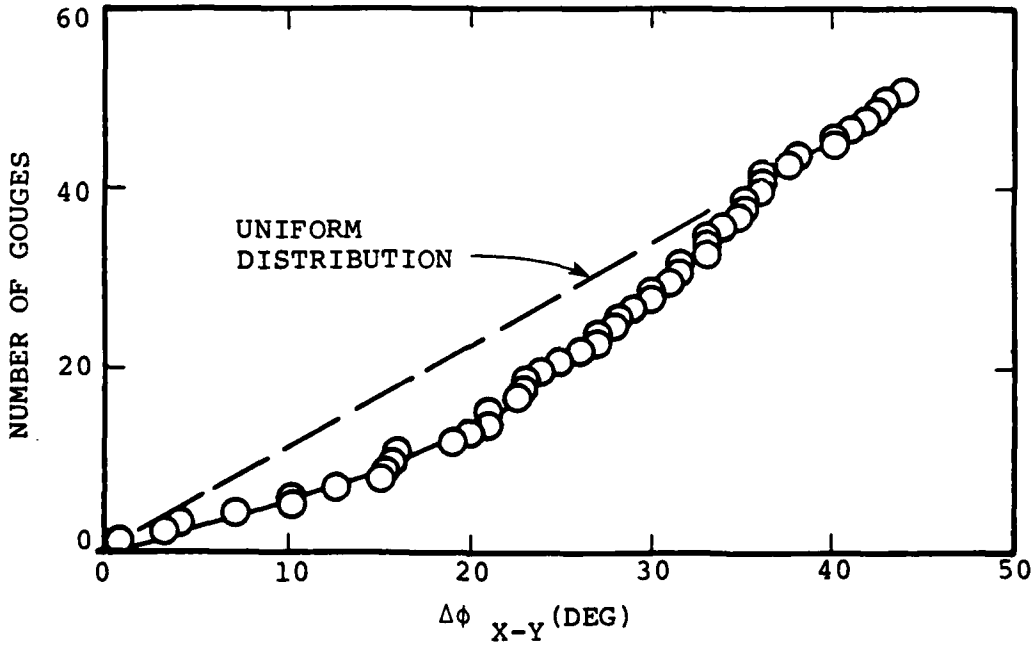

Figure 27. Positions of First Ten Gouges

about half the circumference of the nosetips. Figure 27 shows data for five nosetips and the higher probability of transition near 45-deg is still evident.

The data from these two figures indicates that transition locations on this material show significant preferential location near 45-deg. This effect may be due to the exposure of transverse yarn ends at the ablation surface. For an n-D composite with transverse yarns perpendicular to the axial yarns the relative probability of transverse yarn exposure at the surface can be derived from geometric relationships. The number of yarn ends, n_i, per unit length in the i^{th} direction which cross a nosetip ray at an angle Ψ is given by

$$n_i = N_i \sin|\theta_i - \Psi|$$

where θ_i is the angle of the yarn and N_i is the number of yarns per unit length perpendicular to the yarn direction. For several transverse yarn directions the total number of transverse yarns per unit length is given by

$$n = N \sum_i \sin|\theta_i - \Psi|$$

assuming N_i equals N for all yarn directions. For 3-D, 4-D, and 5-D composites the ratio of the number of yarns crossing off-axis to the number of crossings on a weave axis is thus

$$R_{3\text{-}D} = \frac{\sin\Psi + \cos\Psi}{\sin 0° + \sin 90°}$$

$$R_{4\text{-}D} = \frac{\sin\Psi + \sin|60° - \Psi| + \sin|120° - \Psi|}{\sin 0° + \sin 60° + \sin 120°}$$

$$R_{5\text{-}D} = \frac{\sin\Psi + \sin|45° - \Psi| + \cos\Psi + \sin|135° - \Psi|}{\sin 0° + \sin 45° + \sin 90° + \sin 135°}$$

Figure 28 illustrates these relationships. A 41 percent higher probability of yarn end exposure on the 45-deg rays is evident for 3-D composites. The 4-D and 5-D in-plane weaves are seen to substantially reduce the excess probability at off-axis locations and also to increase the number of rays of maximum yarn end exposure so that transition asymmetry should be less pronounced. Recent 50MW facility ramp test results of n-D materials appear to confirm this trend and suggest a possible method for reducing nosetip asymmetries.

Implementation of the preferential transition location data shown in Figure 26 for 223 fine weave carbon-carbon is obtained in the present model by selectively assigning the initial roughness values to the 20 nosetip segments. The nosetip segments are numbered from 1 to 20 with segment 1 extending from 0 to 18°, segment 2 from 18 to 36°, etc., where the x and y (transverse) weave axes are at 0-deg and 90-deg, respectively. Based on the data shown in Figure 26, the probability of the first transition gouge being located in a particular angular segment is given in Table 2. Figure 29 shows the cumulative probability of transition versus meridional angle.

Table 2
223 FWCC TRANSITION PROBABILITIES

$\Delta(\phi-\phi_{x-y})$,deg	Gouge Numbers	Probability
0-18	1,5,6,10,11,15,16,20	0.020
18-36	2,4,7,9,12,14,17,19	0.035
36-54	3,8,13,18	0.140

Twenty values of roughness height are randomly obtained via Equation(99) using a computer subroutine for selecting random

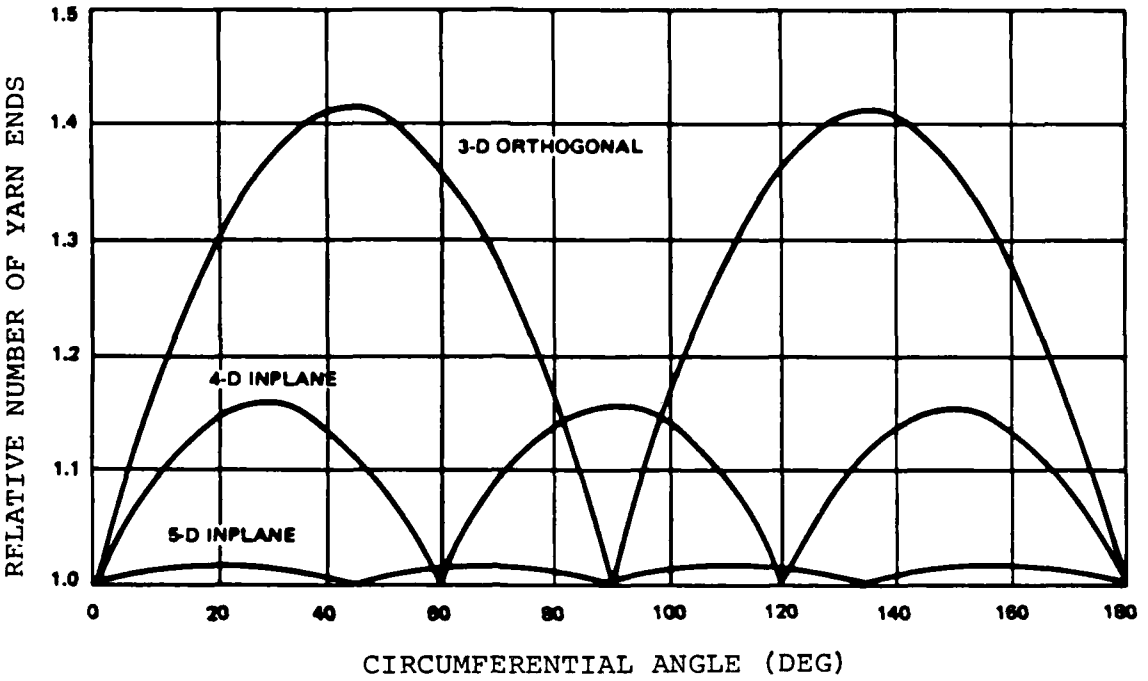

Figure 28. Preferential Transition Locations

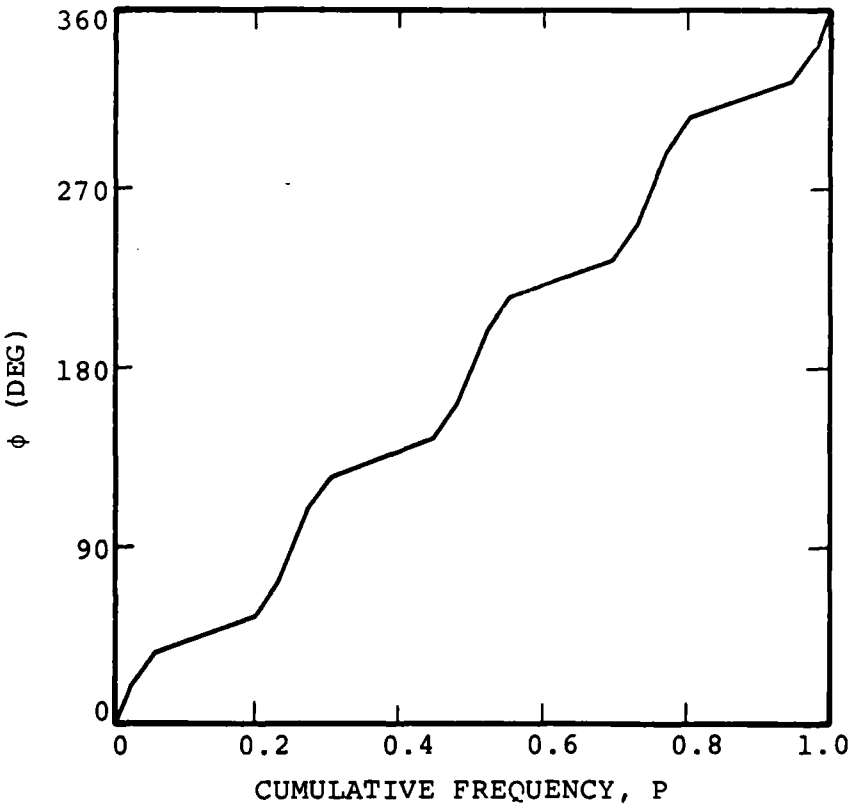

Figure 29. Preferential Transition Location for 223 FWCC

normal deviates. The twenty height values are arranged in descending order. Starting with the highest value of k_i a random number (P) uniformly distributed over the interval 0 to 1.0 is obtained. The meridional angle (or segment number) corresponding to the value of P in Figure 29 is then assigned the roughness height value, k_i. This procedure favors the assignment of the largest roughness values to the segments centered on the meridional angles 45-deg to the weave axes since the probability of one of these four segments being chosen for the highest roughness value is 0.56. The same procedure is followed for subsequent smaller roughness heights except that if a value of P is chosen which corresponds to a segment which has been previously assigned a roughness height, additional values of P are chosen until an unassigned segment occurs.

Comparison of the results of this procedure with the measured data presented in Figures 26 and 27 indicates that while the location of the first transition gouge is accurately modeled, the above procedure over-predicts the probability that all four 45-deg segments (numbers 3, 8 13, and 18) will experience transition by the tenth transition gouge (see Figure 30). This result implies that some cross-correlation between transition locations is present, i.e., that the location of turbulent gouges present influences the location of subsequent turbulence onset. In the present modeling this effect is accounted for in the procedure for varying the roughness height on a given segment as a function of time. After the critical stagnation point recession (Δs_{cr}) has occurred, a new random value of k_i for laminar segments is computed from Equation(99). Let $k_i(t)$ be the value of k_i used for the previous time interval, k' be the new random value chosen, and $k_i(t + \Delta t)$ be the value of k_i for the next time interval. With these definitions the value of $k_i(t + \Delta t)$ is given by k' if both adjacent segments are laminar; that is, no cross-

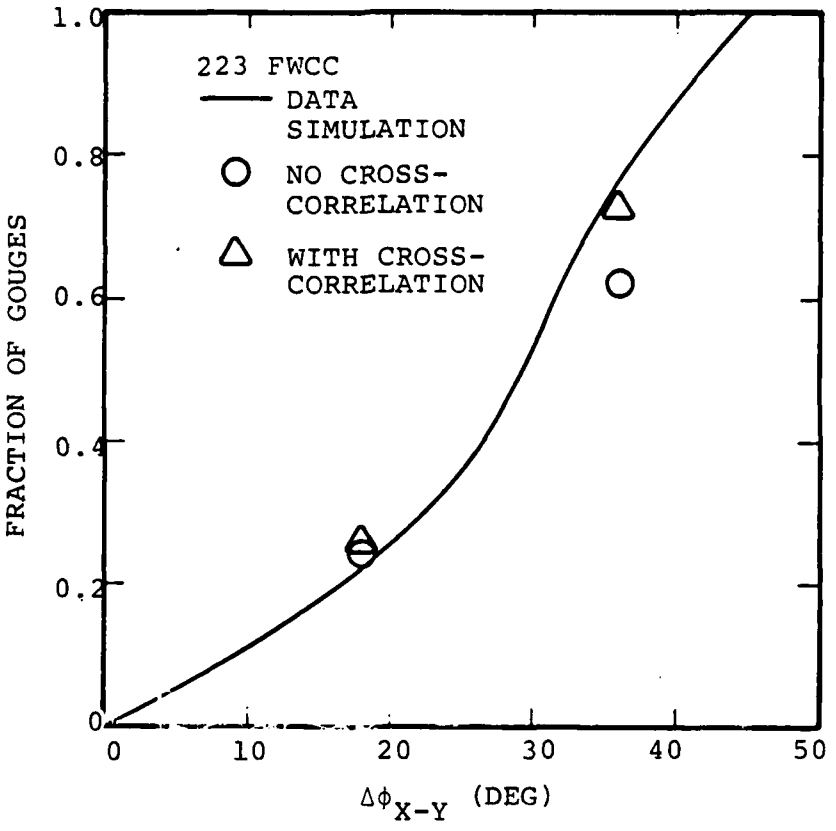

Figure 30. Transition Locations for First Ten Gouges

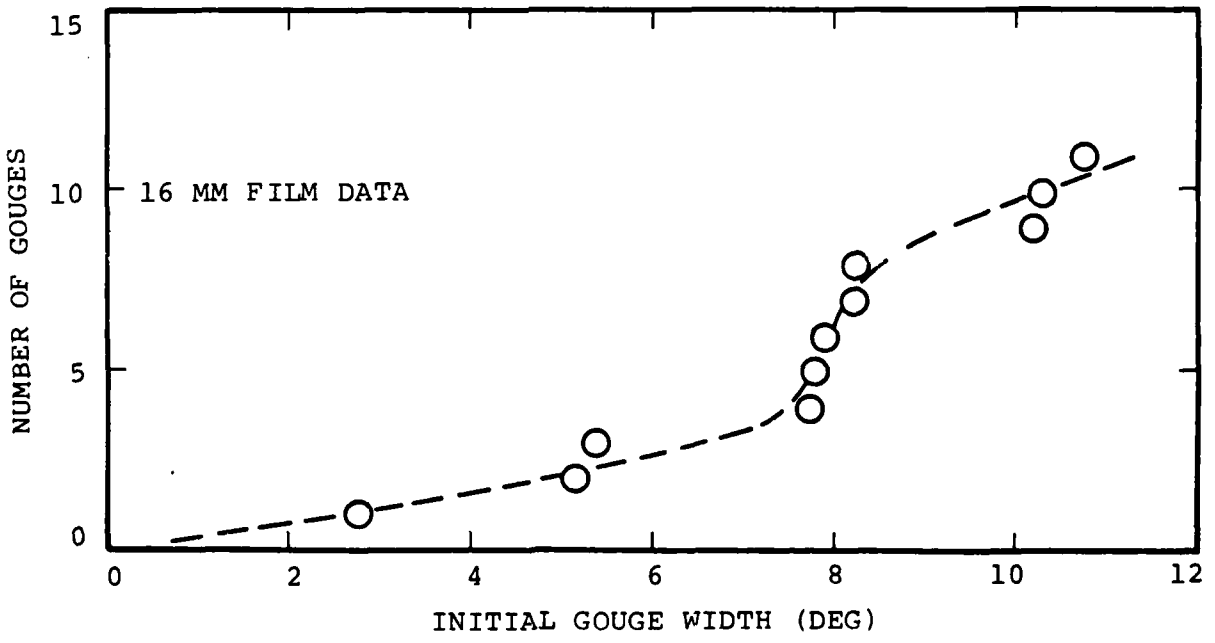

Figure 31. Initial Gouge Width Distribution

correlation is assumed to extend over the adjacent laminar segments. If one of the adjacent segments is turbulent then $k_i(t + \Delta t)$ is increased

$$k_i(t + \Delta t) = 0.5[\bar{k}_j + \max\{k', k_i(t)\}] \qquad (102)$$

where $\bar{k}_j$ is the nosetip average laminar roughness. If both adjacent segments are turbulent the segment's roughness height value is set equal to $\bar{k}_j$. This approach provides for limited cross-correlation effects and improves the correspondence between measured and simulated transition locations as seen in Figure 30.

2.3.2 Turbulent Gouge Measurements

As part of the data measurement effort used to define preferential transition location, both movie and post-test ablation model drawings were used in an attempt to define initial turbulent gouge angular width and growth rate. Movie film data from the south camera of the 50MW facility was analyzed at the first appearance of a visually definable gouge. The film speed was approximately 350 frames/sec and the resolution of the movies was such as to render observation of the details of gouge formation and growth difficult at best. The data obtained for initial gouge width as defined primarily by brightness variations is shown in Figure 31. The average measured value is about 8-deg although measurements ranging from 3 to 11-deg were obtained. Figure 32 shows data from post-test drawings of three models for the angular gouge width plotted versus the gouge shoulder radial location, r_2. The mean of the gouge widths measured is about 17-deg and there appears to be a trend of increasing gouge width with decreasing shoulder radius. No gouges were seen with widths below 8-deg indicating that the much smaller widths measured from the movie films may be indicative of initial turbulent vortex

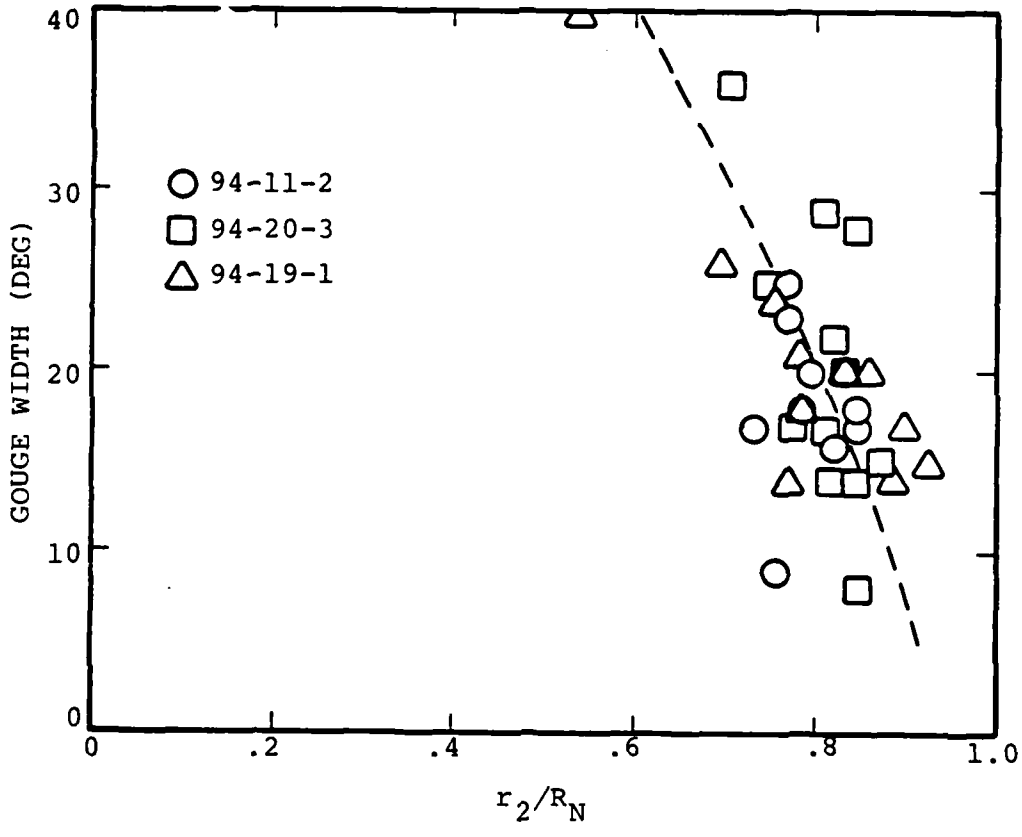

Figure 32. Gouge Width Data from Post-Test Drawings

formation prior to significant ablation and gouge formation. Based on the post-test model measurements the choice of 18-deg for initial gouge width appears reasonable.

An estimate of the angular growth rate of turbulent gouges was obtained from the 16 mm movie film for four 50MW ramp test models where a single gouge was visible. The data obtained is shown in Figure 33 where gouge width is plotted versus total stagnation point recession of each model. Analysis of this data using the models' turbulent recession rates calculated from shape change profiles and the axial drive rates indicates that the equation

$$\frac{d\Delta\phi}{dt} = 1.16\ \dot{s}_T/R_N \qquad (103)$$

adequately represents the data. This equation has the same form as Equation(68) used in the present model, although the growth rate predicted by Equation(68) is about 40 percent lower than the measured data. The post-test drawing data shown in Figure 32, however, indicates that gouge growth rate is probably lower than that given by Equation(103) because few large gouges are observed. Since the film data may reflect heat transfer rate increases rather that actual shape change due to ablation the lower value is used in the present model.

2.3.3 Material Parameters

Additional material related properties included in the nosetip shape change modeling are the equivalent sand roughness (k_s) and bulk density (ρ_o) of the nosetip material. Both laminar and turbulent recession rates vary inversely as bulk density. Turbulent recession rate is assumed to vary as the two-tenths power of k_s.

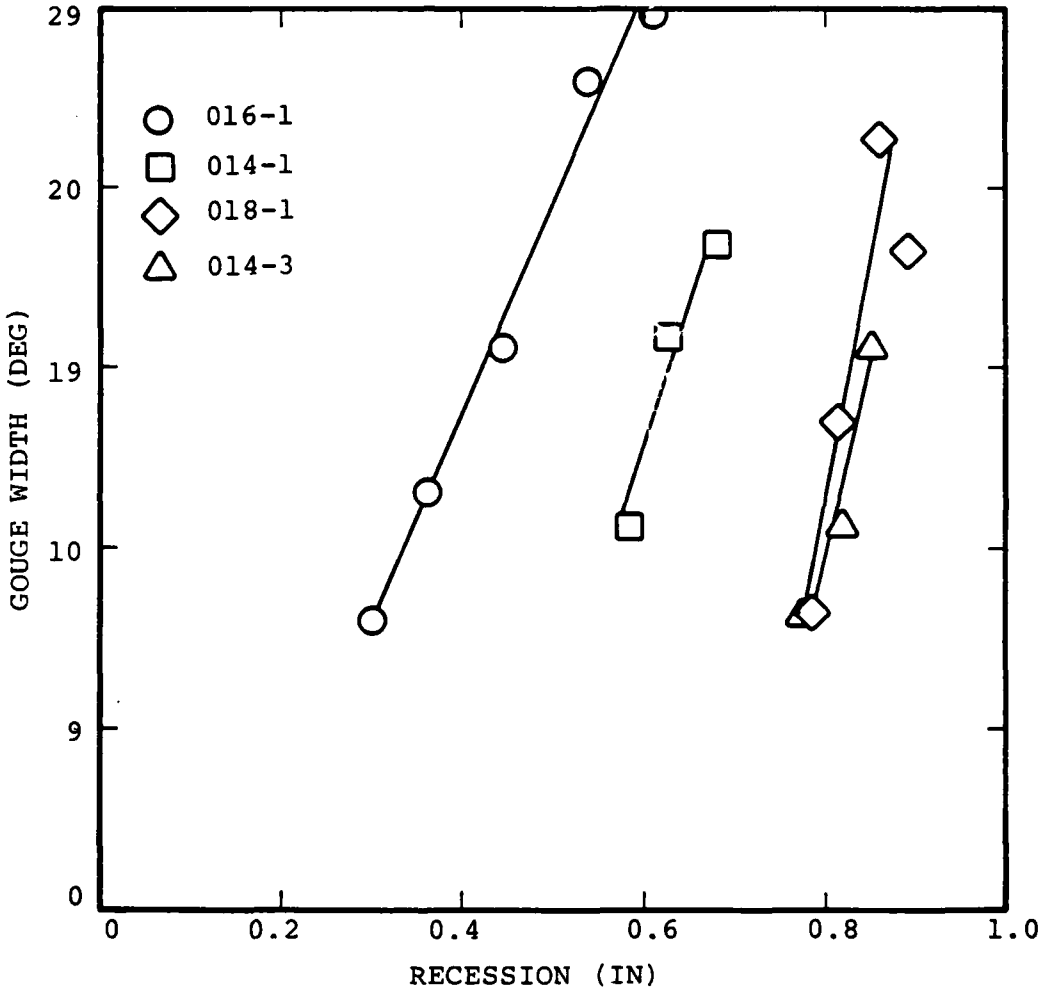

Figure 33. Gouge Width Growth

SECTION 3

RESULTS AND CONCLUSIONS

This section presents comparisons of the results predicted by the analysis method with selected experimental flight test results. Nosetip shape change results are included in addition to limited comparisons of vehicle angle-of-attack history and windward meridian movement. The results of parametric studies conducted in order to identify the effects of reentry trajectory, nosetip material laminar roughness and billet-to-billet variability on nosetip asymmetric shape change are also presented.

Coupling of the nosetip shape change analysis methodology with nosetip pressure/vehicle aerodynamics computer routines (see Vols. II and II of this report, References 27 and 28) and a six-degree-of-freedom trajectory analysis code has been accomplished and is described in Reference 29. The aerodynamics routine contains a detailed procedure for computing reentry vehicle nosetip and frusta pressure distributions including the effects of asymmetric nosetip shapes on downstream frusta pressures and angle-of-attack. The combined analysis for nosetip shape change, vehicle aerodynamics and vehicle dynamics provides an efficient tool for computing ballistic reentry vehicle dispersion. However, for the present purpose of verifying the shape change modeling and providing insight into key parameters affecting asymmetric nosetip shaping, dispersion calculations are not required and a simplier calculation procedure may be employed for determining vehicle aerodynamics.

The approach taken is similar to that described in Reference 30. The nosetip normal force coefficient C_{Nn} defined by

$$C_{Nn} = F_n/q_\infty \pi R_N^2 \tag{104}$$

is calculated by a vector summation of the normal force increment

due to each of the 20 nosetip segments

$$C_{Nn} = \sum_{i=1}^{20} \Delta C_{Nni} \qquad (105)$$

The segment normal force increment, ΔC_{Nni}, is obtained via correlations of the normal force calculated by integration of the surface pressures predicted using the method of Reference 28 as a function of the nosetip segment shape parameters R_1, r_2', R_2, r_3', and r_4'. The effect of angle-of-attack on nosetip normal force is accounted for approximately by correcting C_{Nn} for the effective angle-of-attack (relative to the nosetip cant axis) using the angle-of attack computed for the previous time point. The current vehicle angle-of-attack is then calculated using a first-order moment balance in the pitch plane (ϕ_W) defined by the C_{Nn} vector; i.e.,

$$\alpha_T = \frac{f_v C_{Nn}}{-C_{M\alpha}} \frac{X_{cg}}{L_v} \left(\frac{R_N}{R_B}\right)^2 \qquad (106)$$

where $C_{M\alpha}$ is the derivative of the unablated symmetric vehicle pitching moment about the center of gravity at zero angle-of-attack. The factor f_v accounts for the effect of asymmetric nose shapes on frusta pressure distribution and a resultant change in the vehicle $C_{M\alpha}$. In general, f_v is greater than one for vehicles having bluntness ratios greater than about 15 percent and may be less than one for more slender vehicles (see Reference 31). $C_{M\alpha}$ values used in Equation (106) have been obtained from Reference 32.

The above procedure is sufficient for the investigation of asymmetric nosetip shape development and its effect on vehicle trim angle-of-attack and windward meridian behavior. It should be noted that the nosetip contribution to the vehicle roll torque is also obtained in principle from the nosetip normal force vector and its offset from the vehicle centerline. This contribution to total roll coefficient was investigated in Reference 30 and found to have a low value relative to total vehicle roll torque co-

efficients deduced from flight test data. However, the calculated values matched wind tunnel test data taken on the scale NRV asymmetric nosetip model. Additional investigation of nosetip induced roll torque has been completed in the present study (see Reference 29) including the calculation of roll torques introduced due to imbalanced pressure forces on the "sides" and lands of nosetip turbulent gouges. These calculations which employed a detailed model for nosetip pressure distribution have also indicated that the direct nosetip contribution to vehicle roll torque is small. However, the offset of vehicle normal force from the vehicle center-of-gravity due either to center-of-gravity offset from the vehicle centerline or offset of the frusta aerodynamic center-of-pressure from the center-of-gravity due to manufacturing tolerances and/or asymmetric frusta ablation, etc. is a significant contributor to vehicle roll torque. For typical production manufacturing tolerances, this effect dominates the vehicle roll behavior which is further discussed in Reference 29.

Also not included in this approach is the effect of vehicle lateral motion dynamics or transient response time. That is, Equation 106 assumes instantaneous vehicle response to lateral force perturbations and vehicle lateral motion dynamic frequency is neglected. This approach is sufficient for validation of asymmetric shape change modeling and assessment of general windward meridian behavior characteristics. However, for complete description of the vehicle angle-of-attack and windward meridian behavior and the resulting vehicle dispersion, the asymmetric shape change model must be coupled to vehicle dynamics as described in Reference 29.

3.1 MODEL VALIDATION

Comparisons of the results predicted by the statistical nosetip shape change model coupled with the approximate vehicle aerodynamics methodology described above are presented in this section for selected flight test vehicles.

Nosetip Recovery Vehicle (NRV) - The NRV vehicle flight test provides an excellent test case for validation of nosetip shape change analysis

methods since the vehicle nosetip was recovered (see Figure 1) after the flight. Flight test trajectory and vehicle characteristics are given in Table 3. The roughness values chosen are derived from post-test ablation model roughness measurements and analyses of ground test data and a single flight test (RVTO-3B-102).

Table 3
NRV FLIGHT TEST PARAMETERS

V_∞ @ 279.5 kft (fps)	18731.
α_∞ @ 279.5 kft (deg)	-25.46
R_N (in)	1.25
R_B (in)	5.96
Θ_f (deg)	6.0
R_N/R_B	0.2097
Nosetip Material	ATJ-S Graphite
k_L (mil)	0.68
σ_k	0.153
k_s (mil)	1.64
f_v	1.0

The NRV vehicle was designed to drop weight at approximately 28,000 feet altitude and rapidly decelerate with final descent by parachute for recovery. The nosetip of the vehicle was recovered intact and provides an exact definition of nosetip shape at an altitude somewhat lower than 28 kft since some slight shape change is predicted to occur during the initial deceleration period. Figure 34 shows the post-flight recovered shape exhibited by the nosetip. Stagnation point recession was approximately 0.35 inches and a mildly indented shape developed. Turbulent recession was evident on all meridians forming a laminar cap region. The geometric center of this cap was offset approximately 0.1 inch from the nosetip center-

line along the 40-deg meridian (see Figure 1). During entry a preferred windward meridian location developed below 38 kft and was located at 200 to 220-deg or about 180-deg from the laminar region offset as would be expected.

In order to compare the analysis with the flight test results, twenty Monte Carlo trials were computed for the flight test and material parameters specified in Table 3. Each of these trials yields a complete reentry shape change history, vehicle angle-of-attack history and windward meridian history. For these results twenty trials are sufficient to identify mean and standard deviations of the various parameters of interest because the shape change process is fairly well behaved statistically and is not bimodal. In general, one trial was chosen as a nominal flight based on the correspondence of its angle-of-attack at impact (28,000 feet altitude for NRV) to the mean value for the twenty trials and the similarity of its angle-of-attack history to that typical of the twenty trials. Also, in order to indicate the variability of the results calculated, two specific additional trials were selected to represent the range of results obtained. These trials were selected from the set of twenty trials on the basis of calculated angle-of-attack at impact (or in the case of the NRV vehicle at the beginning of the recovery sequency). The trial for which the computed impact angle-of-attack is highest is designated as HIGH while that evidencing the lowest value is designated as LOW. Since the frequency of occurrence of each of these trials is one in twenty they correspond approximately to + 2σ and - 2σ values, respectively. The presentation of the calculated results for these three specific trails rather than statistically averaged (at a given altitude) quantities better reflects the actual time history likely to be observed on a specific flight test and will be used in the remainder of this section.

Figure 35 presents the windward-leeward nosetip shape calculated for the nominal trial. Stagnation point recession is 0.32 inches which compares well with that of the recovered nosetip. Comparison of Figures 34 and 35 indicate that the approximate

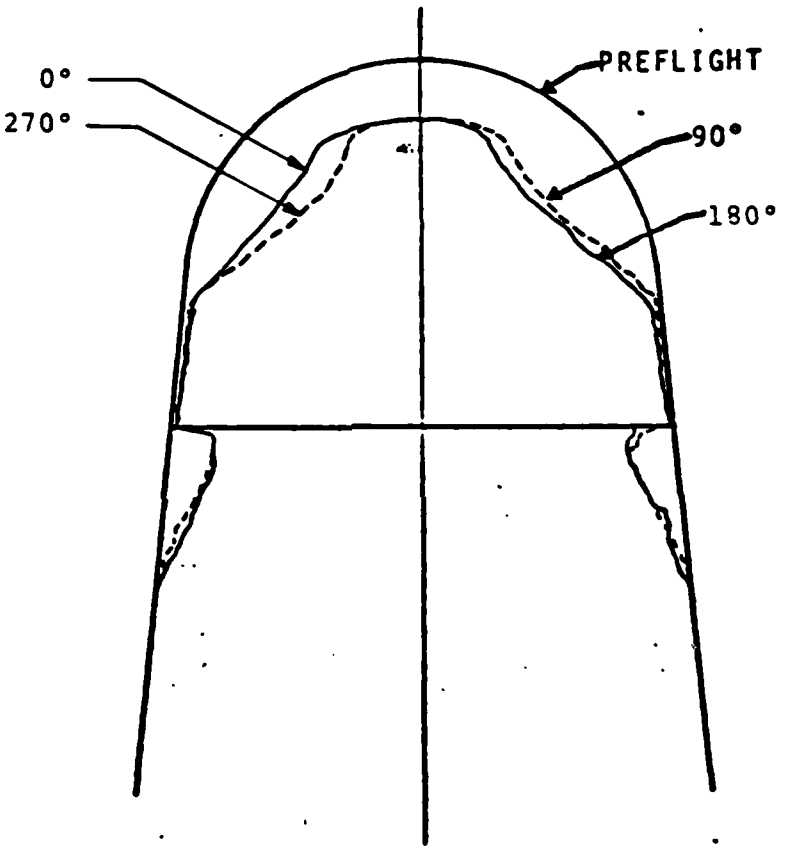

Figure 34. NRV Nosetip Recession

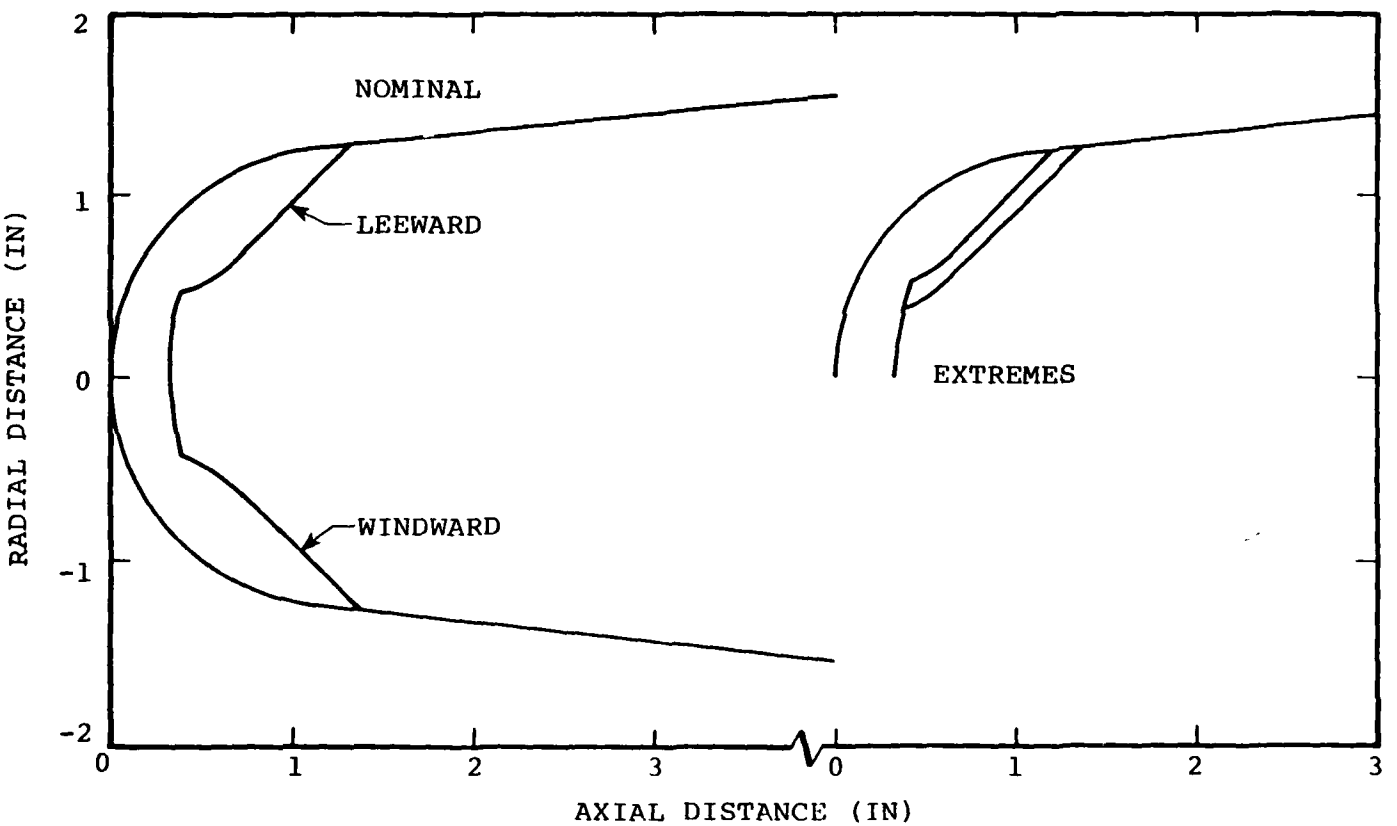

Figure 35. Computed NRV Shape Change

shape change modeling gives a good representation of the windward and leeward rays including the radial extent of the laminar region. Also shown in Figure 35 are the maximum and minimum recession turbulent ray shapes predicted. All nosetip ray shapes fall within the envelope of these two rays with the rays evidencing transition nearest the vehicle centerline located near the windward meridian. All nosetip rays are predicted to be turbulent which is consistent with the recovered nosetip shape. First ray transition occurs at an altitude of about 47.5 kft, the mean transition altitude is 40 kft, and all rays experience transition by an altitude of 34 kft.

Comparison of flight measured angle-of-attack history and the results of the present analysis are shown in Figure 36. Flight test data shows a rapid buildup in α_T beginning at 37 kft, reaching a final value of 1.25-deg at the beginning of the recovery sequence. The present analysis shows the same trend with altitude. The mean trim angle at 28.0 kft altitude is 1.18-deg. The highest and lowest trims predicted at this altitude are 1.80 and 0.58 degrees, respectively. Because of the relatively small amount of nosetip recession incurred at this altitude, a value of f_v equal to one was used for these calculations even though the vehicle bluntness ratio would dictate a somewhat larger value. Larger values of f_v would yield correspondingly larger values of predicted trims.

Reentry Vehicle 2 (RV2) - The RV2 flight test vehicle nosetip was instrumented to measure nosetip recession on eleven axial rays using irradiated TOWS and CdTe sensors. Data reduction was complicated by the effects of redeposition of radioactive material; however, an attempt was made by the vehicle contractor to analytically compensate for this effect. Table 4 presents pertinent vehicle and trajectory parameters.

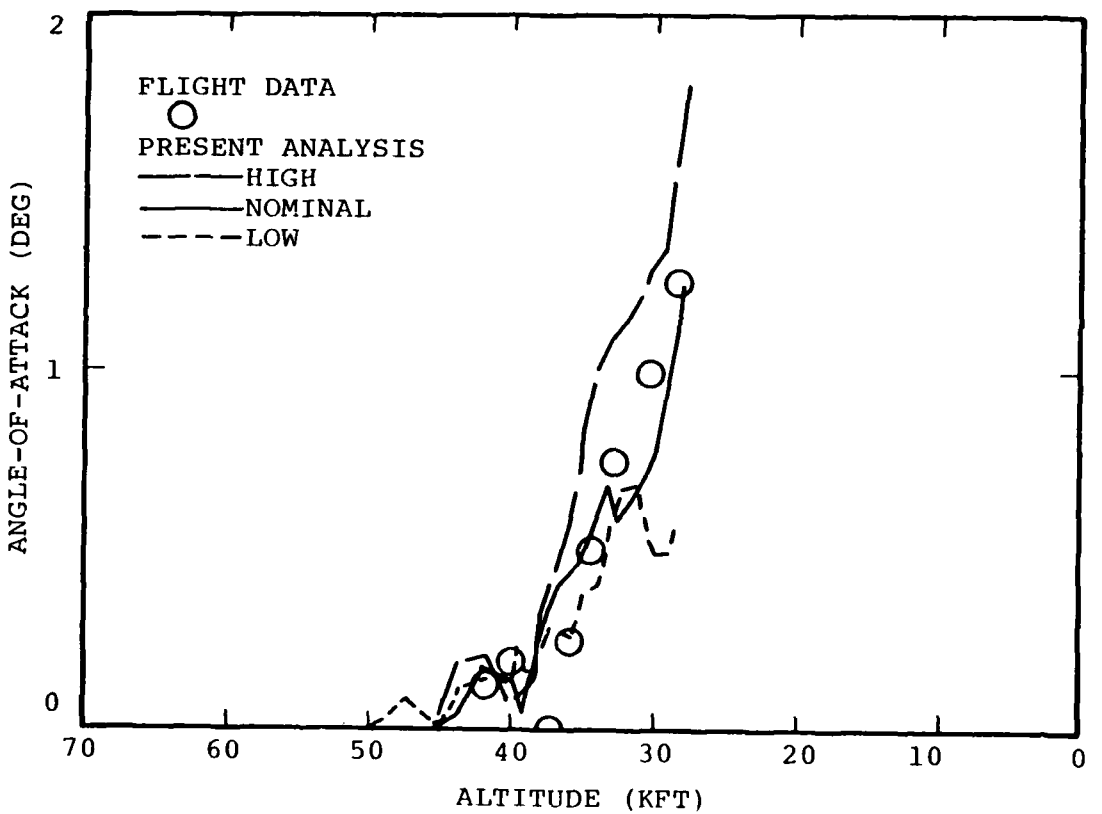

Figure 36. NRV Angle-of-Attack Comparison

AD-A109 945 SCIENCE APPLICATIONS INC IRVINE CA MATERIAL SCIENCES--ETC F/G 16/3
PERFORMANCE TECHNOLOGY PROGRAM (PTP-S II). VOLUME VI. A STATIST--ETC(U)
AUG 80 R B DIRLING F04701-77-C-0126
UNCLASSIFIED SAI-061-81-05-06 BMO-TR-80-53 NL

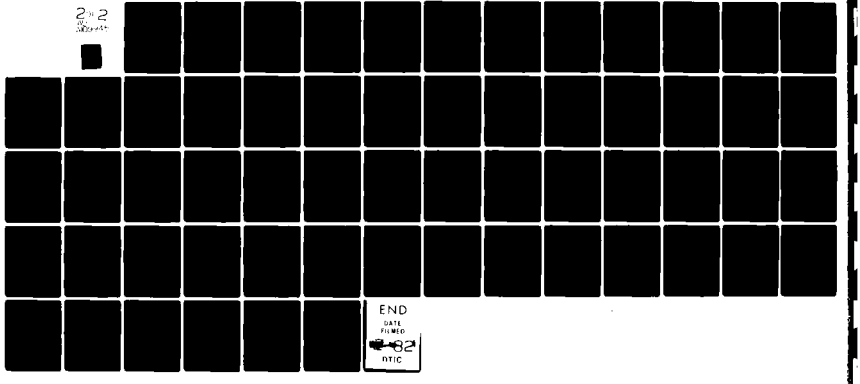

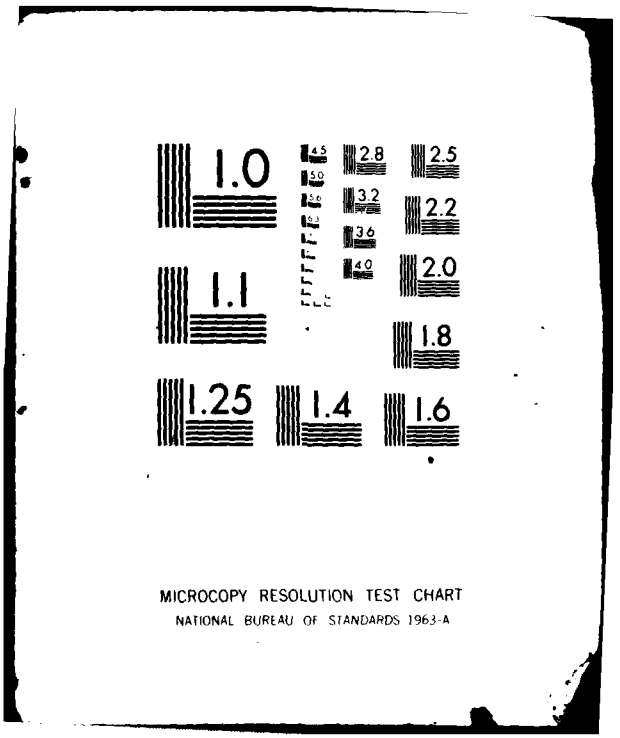
1.0
1.1
1.25
1.4
1.6
1.8
2.0
2.2
2.5
2.8
3.2
3.6
4.0
4.5
5.0
MICROCOPY RESOLUTION TEST CHART
NATIONAL BUREAU OF STANDARDS 1963-A

Table 4

RV2 FLIGHT TEST PARAMETERS

V_∞ @ 400 kft (fps)	22185.
α_∞ @ 400 kft (deg)	-29.92
R_N (in)	2.0
R_B (in)	12.0
θ_f (deg)	7.4
R_N/R_B	0.1667
Nosetip Material	223/PAN FWCC
k_L (mil)	0.40
σ_k	0.325
k_s (mil)	4.2
f_v	1.3

Results for the RV 2 flight test are shown in Figures 37 through 42. Figure 37 presents the reduced recession data (compensated for redeposition effects) at vehicle impact. As shown, the data from the 0, 180, and 270-deg rays are nearly identical. The 90-deg ray data indicates an increased laminar shoulder radial location relative to the vehicle centerline. A possible nosetip shape drawn through the data points is also shown. This shape is consistent with the nosetip drag coefficient measured at impact and indicates an indented nosetip similar to the NRV recovered nosetip with a laminar cap offset approximately 0.25 inches from the nosetip centerline. Measured stagnation point recession is 0.47 inches. The flight test data shows that the windward meridian was located at approximately 260-deg, that is, very nearly opposite the 90-deg ray.

Figure 38 presents a comparison of the stagnation point recession history measured for the flight and the results of the present analysis. Nominal predicted stagnation point recession is 0.40 inches, slightly less than the measured value. The highest value predicted was 0.47 inches while the lowest value in the twenty trials was 0.37 inches and corresponded to laminar boundary layer

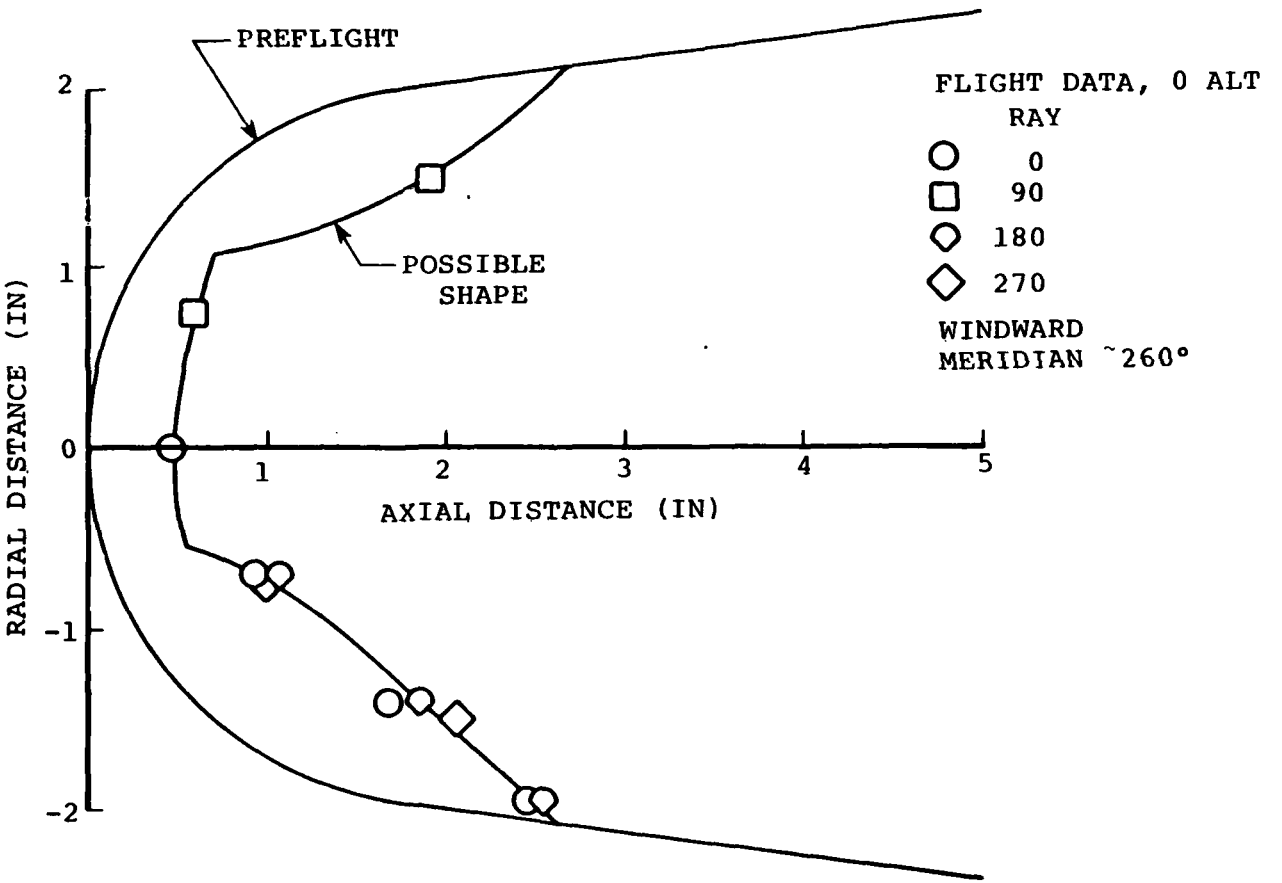

Figure 37. RV2 Nosetip Recession

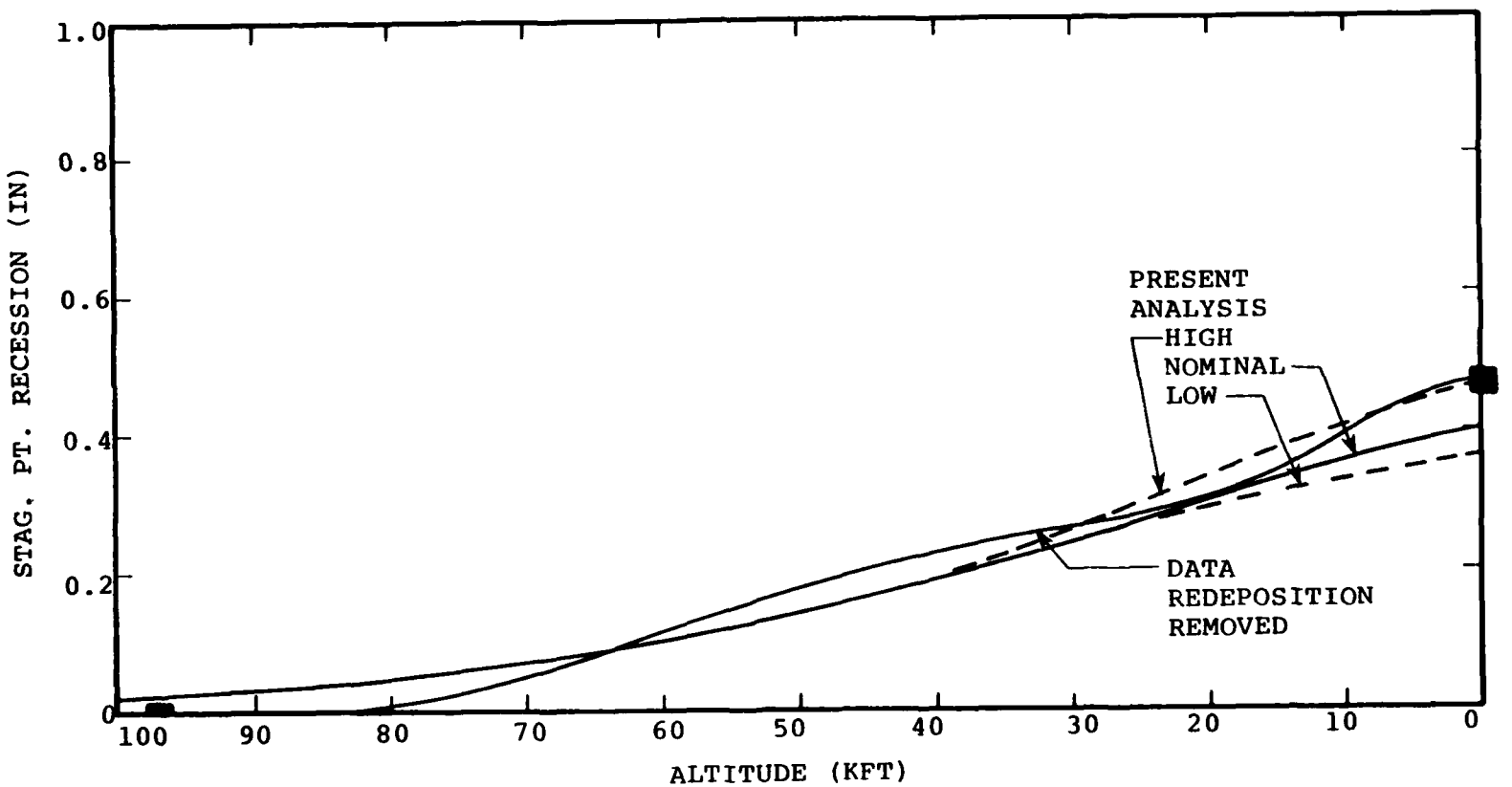

Figure 38. RV2 Recession History Comparison

flow over the nosetip throughout the flight. These results and those presented in Figures 39 through 42 have been obtained including the effect of billet-to-billet variability as discussed in Section 2.3.1. The value of the standard deviation of the average laminar roughness height ($\sigma_{\bar{k}}$ in Eq. 98) is 0.068; the distribution is truncated at a minimum value of 0.19 mils. The all laminar nosetip trial referred to above occurred for a value of k_L close to this minimum value.

Figure 39 presents the nosetip shape at impact calculated for the nominal flight trial. Comparison of the calculated shape and the data of Figure 37 indicates that the general features of the predicted asymmetric shape are similar to those derived from the flight test data. The radial extent of the laminar is somewhat underpredicted; however, the degree of offset and the depth of turbulent recession where the nosetip turbulent surfaces intersect the conical frusta is well predicted by the analysis method.

Table 5 presents predicted results relative to the occurrence of boundary layer transition on the nosetip including

Table 5

RV2 NOSETIP TRANSITION PREDICTIONS

Event	Altitude, Mean/1 (KFT)	
	Billet-to-Billet Variability	Billet-to-Billet Variability
1st Gouge Onset	48.3/13.3	51.3/2.5
10th Gouge Onset	26.7/19.7	32.3/0.7
NT Transition Completed	23.4/17.4	27.8/2.1

the effect of billet-to-billet variability. For this case, 70 percent of the trials experienced complete nosetip transition to turbulent flow as evidenced by the prediction of transition on all twenty nosetip segments. In one trial (of the twenty trials calculated), the nosetip remained completely laminar to impact while in the remaining trials various numbers of turbulent gouges were predicted to occur around the nosetip periphery. These cases contributed substantially to the relatively large standard deviations shown in Table 5. Mean transition altitude as delineated by occurance of the tenth turbulent gouge was 26.7 kft while the mean altitude of initial

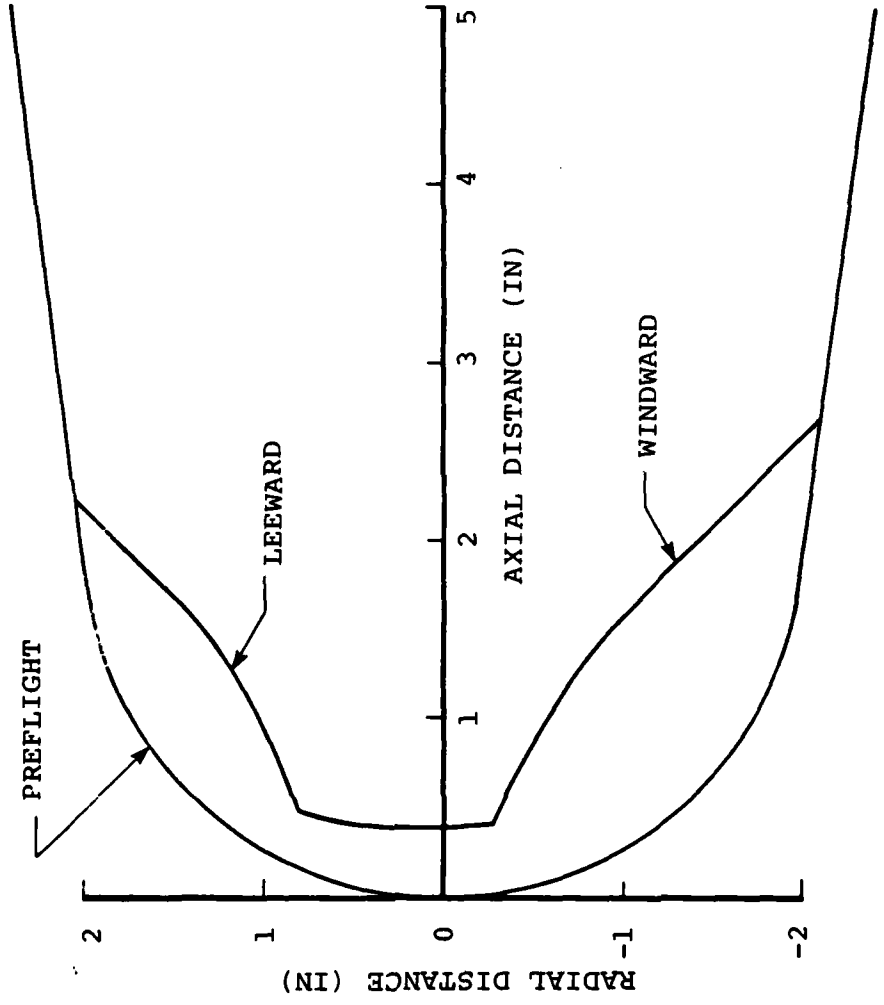

Figure 39. Computed RV2 Shape Change

boundary layer transition is at 48.3 kft. Without billet-to-billet variability, all trials experienced complete nosetip transition which results in the slightly higher mean altitude predicted for the various transition events compared to the case with material variability. The standard deviations for the altitude of the events are substantially reduced indicating that the variation of roughness heights on a particular nosetip has little effect of overall transition performance and vehicle drag coefficient history characteristics. However, control of billet-to-billet variability is an important requirement for accurate BRV's.

Figure 40 shows the measured and predicted angle-of-attack history for RV2. The flight vehicle spun up as altitude decreased to about 65 percent of the critical roll rate. The total (dynamic) angle-of-attack was theoretically deamplified by the vehicle contractor resulting in the trim angle history shown. The trim angle data is between the high and nominal results from the present analysis (which do not include vehicle spin up) although the altitude of trim buildup occurs between that of the nominal and low predicted results. Windward meridian stabilization (see Figure 41) results indicate that the present analysis may be overpredicting the effect of small early gouges on nosetip normal force, and hence trim angle, since predicted stabilization of the windward meridian location is consistent with the flight test data. It should be pointed out that the windward meridian obtained in flight was within 10-deg of an instrumented ray having a sonic point recession sensor. This close correspondence of the windward meridian with a nosetip ray having a sonic point recession TOW has been noted for other flight test vehicles and may indicate that the sonic point TOW's cause preferential boundary layer transition. This effect, if present, may contribute to higher values of trim angle-of-attack due to somewhat premature and/or relatively firm fixing of the windward meridian.

RV3 and RV4 - RV3 and RV4 provide a direct comparison of the effect of vehicle bluntness ratio on nosetip ablation and shape change and vehicle aerodynamic performance. As seen in Table 6, all para-

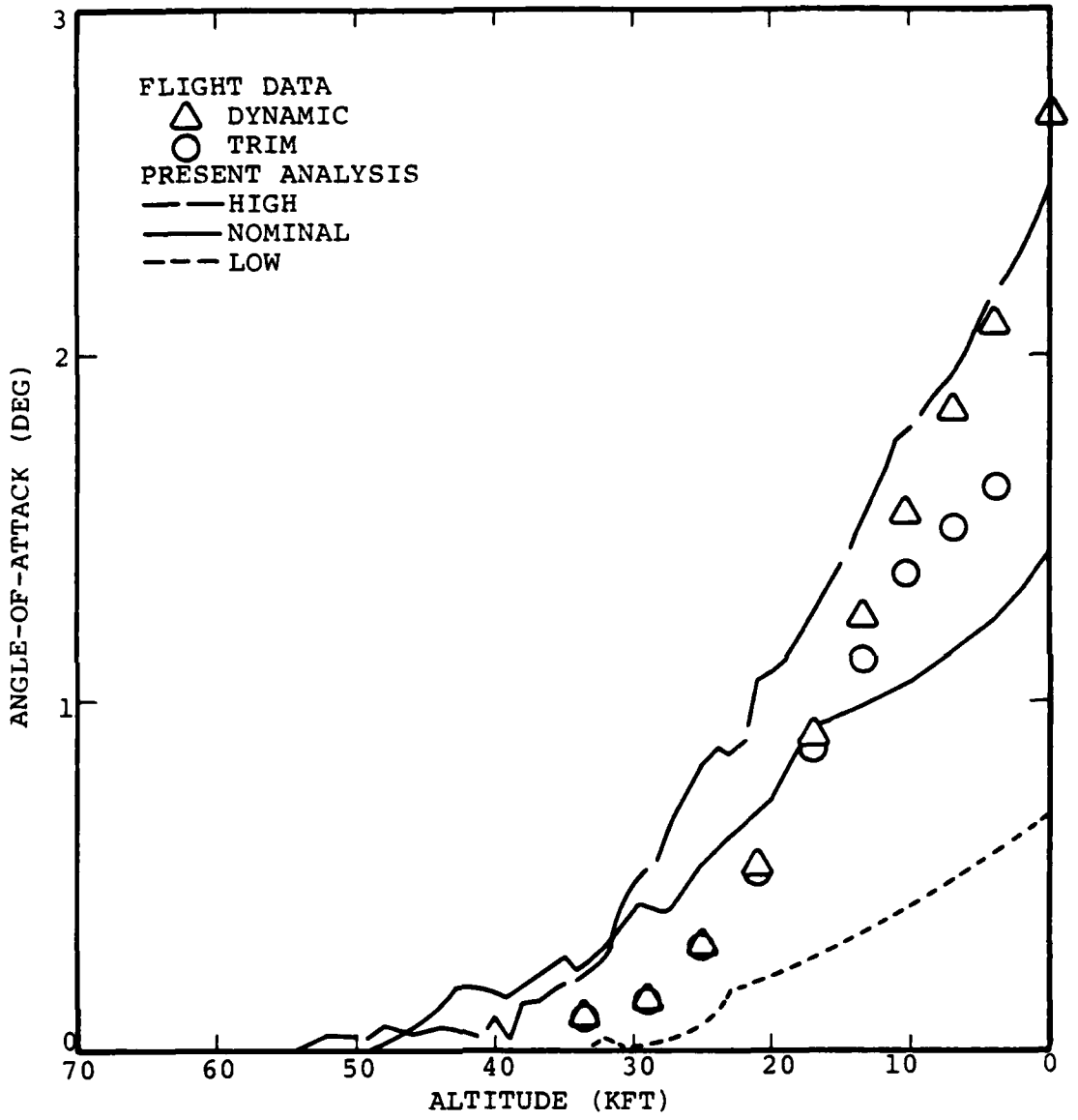

FIGURE 40. RV2 Angle - of Attack Comparison

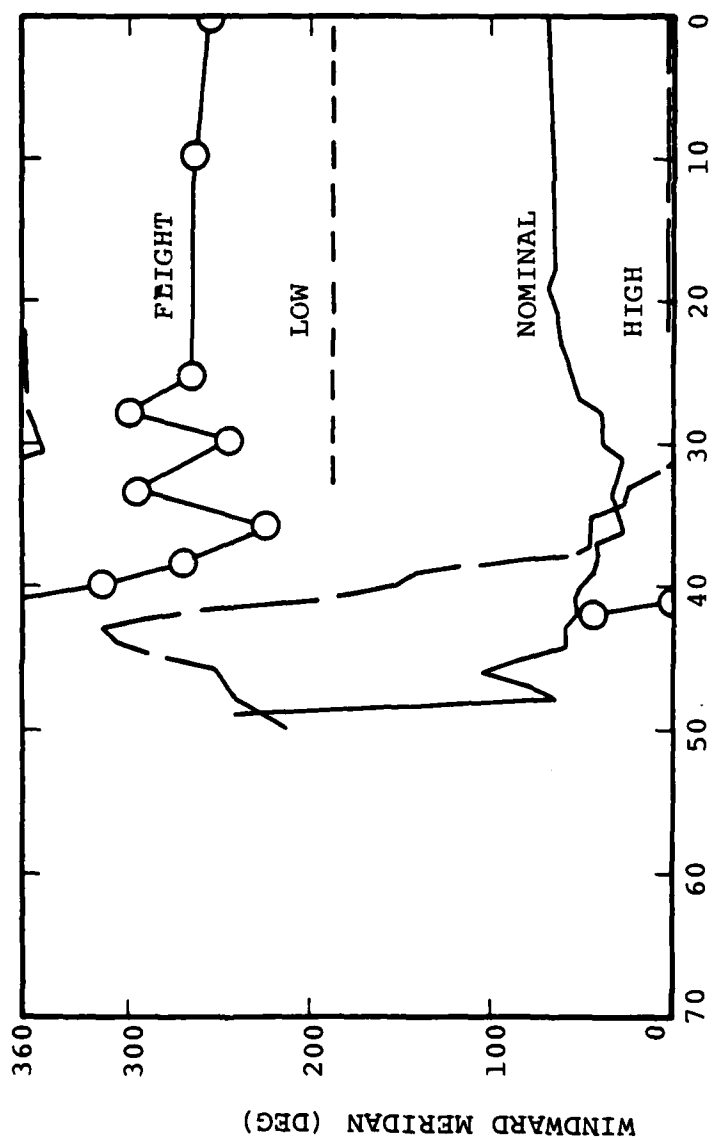

Figure 41. RV2 Windward Meridian Histories

meters for the two vehicles are identical including nosetip material with the exception of vehicle bluntness ratio which ranged from 0.15 for RV3 to 0.25 for RV4. Corresponding values of the frusta amplification factor (f_v) were chosen as 1.0 and 1.5. Both nosetips were instrumented with irradiated Ta TOW's for the in situ recession measurements.

Table 6
FLIGHT TEST PARAMETERS FOR RV3 AND RV4

	RV3	RV4
V_∞ @ 400 kft (fps)	22325	22325
γ_∞ @ 400 kft (deg)	30.1	30.1
R_N (in)	0.75	1.25
R_B (in)	5.0	5.0
θ_f (deg)	6.0	6.0
R_N/R_B	0.15	0.25
Nosetip Material	223/T-50 FWCC	223/T-50 FWCC
k_L (mil)	0.613	0.613
σ_k	0.37	0.37
k_s (mil)	1.74	1.74
f_v	1.0	1.5

Figures 42 and 43 compare the measured stagnation point recession histories with the corresponding analysis results including the effect of billet-to-billet variability. For the 223/T-50 FWCC

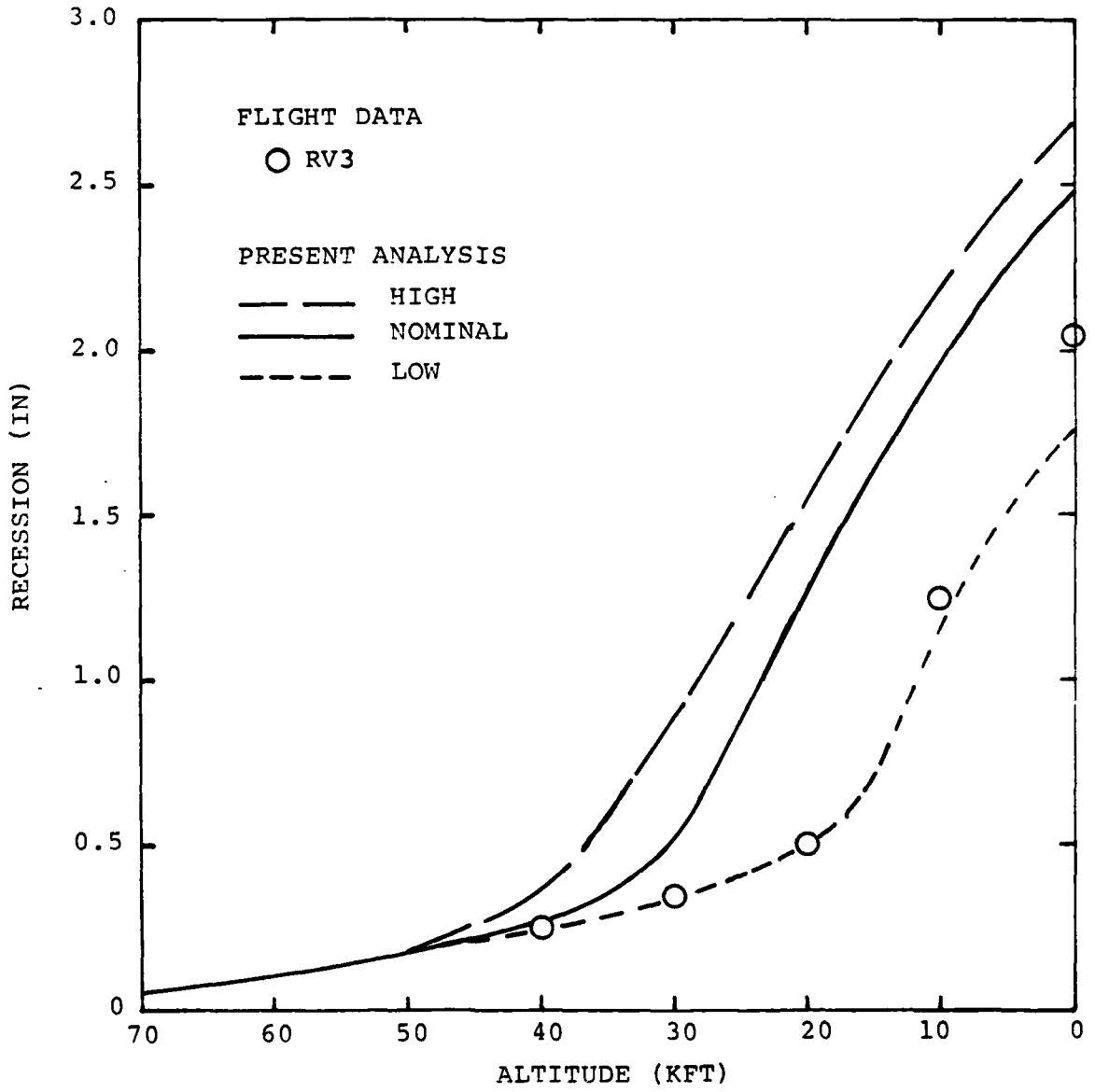

Figure 42. RV3 Nosetip Recession

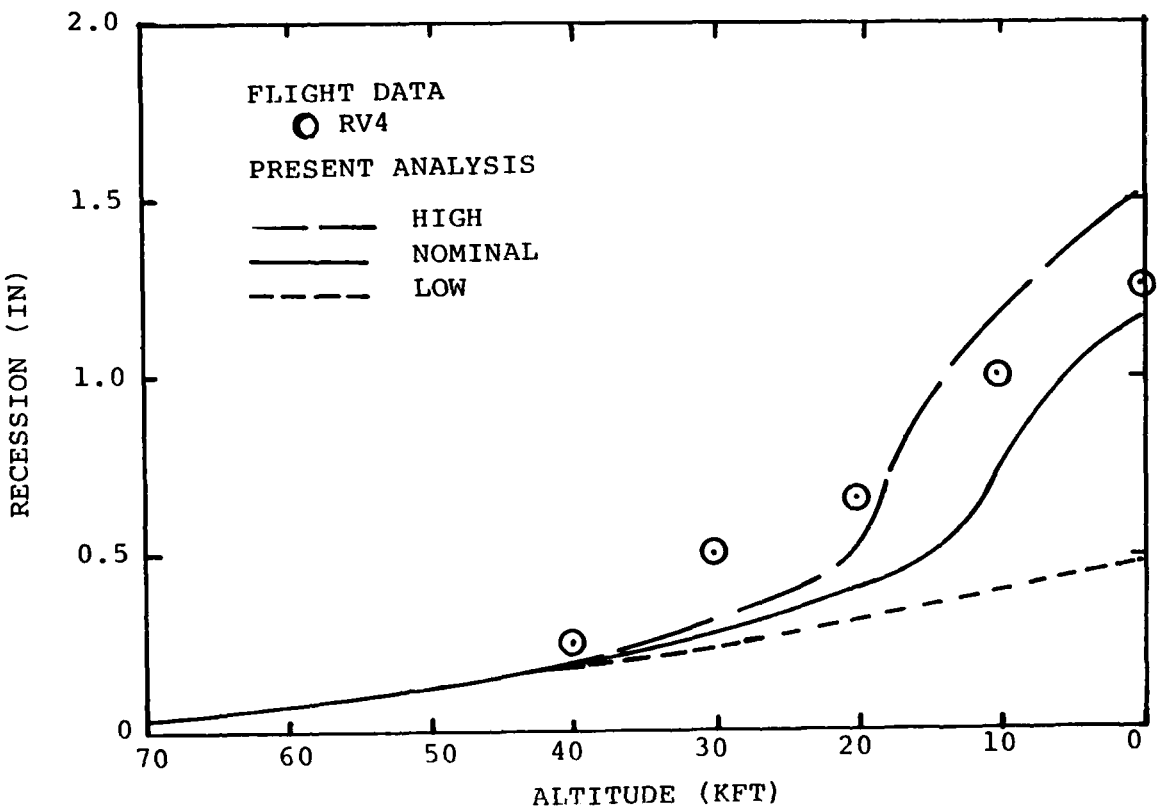

Figure 43. RV4 Nosetip Recession

effect of billet-to-billet variability. For the 223/T-50 FWCC nosetip material flown on these vehicles, the normalized standard deviation of the average laminar roughness height is 0.30 mils. These values are derived from optical measurements of post-test ablation model surface roughness and indicate that while 223 with T-50 fibers yields a somewhat increased average laminar roughness height compared to 223 with PAN fibers, the normalized standard deviation is slightly smaller. The measured recession for both flight cases is within the expected range. For the sharper RV3, the measured recession of 2.05 inches is 18 percent below the calculated nominal result but substantially above the low result of 1.76 inches. For the blunt RV4 vehicle measured recession is 8 percent higher than the calculated nominal result. The large difference in nosetip recession behavior for the two vehicles is evident from these results. Although the mean transition altitude of RV4 is only 0.5 kft below that of the sharper vehicle (49.1 kft compared to 49.6 kft), the onset of rapid stagnation point recession is delayed to lower altitudes by the longer length of time required for nosetip sharpening.

Figure 44 presents the calculated RV3 nosetip shapes at impact for the high, nominal and low trials. The positions of the maximum recession and tangent point TOW measurements indicate a blunter shape than that calculated by the present method. However, the large measured recession rate is inconsistent with the blunt shape indicated by the recession measurements and the off-stagnation point measurements may be compromised by redeposition effects for this small nose radius tip. The calculated shapes indicate a small laminar stagnation region with only a slight recompression region downstream of the laminar region shoulder . The laminar region offset has an average value of 0.089 inches and a standard deviation of 0.029 inches.

For the blunt RV4 vehicle, Figure 45 indicates the influence of billet-to-billet variability on nosetip recession. The calculated values of nosetip recession are shown as a function of the nosetip

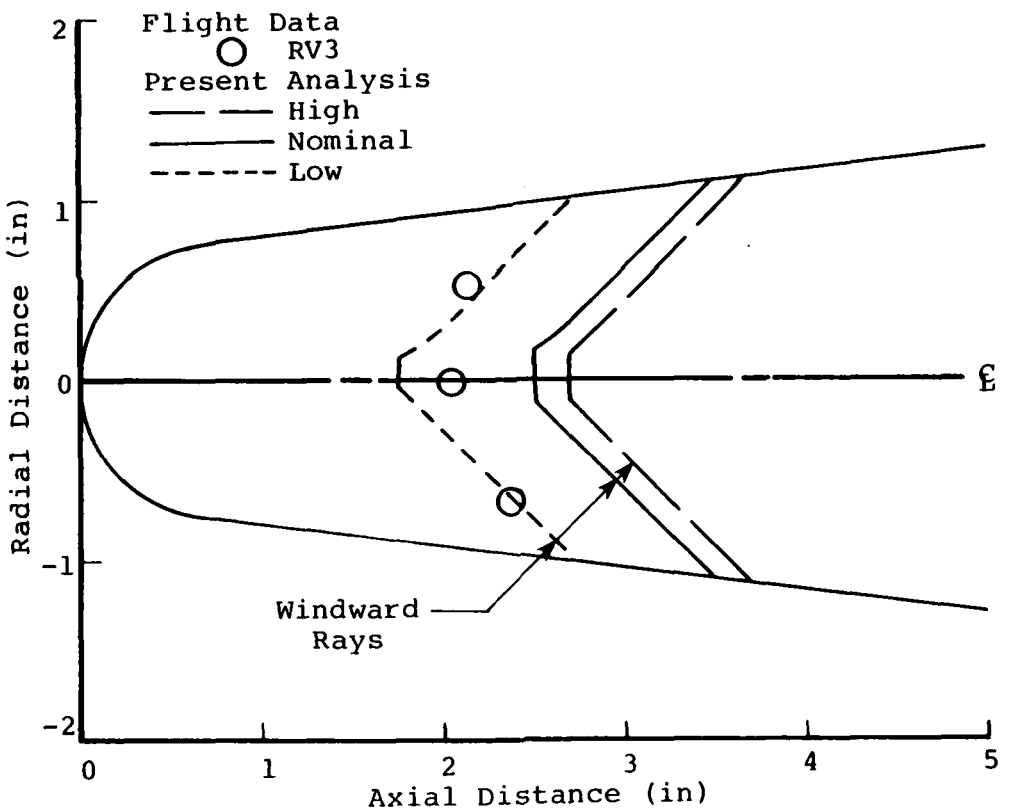

Figure 44. Impact Shape Comparison for RV3

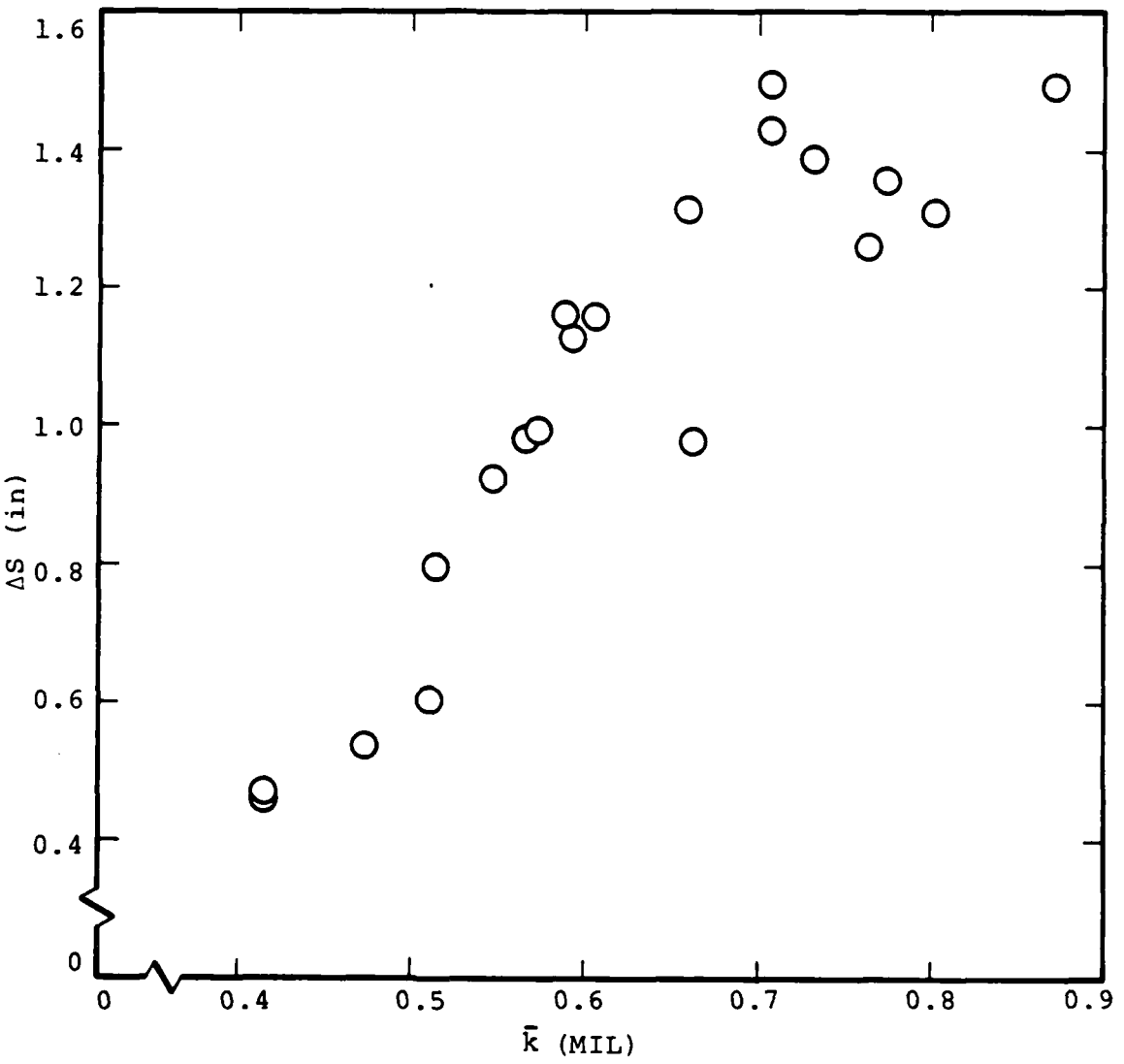

Figure 45. Calculated Sensitivity of Recession to Mean Laminar Roughness Height for RV4

mean laminar roughness assigned for each of the twenty trials computed. The mean roughness heights chosen fall between 0.4 and 0.8 mils and are, as expected, centered about the average billet laminar roughness height, 0.613 mils. These data indicate a fairly direct correspondence between $\bar{k}$ and Δs. The variability of Δs for a given value of $\bar{k}$ (indicated by the vertical spread of the calculated points) reflects the influence of the roughness element height distribution used to assign roughnesses to the twenty nosetip segments for a specific trial. However, billet-to-billet variability is seen to be the predominant influence on nosetip recession variability.

Figures 46 and 47 compare measured vehicle trim angles with the range of trim angle histories calculated using the present method. Twenty trials were computed for each vehicle and the effects of billet-to-billet variability are included. Figure 46 presents the results for the sharp vehicle. Measured trim angles are generally consistent with those predicted although slightly higher. For this vehicle configuration, however, trim angles of less than one degree are expected and observed. For the blunt vehicle much larger trim angles are predicted as seen in Figure 47. The range of predicted trim angles varies from a high of over 10-deg to a low of slightly over one degree. The nominal value of the predicted results is 5.2-deg maximum which compares well with the measured value of 6.3-deg. Both the predicted and the measured trim angle histories indicate that the maximum value of trim angle is developed prior to impact in the 20 to 10 kft altitude range. In the case of the measured data, the subsequent increase below about 8 kft altitude is due to amplification of the static trim angle as the vehicle spin rate approached the critical resonance value.

The effect of billet-to-billet variability on trim angle is illustrated in Figures 48 and 49 for the blunt and sharp vehicles, respectively. These figures present calculated trim angle-of-attack at impact as a function of the mean laminar roughness height assigned to the nosetip material for each of the twenty trials computed. Unlike the results shown in Figure 45 for the effect of billet-to-billet

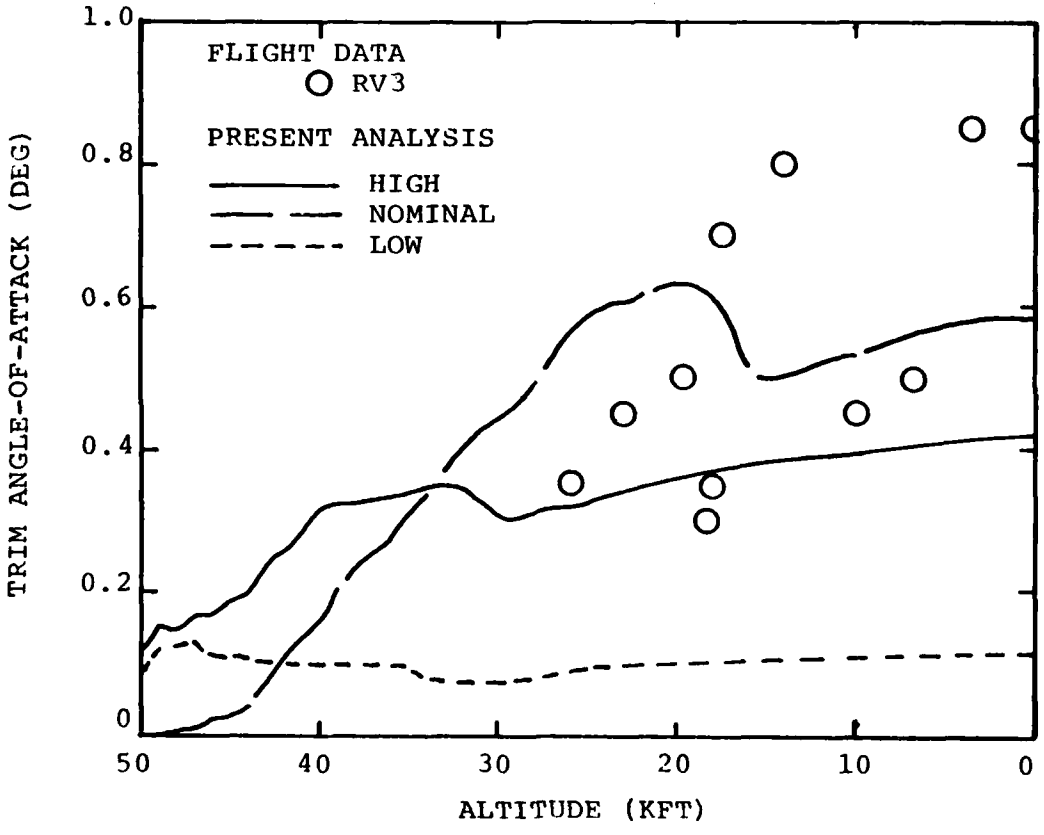

Figure 46. Trim Angle Correlation for RV3

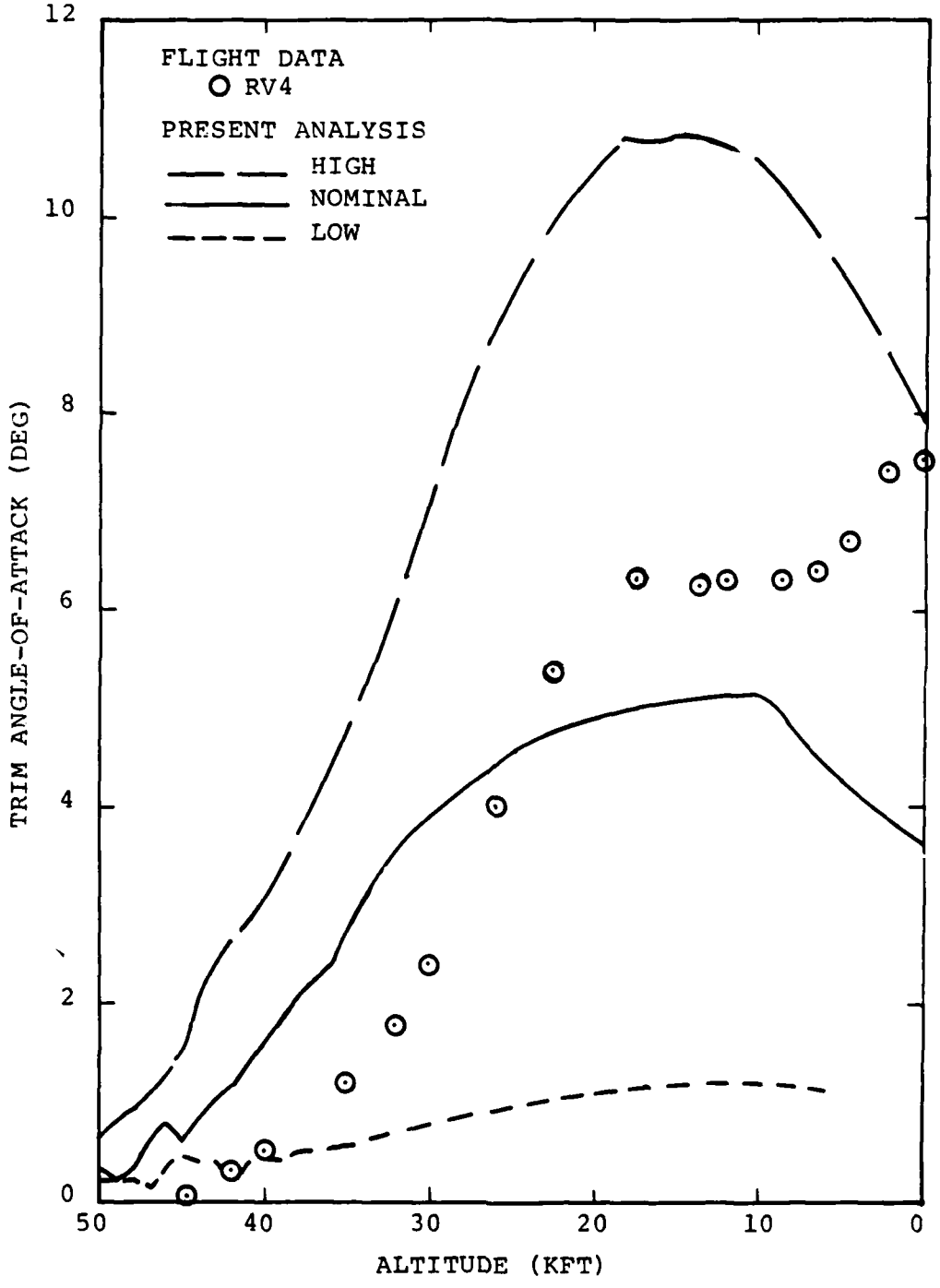

Figure 47. Trim Angle Correlation for RV4

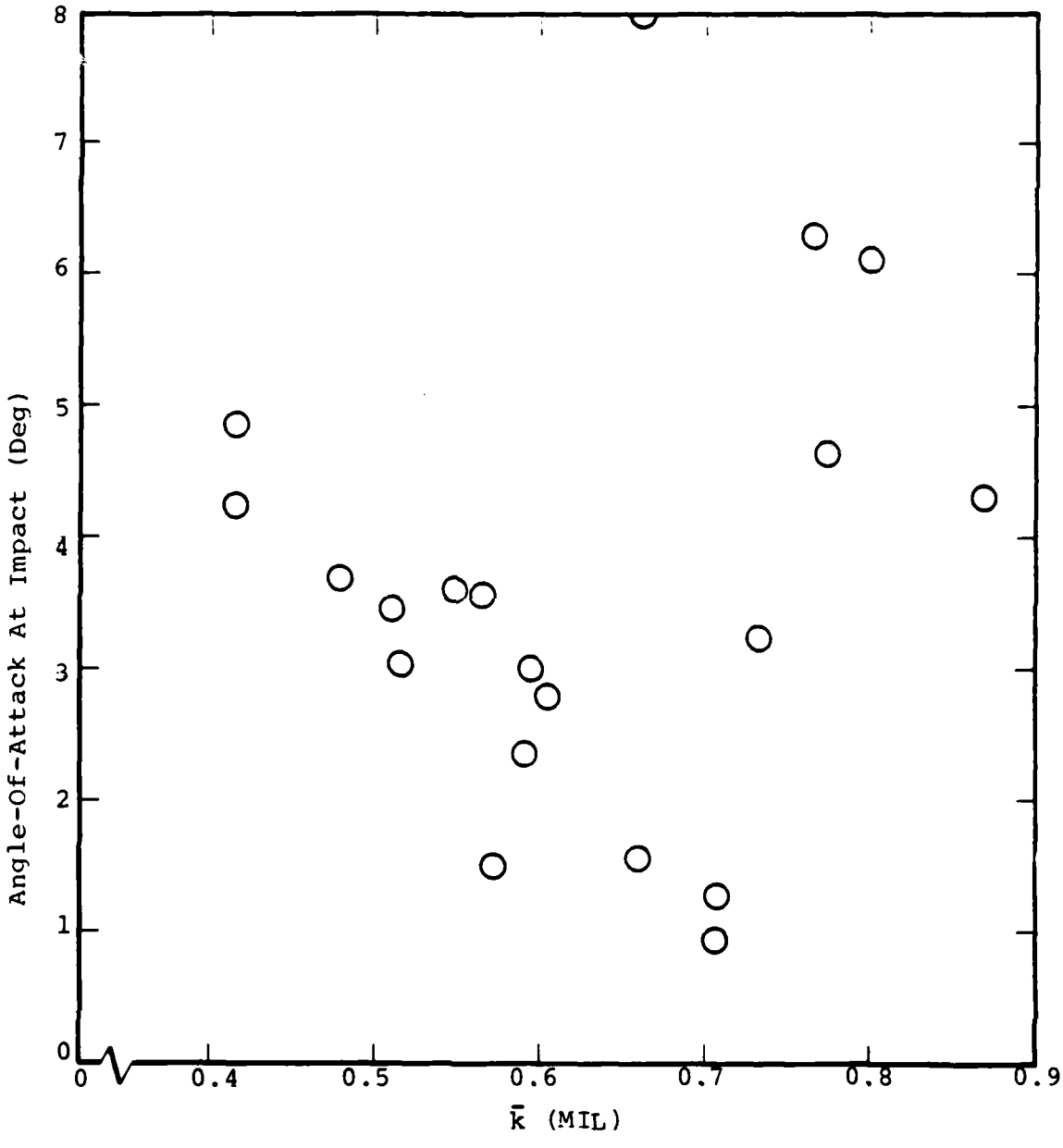

Figure 48. Sensitivity of Impact Trim Angle to Mean Laminar Roughness Height for RV4

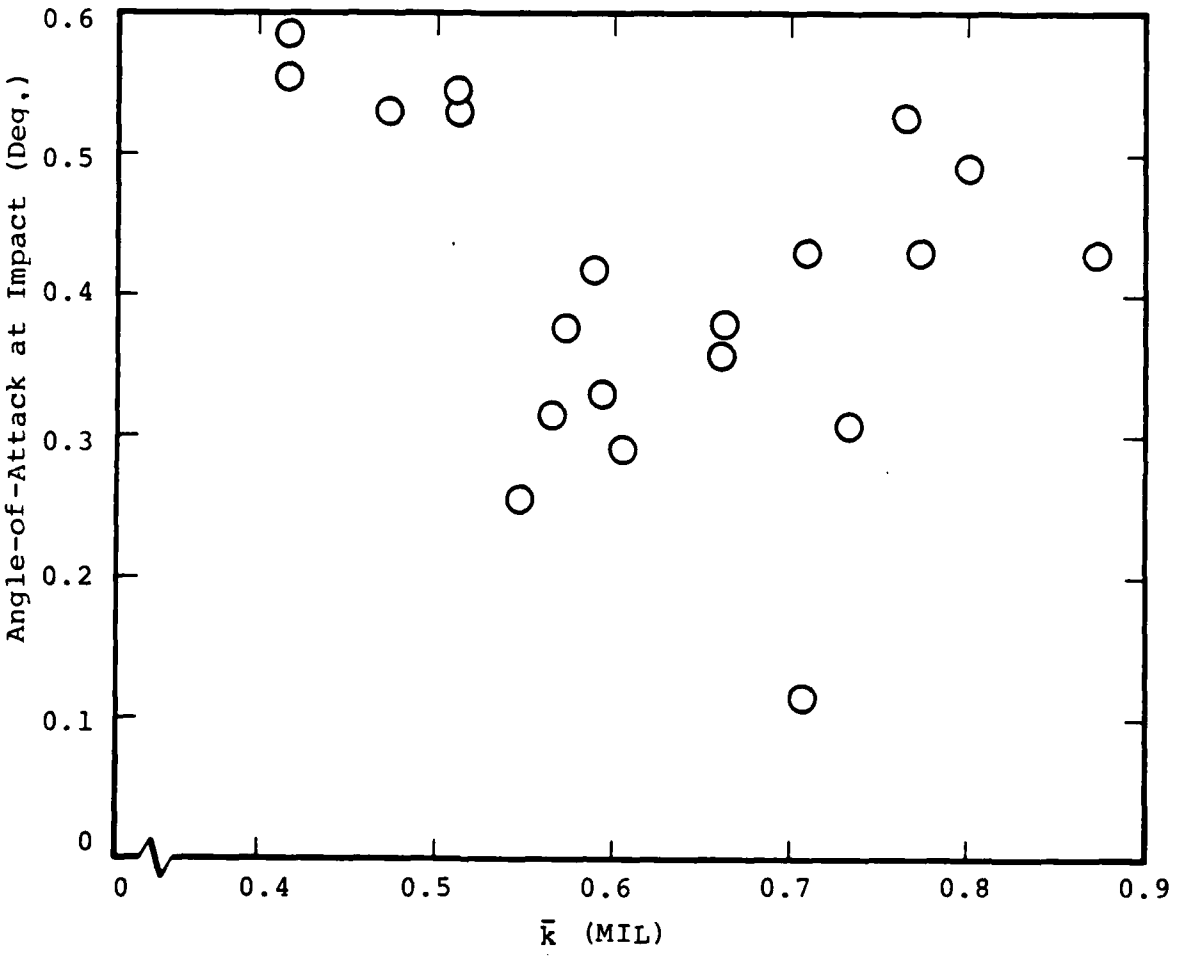

Figure 49. Sensitivity of Impact Trim Angle to Mean Laminar Roughness Height for RV3

variability on nosetip recession, these figures indicate that billet-to-billet variability has no direct functional effect on vehicle trim, the calculated data points showing no identifiable trends for either the blunt or sharp vehicles.

RV's 5,6,7 and 8 - These test cases include selected flight tests of an 8 percent bluntness ratio reentry vehicle as indicated in Table 7. All nosetips were constructed from 223/T-50 FWCC material and were selectively instrumental for nosetip recession. Nominal entry conditions are as indicated, but several of the vehicles flew slightly different trajectories. These cases are interesting primarily due to the multiple flights at nearly constant entry conditions of "identical" vehicles. Hence, some indication of material variability and the random nature of the asymmetric shape change process is obtained from these flight test results.

Twenty trials were computed for this test case using the parameters listed in Table 7 and the same billet-to-billet material variability parameters previously described for the 223/T-50 FWCC nosetips of RV's 3 and 4. Comparisons of measured and predicted nosetip material recession during entry are presented in Figure 50. Interestingly, the measured recessions are very nearly equal to the high, nominal and low results obtained in the twenty trial computations. The wide difference in measured recessions for the three flights clearly shows the importance of billet-to-billet variability and the error in predicted recession that can result on a particular flight test comparison. Specific pre-flight NDE or characterization procedures have been suggested in order to identify billets likely to have a high variance in performance from accepted norms. However, at the present time, the connection between transition and ablation performance and specific Quality Assurance type parameters such as density, open porosity, permeability, etc. is not firmly established. The results obtained from the present analysis clearly show the effect of the current billet-to-billet variability obtained due to processing variances.

Figure 51 compares the predicted and measured trim angle his-

Table 7

FLIGHT TEST PARAMETERS FOR RV'S 5 THROUGH 8

V_∞ @ 400 kft (fps)	22300*
γ_∞ @ 400 kft (deg)	27.5*
R_N (in)	0.861
R_B (in)	10.71
θ_f (deg)	9.033
R_N/R_B	0.08
Nosetip Material	223/T-50 FWCC
k_L (mil)	0.613
σ_k	0.37
k_s (mil)	1.74
f_v	1.0

*Nominal Values Used for Analysis

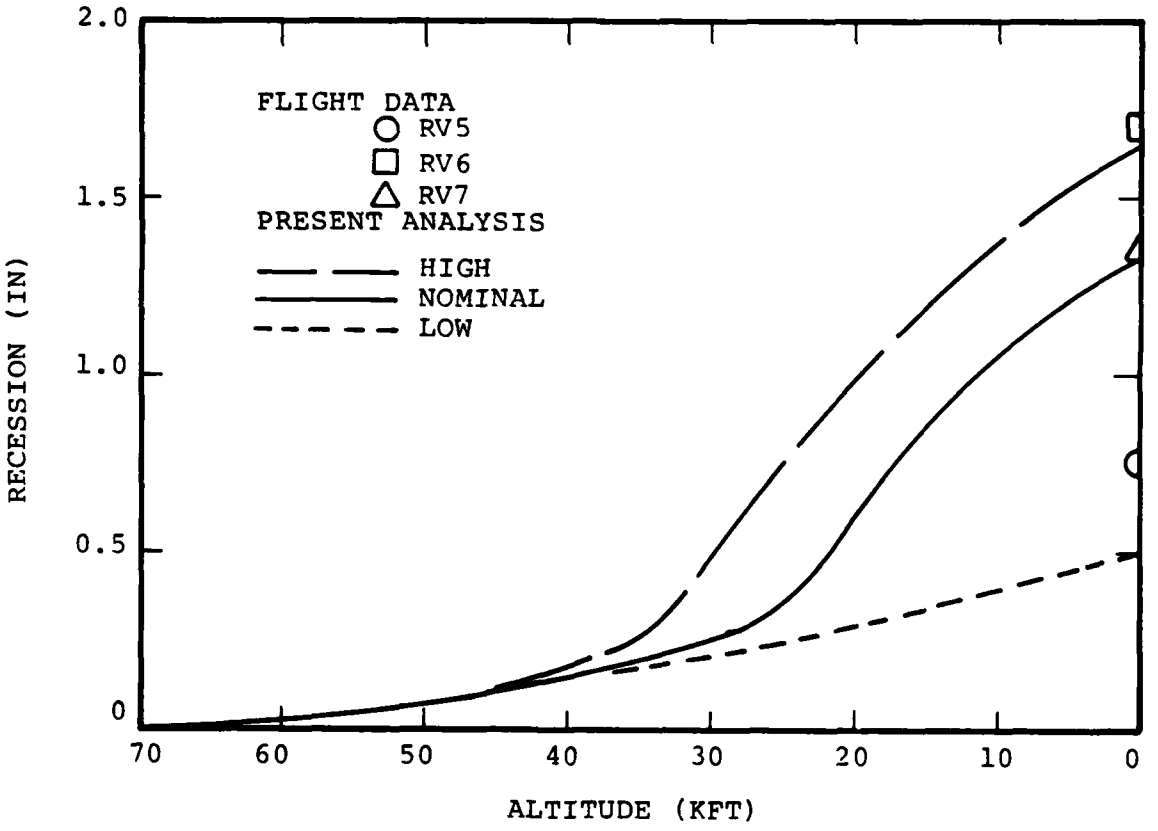

Figure 50. Nosetip Recession Correlation

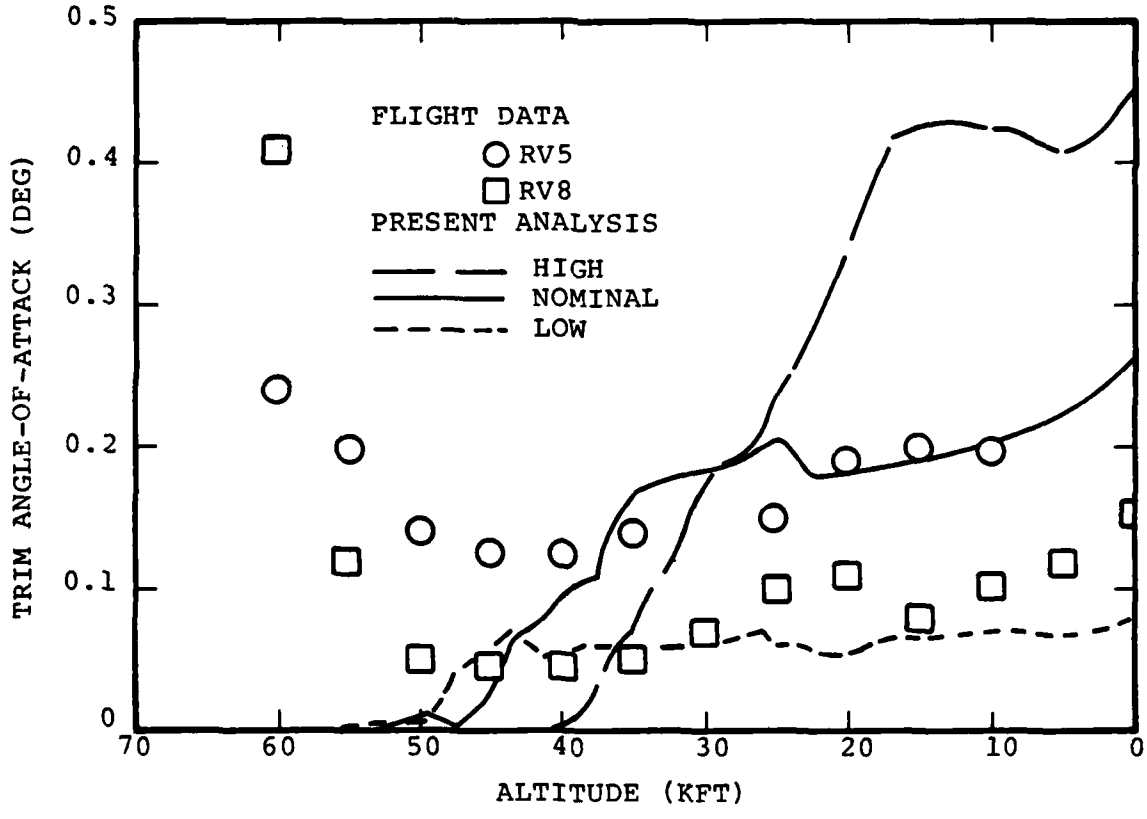

Figure 51. Correlation of Vehicle Trim Angles

tories for these slender vehicles. The measured data shows almost a factor or two difference in trim angle magnitudes and is similar to the low to nominal trials computed using the present method. The onset of trim angle buildup appears to be fairly well predicted for these cases and occurs between 40 and 50 kft. Higher altitude measured trims reflect the damping of initial vehicle angle-of-attack at deployment.

RV9, RV10 and RV11 - These three reentry vehicles flew slightly more severe reentry trajectories than those considered previously with maximum nosetip stagnation pressures of approximately 170 atm. These flights addressed several important reentry technology issues including a one-to-one comparison of the performance of different fine weave carbon-carbon materials. As seen in Table 8, the three vehicles differ only in the nosetip materials flown. All vehicles were of moderate bluntness ratio and a frusta amplification factor of 1.0 was assumed to be appropriate.

Table 8
FLIGHT TEST PARAMETERS FOR RV9, RV10 AND RV11

	RV9	RV10	RV11
V_a @ 400 kft (fps)	22325	22325	22325
γ_a @ 400 kft (deg)	30.2	30.2	30.2
R_N (in)	0.75	0.75	0.75
R_B (in)	5.0	5.0	5.0
θ_f (deg)	6.0	6.0	6.0
R_N/R_B	0.15	0.15	0.15
Nosetip Material	223/T-50 FWCC	223/PAN FWCC	FWPF/PAN
k_L (mil)	0.613	0.400	0.315
σ_k	0.37	0.325	0.158
k_s (mil)	1.74	4.2	2.4
f_v	1.0	1.0	1.0

Twenty trials were computed for the entry of each of these vehicles including the effects of billet-to-billet variability. Roughness parameters for the two 223 fine weave carbon-carbons were as previously discussed. For the PAN fine weave pierced fabric (FWPF) nosetip material less ground test ablation data is available. The values listed in Table 8 for FWPF/PAN have been derived primarily from post-test roughness measurements of 50MW ramp ablation test models (Reference 18) and indicate that laminar roughness elements developed by this material are both smaller in height and more uniform. Billet-to-billet variability is also reduced compared to 223 FWCC. The normalized standard deviation of the average laminar roughness height is 0.109 for FWPF/PAN material (compared to 0.154 for 223/T-50 and 0.17 for 223/PAN) and the minimum value is 0.15 mils. Based on these results, it is expected that the FWPF/PAN nosetip will undergo boundary layer transition at a significantly lower altitude than the 223/T-50 nosetip. Also reduced nosetip asymmetry would be expected to develop leading to lower trim angles. However, the delay of transition to lower altitudes tends to increase nosetip asymmetry for those cases when the nosetip boundary layer flow remains laminar over some segments.

Figure 52 presents a comparison of the recession histories measured and calculated for RV9. Calculated nosetip recessions vary from a low value of 2.25-in which is within the range of measurements obtained from the RV9 stagnation point recession gage to a high of 3.13-in. Predicted recession with the average laminar roughness value of 0.613 mils is approximately 2.86-in. These results should be compared with those of the 223/PAN FWCC nosetip (RV10) presented in Figure 53. Calculations for this nosetip material using the roughness parameters previously delineated including the effect of billet-to-billet variability yield a nominal predicted recession 23 percent lower than that calculated for RV9. This decreased nominal recession occurs due to the lower average laminar roughness height of the PAN material (0.40 compared to 0.613 mils) resulting in lower altitude transition and nosetip sharpening. However, because of its larger sand roughness height, the PAN material experiences a greater turbulent recession rate once the nosetip has

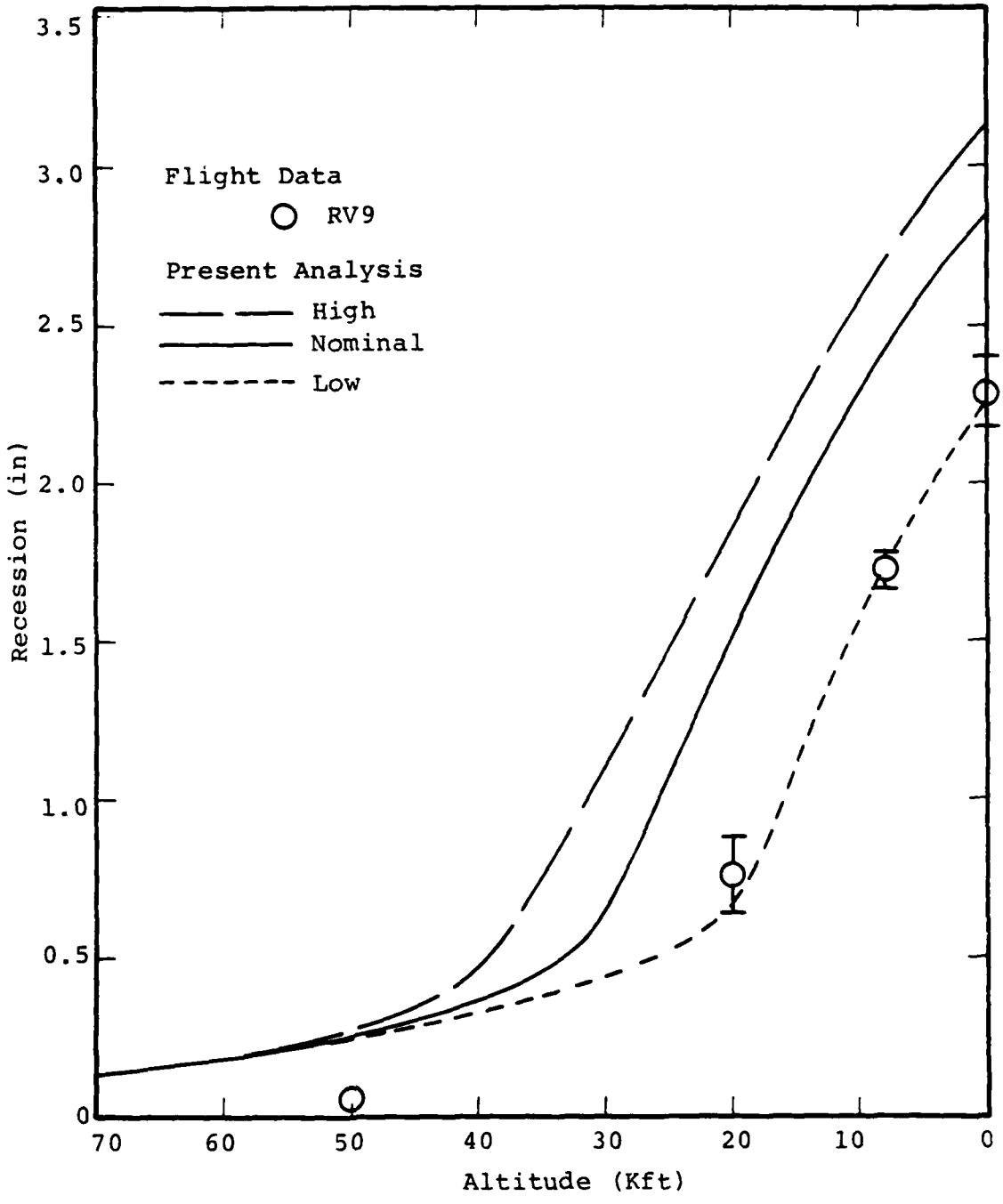

Figure 52. RV9 Nosetip Recession

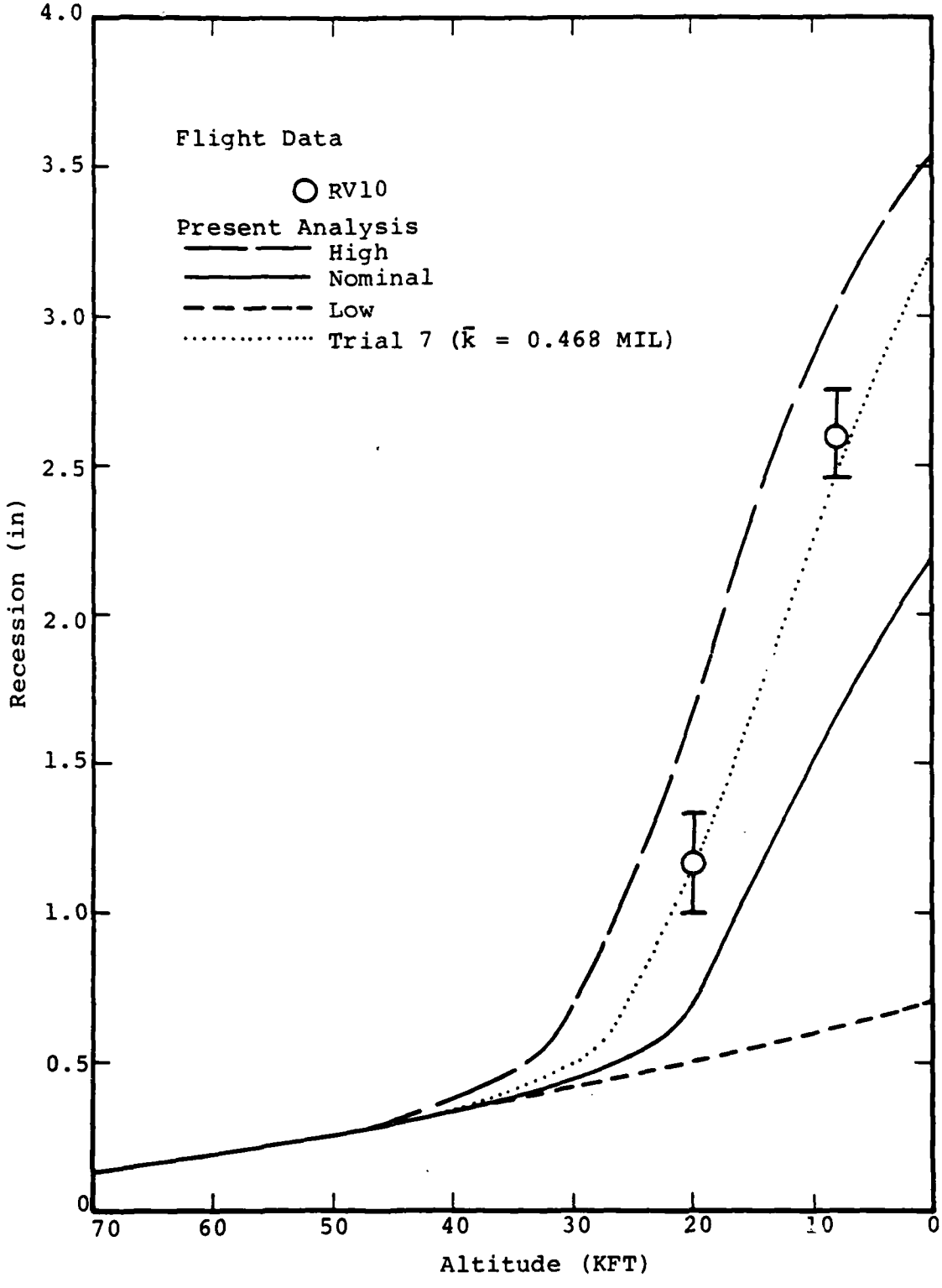

Figure 53. RV10 Nosetip Recession

sharpened. Hence, the "high" recession for the PAN material is 14 percent larger than the corresponding value for the T-50 223 FWCC nosetip. The data comparison presented in Figure 53 would indicate that the RV10 nosetip FWCC material had a somewhat higher than nominal laminar roughness. As shown, an excellent match of flight measured data occurred for a trial calculation wherein the assigned mean laminar roughness height was 0.468 mils.

Figure 54 presents a comparison of measured and calculated nosetip recession for the FWPF/PAN nosetip vehicle (RV11). Much lower recessions were measured for this nosetip material consistent with the reduced average laminar roughness height of 0.315 mils. The measured recession at an altitude of 9.5 kft matches the lower bound of the calculations which indicate incomplete nosetip boundary layer transition, i.e., the formation of turbulent gouges, but not an isolated laminar stagnation region. The calculated recession for the nominal laminar roughness height is only 0.1 inches greater than the measured recession. Even with the improved billet-to-billet uniformity of this material mentioned previously, a wide variance in predicted recession is observed due to the sensitivity of recession to the average transition altitude. The very small recession measured at an altitude of 20 kft is inconsistent with all-laminar ablation theory and may be in error due to redeposition effects.

Comparisons of measured trim angle histories with those calculated using the present analysis method are presented in Figures 55 through 57. Both RV9 and RV10 show fair agreement of the analytical results with measured data except at the lower altitudes. Flight derived pitching moment coefficients have been shown to be lower than theoretical at the lower altitudes which may have lead to the larger measured trim angles. This may indicate that for the specific nosetip shapes developed on the test flights the frusta amplification factors should be larger than unity. However, the analytical results do predict larger trim angles for RV10 compared to RV9 in good agreement with the measured data. The measured trim angle history of RV11 is anomalous and has not been explained fully

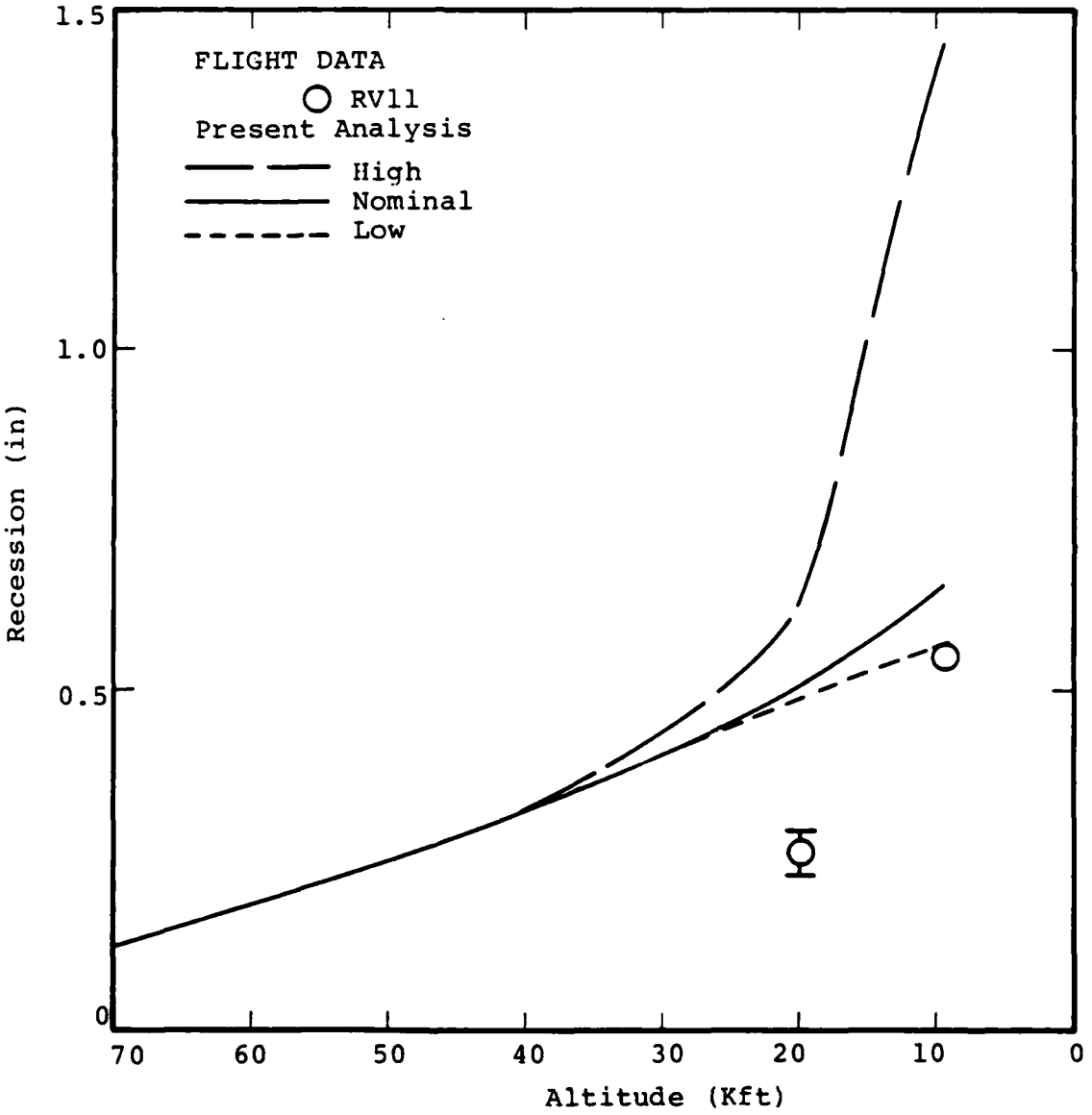

Figure 54. RV11 Nosetip Recession

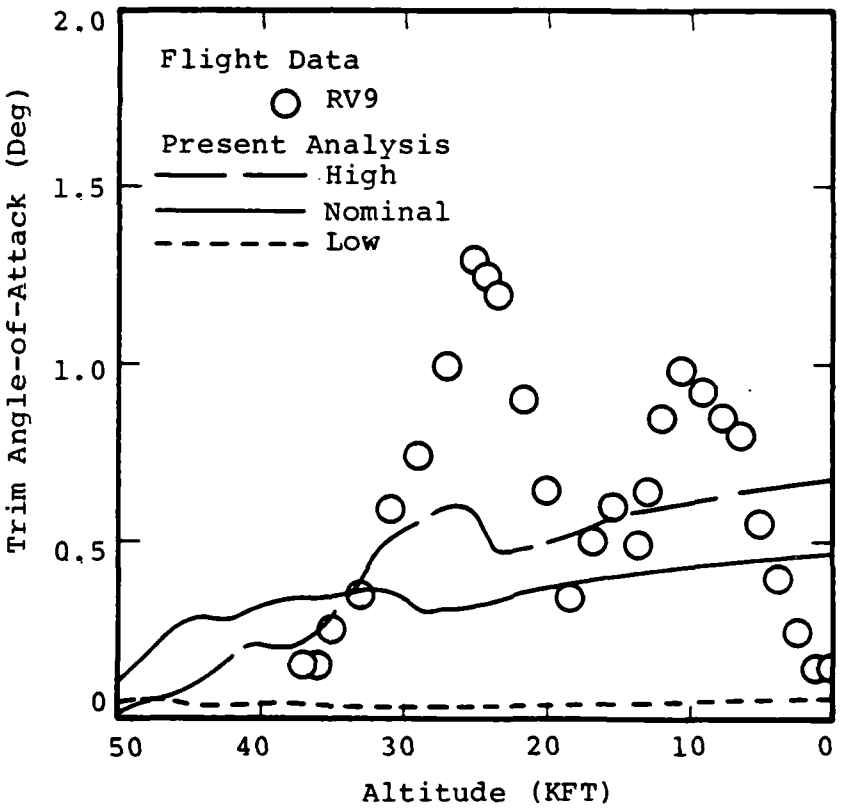

Figure 55. Trim Angle Correlation for RV9

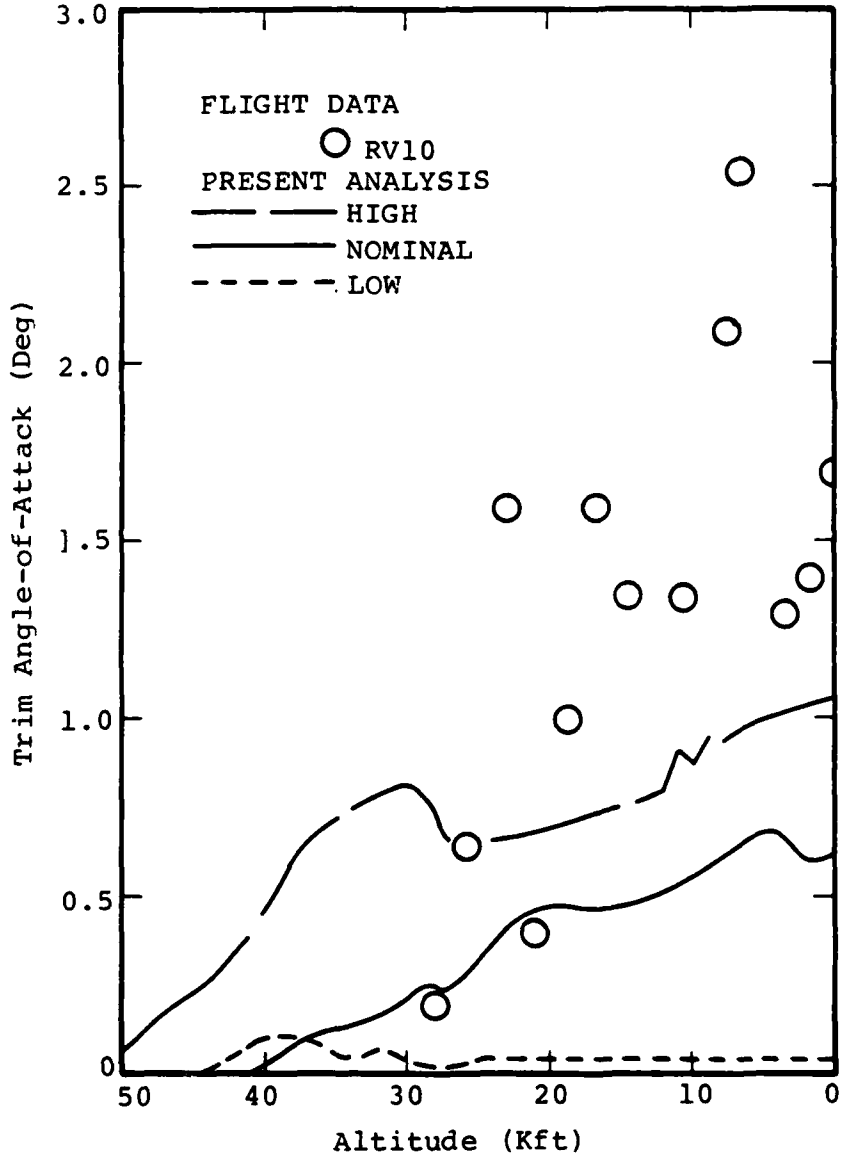

Figure 56. Trim Angle Correlation for RV10

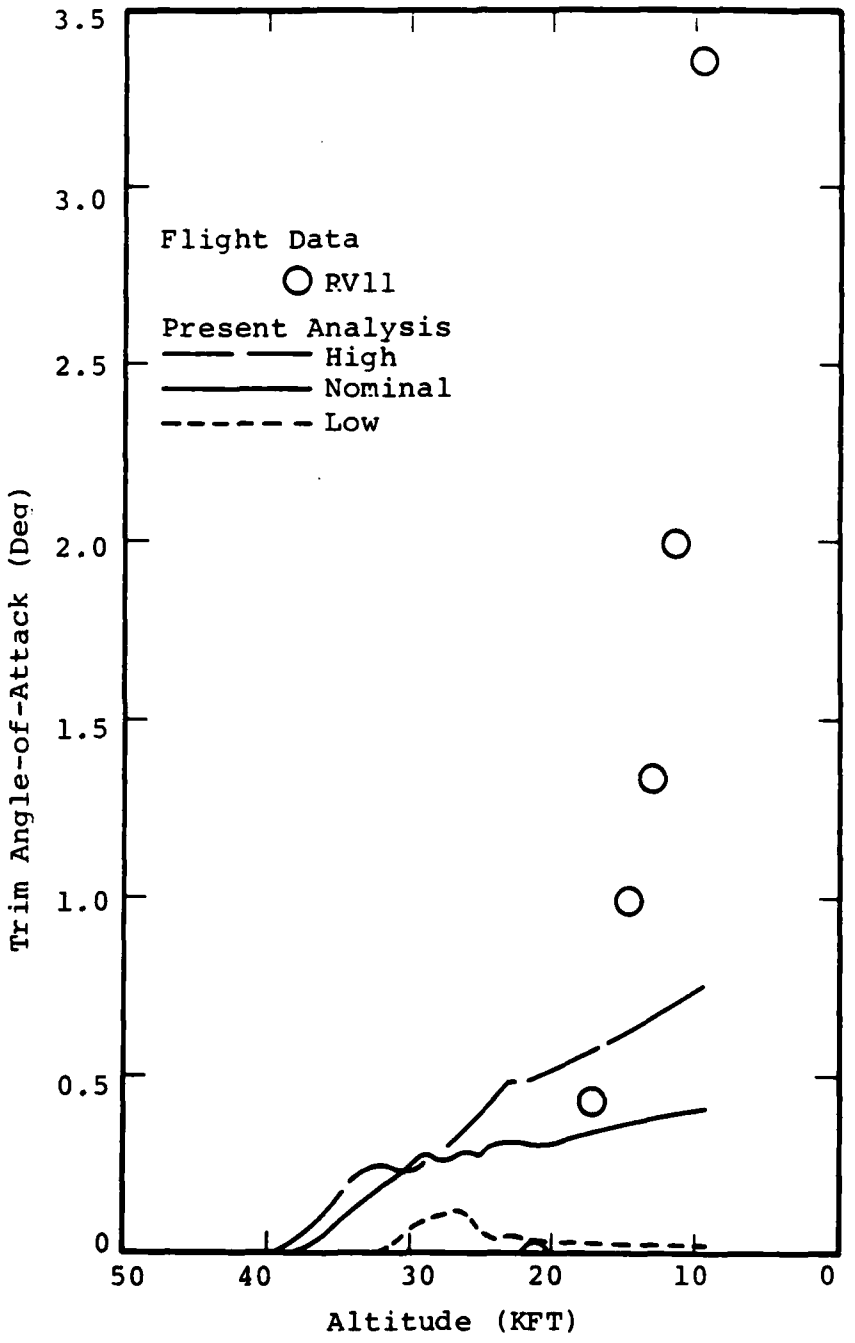

Figure 57. Trim Angle Correlation for RV11

at the present time. The trim history data is most consistent with the development of a single large gouge on the nosetip although this explanation does not explain all measured test data nor the vehicle demise at approximately 10 kft altitude. Apparently, a 3σ event related to nosetip material (and/or attachment) degradation significantly influenced vehicle performance on this flight. While the analytical results obtained for RV11 indicate a lower trim onset altitude compared to RV's 9 and 10 in agreement with the measured data, the measured trim angle is over four times greater than the highest calculated value. It might be noted that as a group these vehicles exhibited anomalous behavior in roll performance as well as trim angle-of-attack. RV's 9 and 10 both experienced roll-through-zero at low altitudes while RV11 spun-up to 14 Hz at demise. These results are consistent with the development of highly asymmetric nosetip shapes and significant nosetip coupling to full vehicle aerodynamics.

Table 9 and Figures 58 through 60 summarize the direct nosetip material related performance effects which can be derived from the analytical calculations performed for these three reentry vehicles. As seen in Table 9, the mean recession values predicted for the nosetips are directly correlated with their respective mean transition altitudes defined as the altitude at which ten (one-half the maximum number) turbulent gouges have occurred on the nosetip. However, the largest recession may occur with the 223/PAN material due to its larger value of sand roughness. Figure 58 presents histograms of the calculated nosetip recessions for 20 trials of each material. Also indicated are the computed mean values for each material. This figure readily illustrates the large performance variances expected for the 223/PAN nosetip material. While both the 223/T-50 and FWPF/PAN materials evidence narrow peaked frequency distributions, the 223/PAN material's distribution is broad and fairly flat. Approximately 15 percent of the calculated recessions are in the low recession (0.5 to 1.0-in) regime wherein significant nosetip sharpening has not occurred. Twenty percent of the calculated recessions exceed 3.13 inches, the largest recession calculated for the 223/T-50 nosetip.

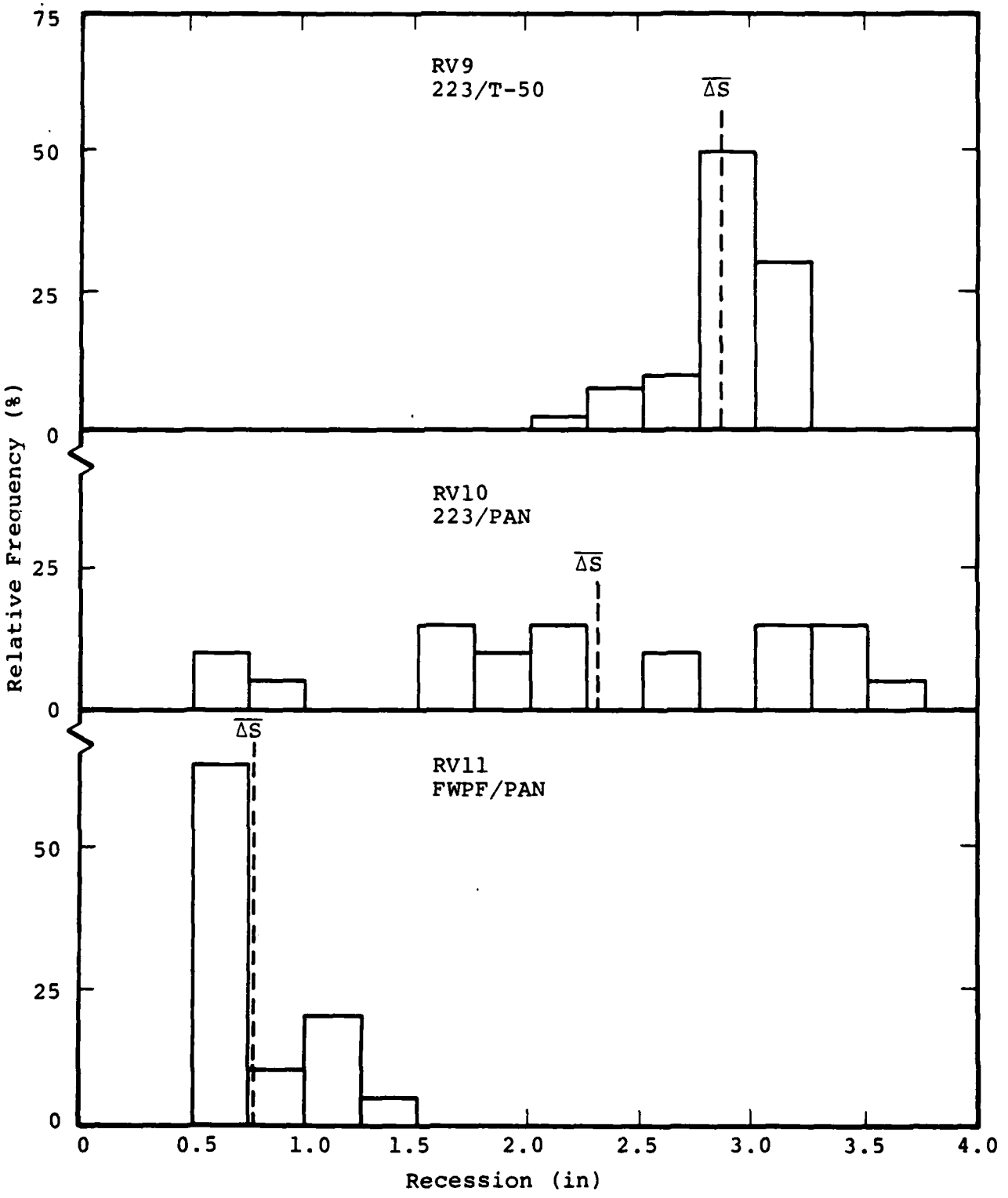

Figure 58. Nosetip Material Recession Performance

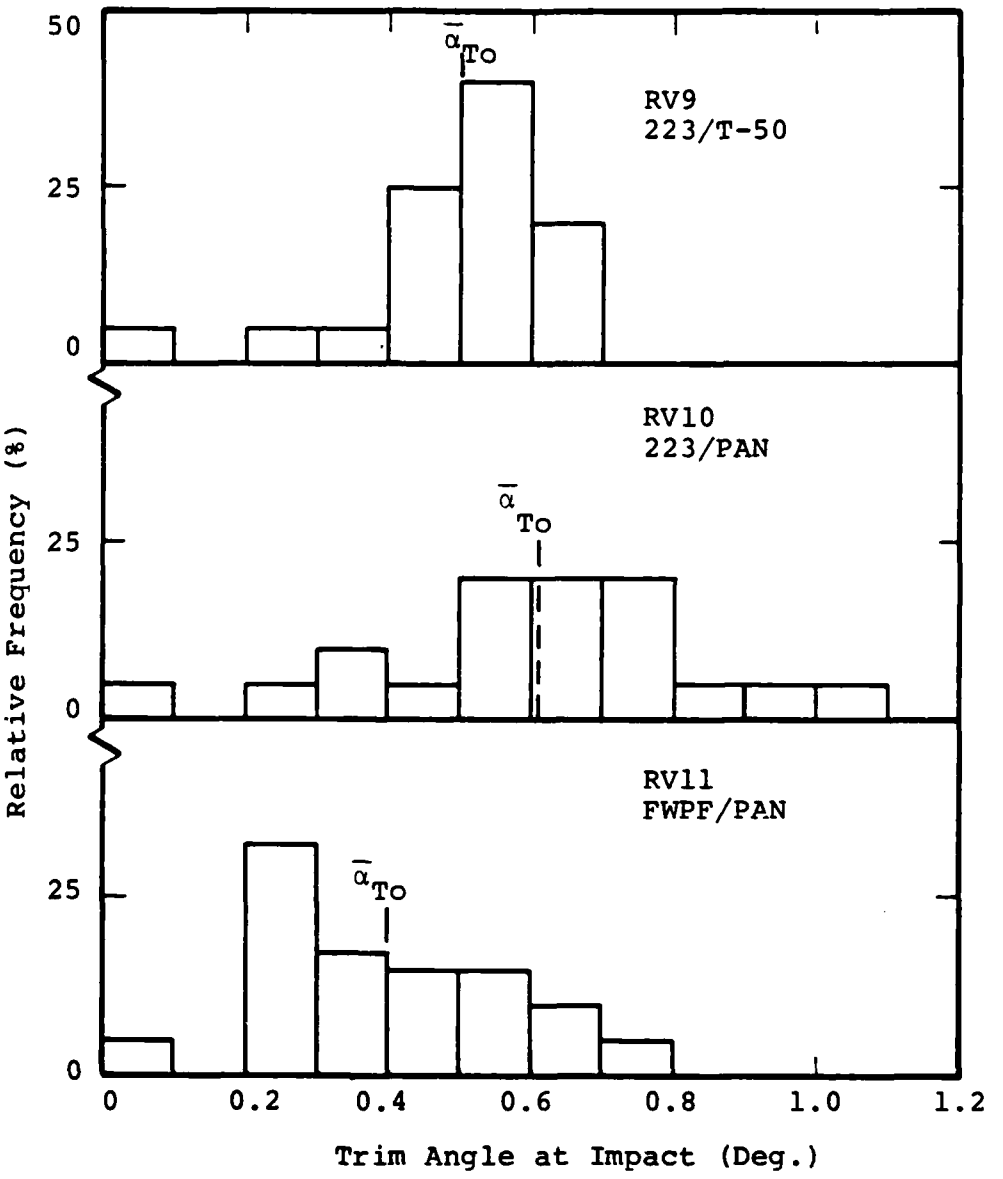

Figure 59. Vehicle Trim Performance

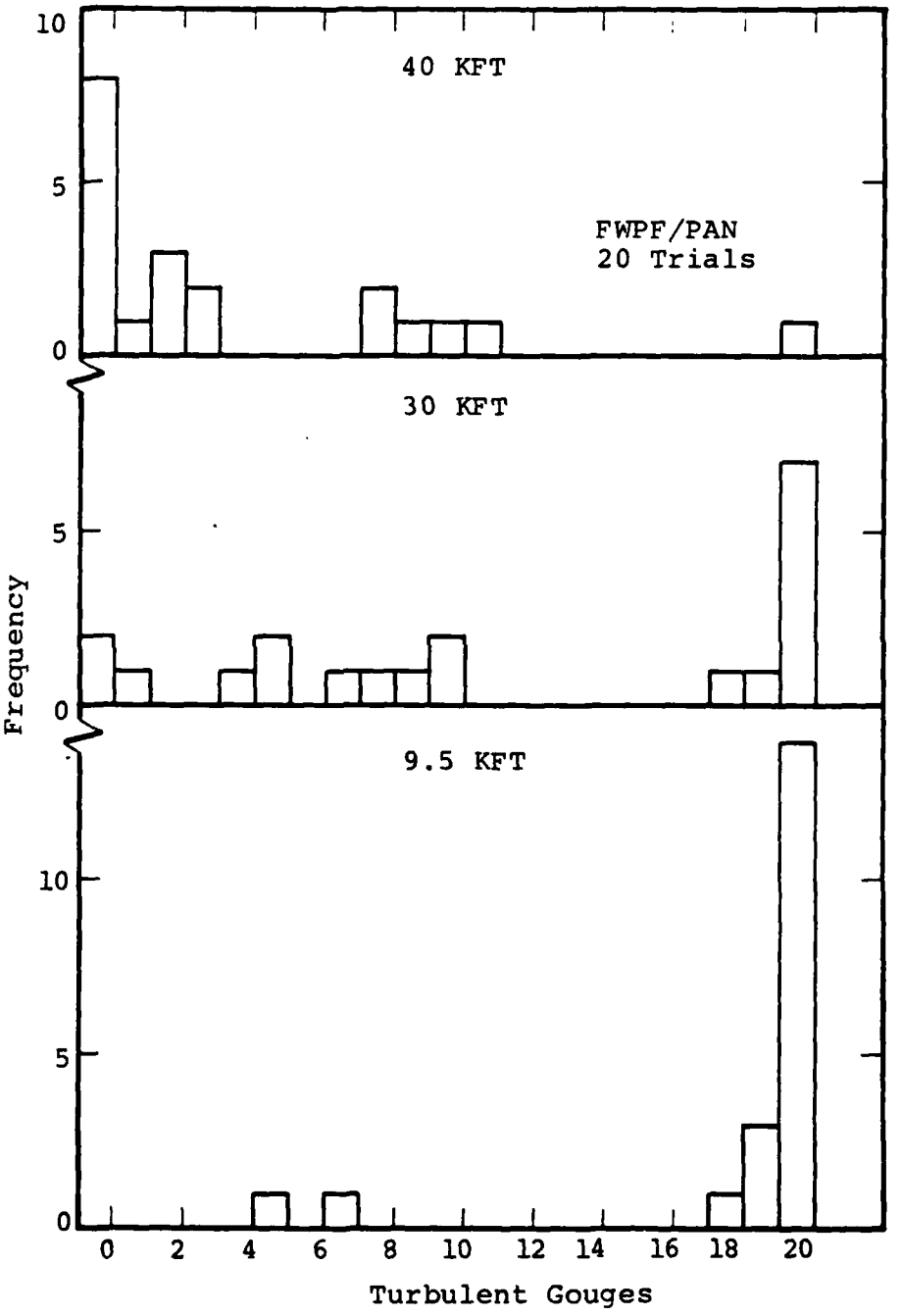

Figure 60. RV11 Nosetip Transition

Figure 59 illustrates the frequency distribution of vehicle trim angle-of-attack at impact for each of the three vehicles. Also shown are the calculated mean values (see also Table 9). It is noted that both the mean value and the standard deviation calculated for the 223/PAN material are larger than those of the other two materials. As previously noted, the distribution width for the lower altitude transitioning FWPF/PAN material tends to be slightly larger than that of the larger roughness 223/T-50 material. The mean and standard deviation of the trim angle at impact are seen to be nearly proportional to the corresponding laminar region offset parameters indicating the importance of this nosetip asymmetric shape parameter. However, some increase in the mean trim for the 223/PAN nosetip vehicle is noted due probably to the larger variance of nosetip shape change experienced with this material.

Table 9

EFFECT OF NOSETIP MATERIAL ON ENTRY PERFORMANCE

Parameter Mean Value ± Std. Dev.	NOSETIP MATERIAL		
	223/T-50 (RV9)	223/PAN (RV10)	FWPF/PAN (RV11)
Nosetip Recession (in)	2.84 ± 0.24	2.30 ± 0.92	0.78 ± 0.25
Mean Transition Altitude (KFT)	52.2 ± 4.8	40.1 ± 10.2	28.4 ± 12.0
Trim Angle at Impact (deg)[1]	0.50 ± 0.15	0.61 ± 0.24	0.40 ± 0.18
Laminar Region Offset at Impact (in)[1]	0.087 ± 0.027	0.088 ± 0.043	0.062 ± 0.027
Probability of Laminar Region Formation at Impact[1]	1.0	1.0	0.9

[1]RV11 Values at 9.5 KFT

The data of Table 9 also indicates that all of the three nosetip materials have a high probability of forming an isolated laminar stagnation region completely surrounded by turbulent flow for this entry condition. Both of the 223 materials do not exhibit

a single trial with incomplete turbulent gouging at impact. Two trials calculated for the FWPF/PAN nosetip, however, showed incomplete laminar stagnation region formation as illustrated in Figure 60. This figure presents for RV11 the frequency of occurrence of a given number of gouges - zero to the maximum number of 20 - at three altitudes. At 40 kft altitude, the most likely number of gouges is zero; however, several trials had 8 to 11 gouges occur and one trial evidenced transition on all 20 nosetip segments. By 30 kft, only two trials evidenced all laminar flow, more trials evidenced 4 to 10 turbulent gouges, and 9 trials had 18 to 20 gouges. By 9.5 kft, all but two trials had turbuelnt flow completely surrounding the laminar stagnation region. The remaining two trials resulted in only 5 and 7 turbuelnt gouges. It should be noted that even for the trials which show 18 or 19 turbulent gouges rather than the maximum value of 20 completely turbulent flow exists over the nosetip periphery because of the angular spreading of the turbulent gouges. That is, only 18 or 19 gouges may be formed because early occuring turbulent gouges may spread into adjacent laminar regions causing turbulent flow to be established for the adjacent segment even though transition has not been predicted based on the assigned roughness height.

3.2 PARAMETRIC STUDIES

Selected parametric studies are presented in this section. These results have been obtained with the asymmetric shape change model and the simplified vehicle aerodynamics model described earlier.

Entry Trajectory - The influence of entry trajectory on nosetip ablation and shape change has been investigated for a fixed vehicle configuration similar to that of RV's 5 through 8 described earlier. Pertinent vehicle characteristics are presented in Table 10. A single nosetip material, FWPF/PAN, was investigated. Assigned material parameters were as previously discussed for the FWPF/PAN nosetip flown on RV11 and billet-to-billet variability was included. Five entry trajectories were considered as listed in Table 11. Also shown are the respective maximum nosetip stagnation pressures encountered on

each trajectory. These trajectories encompass both high and low entry angles and velocities so that flight time from 300 kft altitude and maximum stagnation pressure vary significantly over the entry conditions.

For each entry trajectory, twenty trials were computed to determine nosetip shaping and approximate vehicle trim history characteristics. Table 12 summarizes the pertinent shape change and vehicle trim parameters determined from the entry trials. Average nosetip recessions calculated from the twenty trials are seen to be fairly low

Table 10
VEHICLE CHARACTERISTICS

R_N (in)	0.861
R_B (in)	10.71
θ_f (deg)	9.033
R_N/R_B	0.08
f_v	1.0

Table 11
ENTRY TRAJCETORIES

Trajectory Number	V_∞ @ 400 KFT (FPS)	γ_∞ @ 400 KFT (DEG)	$P_{s\ max}$ (ATM)
1	22300	27.5	108.
2	21500	21.0	85.
3	23000	42.0	153.
4	26500	30.0	160.
5	25500	21.0	116.

for the FWPF/PAN nosetip material modeled. Relatively low values of the standard deviation of the calculated recessions are also evident for the lower stagnation pressure trajectories (1, 2 and 5). Comparison of the average number of turbulent gouges occurring on the nosetip at impact (n_{T_O}) indicates that only on the two trajectories where high stagnation pressures are obtained do a significant fraction of the nosetip segments experience turbulent flow. Hence, nosetip sharpening and the attendent high recession rates are unlikely to occur. As indicated by the results shown for the maximum and minimum (of the twenty trials) values of recession, the distribution of calculated nosetip recessions is skewed and not well represented by the mean and standard deviation. In particular, the frequency of occurrence of large recessions is higher than would be expected based on a normal distribution with the calculated mean and standard deviations and the mean is baised toward lower recessions due to the fixed minimum recession which occurs for all-laminar nosetip boundary layer flow. Further definition of the nosetip transition statistics is given by the mean and standard deviations calculated for the average nosetip transition altitude, $\bar{h}_T$. For this data $\bar{h}_T$ was assigned a value of zero for those trials which had less than 10 gouges at impact. Because of this, very low mean transition altitudes and large standard deviations are indicated in Table 12. Transition altitudes are seen to be almost a direct function of trajectory maximum stagnation pressure as would be expected. Table 13 summarizes the transition performance of the FWPF/PAN nosetip material by presenting the relative frequency of occurrence of turbulent gouges on the nosetip for each trajectory. All laminar nosetips were calculated for trajectories 1, 2 and 5 with 20, 75 and 20 percent probability, respectively. Almost all turbulent nosetips occurred on trajectories 1, 3, 4 and 5 with 20, 85, 80 and 20 percent probability, respectively. Trajectory 2, therefore, exhibited the most consistent nosetip performance because of the low stagnation pressure. The high pressure trajectories (3 and 4) also exhibited fairly consistent nosetip performance with a high

Table 12

FWPF/PAN NOSETIP ENTRY PERFORMANCE

Parameter Mean ± Std. Dev.	TRAJECTORY 1	2	3	4	5
ΔS_o (in)	0.382 ± 0.030	0.445 ± 0.004	0.439 ± 0.154	0.720 ± 0.257	0.611 ± 0.065
$\Delta S_{o\ max}$ (in)	0.478	0.463	0.939	1.489	0.846
$\Delta S_{o\ min}$ (in)	0.365	0.444	0.317	0.506	0.579
n_{T_o}	6.0 ± 7.5	0.8 ± 2.0	17.4 ± 6.2	16.6 ± 6.8	5.7 ± 7.5
$\bar{h}_T$ (KFT)	5.6 ± 11.6	0.0 ± 0.0	24.0 ± 12.2	25.0 ± 13.6	6.34 ± 13.2
Δ_o (in)	0.040 ± 0.047	0.009 ± 0.025	0.061 ± 0.036	0.070 ± 0.037	0.039 ± 0.047
ψ_o (Deg)	0.175 ± 0.135	0.049 ± 0.097	0.164 ± 0.084	0.179 ± 0.084	0.247 ± 0.184
α_{T_o} (Deg)	0.284 ± 0.194	0.083 ± 0.159	0.186 ± 0.081	0.220 ± 0.114	0.376 ± 0.268
$\alpha_{T_{o\ max}}$ (Deg)	0.620	0.480	0.363	0.504	0.913

Table 13

FWPF/PAN NOSETIP TRANSITION

Number Of Gouges At Impact	RELATIVE FREQUENCY FOR TRAJECTORY 1	2	3	4	5
0	0.20	0.75			0.20
1	0.15	0.10		0.05	0.20
2	0.15		0.10	0.05	0.20
3	0.10	0.05			0.05
4	0.05	0.05			
5	0.05		0.05	0.05	0.05
6				0.05	
7					0.05
8	0.10	0.05			0.05
-					
-					
-					
18				0.05	
19	0.05		0.05		0.05
20	0.15		0.80	0.75	0.15

percentage of nearly all turbulent nosetips, only a small percentage of nearly all-laminar nosetip and no all-laminar trials. The intermediate pressure trajectories (1 and 5) show a small preference for blunt, nearly-laminar nosetips, but nearly all-turbulent cases occur with about 20 percent probability. The statistics of the two asymmetric shape parameters Δ and ψ are also presented in Table 12. Somewhat smaller asymmetries as measured by the parameters are evident in comparison to those typically obtained for higher altitude transitioning materials. With the exception of trajectory 2, only small effects of trajectory entry conditions are noted.

The effect of nosetip asymmetries on vehicle aerodynamics is approximately given by the vehicle trim angle-of-attack behavior at impact. The data in Table 12 indicates that the impact trim angle statistical properties generally follows the corresponding laminar region offset properties. Small trims are prevalent for trajectory 2 entries. The largest trims and the highest single trim predicted for the various entry conditions occur on trajectory 5. Some slight reduction in trims are seen on the two high stagnation pressure trajectories compared to the two intermediate pressure trajectories. The correlation of impact trim angle with total nosetip recession at impact is shown in Figures 61 and 62 for trajectories 4 and 5, respectively. Figure 61 for the high stagnation pressure trajectory 4 shows a trend toward decreasing trim angle with increasing recession although the variance in predicted trims at low values of nosetip recession is very large. The noted trend is consistent with the expectation that more complete transition leads to reduced nosetip asymmetries. For the intermediate stagnation pressure trajectory 5, the frequency of occurrence of nearly all-laminar flights is much higher than for trajectory 4. Hence, no discernable trend can be ascribed to the data. It is interesting to note, however, the wide range of trims predicted for a nearly constant recession of 0.58 in.

Transition Altitude - The sensitivity of nosetip and vehicle performance to the mean altitude of transition determined by the nosetip material laminar roughness characteristics was investigated for a single slender vehicle (defined in Table 10) and the intermediate

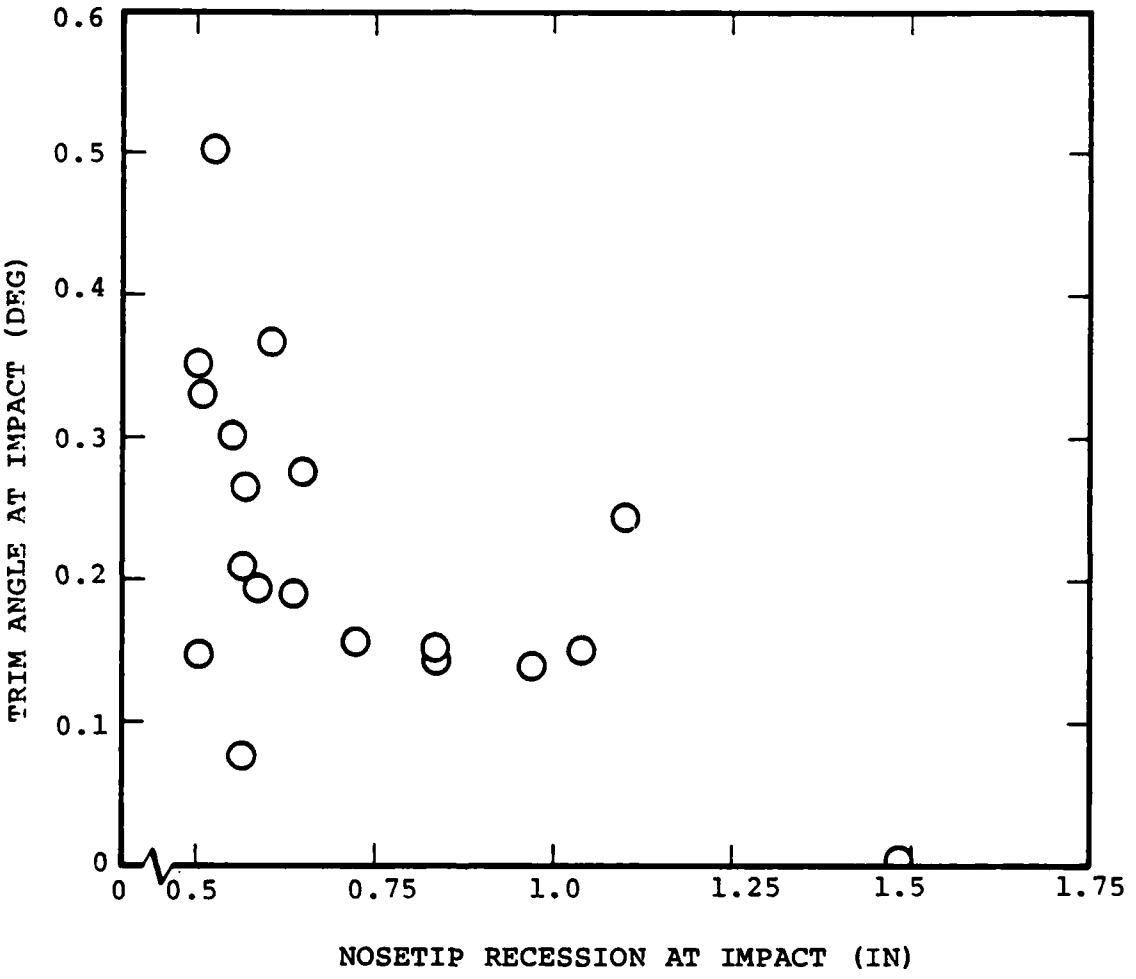

Figure 61. Correlation of Vehicle Trim and Nosetip Recession, Trajectory 4

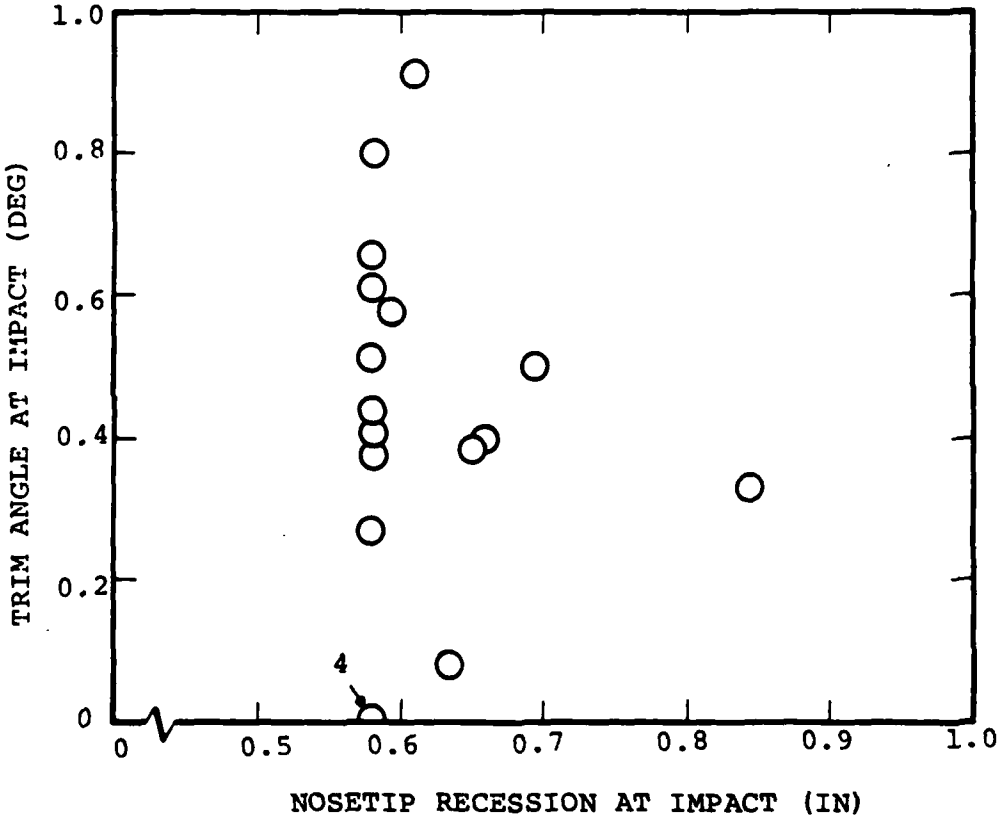

Figure 62. Correlation of Vehicle Trim and Nosetip Recession, Trajectory 5

stagnation pressure trajectory (No. 1 in Table 11). Three materials were considered: FWPF/PAN, 223/T-50 and a high-altitude transitioning (HAT) material. The roughness properties of the first two materials were identical to those previously given for these materials. For the HAT material, an average laminar roughness height of 2.0 mils was assigned in order to obtain high altitude transition. Other appropriate laminar roughness properties were obtained from the properties of 223/T-50 by linearily scaling by the ratio of 2.0 to 0.613. In order to determine only the influence of transition altitude, the bulk density and sand roughness of the HAT material were taken to be identical to those of 223/T-50.

Table 14 summarizes the results obtained and provides a comparison of the performance of the three materials. As expected, average nosetip recession increases significantly with increasing mean transition altitude. The standard deviation of nosetip recession is largest for the intermediate roughness 223/T-50 FWCC since both nearly laminar and nearly turbulent nosetip shapes are predicted. The higher roughness of the HAT material is successful in reducing nosetip recession variance as is the low roughness of the FWPF/PAN material for this trajectory. The mean transition altitude of the HAT material is almost 20 kft higher than that of 223/T-50 and both materials evidence fully turbulent nosetip flow at impact for every trial computed. The asymmetric shape parameters Δ and ψ are also reduced somewhat for the HAT material nosetip compared to the 223/T-50 nosetip, but are about equal to those ssen for the FWPF/PAN material. As expected, these results for Δ and ψ yield nearly corresponding results for the vehicle trim angle-of-attack at impact. That is, the HAT material reduces the average α_T by about 30 percent compared to the 223/T-50 material and 37 percent compared to the FWPF/PAN material. Nearly corresponding reductions in maximum calculated impact trim angle are also seen.

The above results indicate that the use of a high altitude transitioning material may provide some improvement in the degree of nosetip shape change asymmetry obtained during entry. This effect

Table 14

SENSITIVITY OF NOSETIP ENTRY PERFORMANCE
TO LAMINAR ROUGHNESS

Parameter Mean ± Std. Dev.	FWPF/PAN K_L= 0.315 Mil	223/T-50 K_L= 0.613 Mil	HAT K_L= 2.0 Mil
ΔS_o (in)	0.382 ± 0.030	1.284 ± 0.321	1.736 ± 0.023
$\Delta S_{o\ max}$ (in)	0.478	1.654	1.783
$\Delta S_{o\ min}$ (in)	0.365	0.502	1.704
$\bar{h}_T$ (KFT)	5.6 ± 11.6	46.0 ± 5.1	65.5 ± 3.1
n_{T_o}	6.0 ± 7.5	20.0 ± 0.0	20.0 ± 0.0
Δ_o (in)	0.040 ± 0.047	0.076 ± 0.034	0.049 ± 0.026
ψ_o (Deg)	0.175 ± 0.135	0.225 ± 0.090	0.153 ± 0.079
α_{T_o} (Deg)	0.284 ± 0.194	0.254 ± 0.098	0.179 ± 0.092
$\alpha_{T_{o\ max}}$ (Deg)	0.620	0.454	0.387

might be expected to contribute to a reduction in the reentry vehicle circular error probability (CEP) due to the resulting lower vehicle trim angles and lift forces. However, a compensating effect is that, although the trim magnitudes are lower, trim buildup occurs at a higher altitude so that dispersive velocities generated due to lift non-averaging have a longer time to propagate to impact. Selected calculations performed with the full SAI dispersion computer code developed during this study indicate that the net effect of using a HAT nosetip material is an increase rather than a decrease in vehicle roll-trim contribution to CEP. For instance, for vehicle and entry conditions similar to those presented in Table 14, the CEP (considering only roll-trim dispersion sources) of the HAT material nosetip reentry vehicle was calculated to be about 50 percent larger than that of the 223/T-50 nosetip vehicle.

Roughness Element Size Distribution - The effect of the standard deviation of the roughness element height distribution on entry performance was determined by varying σ_k from the FWPF/PAN baseline value of 0.158. Trajectory 1 and the previous slender vehicle were again used for this investigation. An "improved" version of FWPF/PAN with σ_k reduced by a factor of two from the nominal value was considered. Also included in the investigation was a FWPF/PAN material with σ_k increased to 0.370, the value of σ_k for 223/T-50 FWCC. In both off-nominal cases, all other material properties including billet variability parameters were assigned the baseline values of FWPF/PAN material.

Table 15 summarizes the results obtained for the two off-nominal cases and provides a direct comparison with the results for baseline material. The average nosetip recession and standard deviation are relatively insensitive to σ_k, both increasing only slightly as σ_k is increased. Since the minimum recession remains fixed at the all-laminar nosetip value and larger σ_k produces an increase in the number and size of the larger roughness elements, these results are not surprising. Also, due to the increase in larger roughness elements, both the average mean transition altitude and the number of turbulent gouges on the nosetip at impact increase slightly with increasing σ_k.

Table 15

SENSITIVITY OF NOSETIP ENTRY PERFORMANCE
TO ROUGHNESS ELEMENT VARIANCE

Parameter Mean ± Std. Dev.	Improved FWPF/PAN σ_k= 0.079	Nominal FWPF/PAN σ_k= 0.158	FWPF/PAN σ_k= 0.370
ΔS_o(in)	0.379 ± 0.027	0.382 ± 0.030	0.399 ± 0.055
$\Delta S_{o\ max}$(in)	0.464	0.478	0.596
$\Delta S_{o\ min}$(in)	0.365	0.365	0.365
$\bar{h}_T$(kFT)	5.7 ± 11.9	5.6 ± 11.6	6.6 ± 13.4
n_{T_o}	5.3 ± 7.9	6.0 ± 7.5	8.7 ± 7.0
Δ_o(in)	0.023 ± 0.032	0.040 ± 0.047	0.084 ± 0.058
ψ_o(Deg)	0.080 ± 0.089	0.175 ± 0.135	0.336 ± 0.164
α_{T_o}(Deg)	0.134 ± 0.140	0.284 ± 0.194	0.492 ± 0.213
$\alpha_{T_{o\ max}}$ (Deg)	0.406	0.620	0.977

Further definition of the transition behavior of the nosetip materials is given in Figure 63. Here the frequency of occurrence of a given number of turbulent gouges at impact is shown for the 20 trials computed for each nosetip material. The nominal baseline material shows only a small preference for all-laminar (zero gouges) behavior compared to 1 through 3 gouges. Also, 19 and 20 gouge trials are as likely to occur as zero gouge trials. The improved material with reduced σ_k tends to exhibit either all-laminar or all-turbulent flow. This type of performance should be expected since all nosetip segments either transition together or not at all because of the small variance in the roughness heights assigned for the nosetip segments in a specific trial. The proportion of all-laminar to all-turbulent shapes depends on both the trajectory and the distribution of nosetip average laminar roughness as influenced by billet-to-billet variability. For the material with the larger value of σ_k, 5, 6 and 7 gouges appear most frequently, the larger σ_k favoring larger roughness heights assigned to nosetip segments. All-laminar trials have been significantly reduced in frequency and the frequency of nearly all-turbulent trials is seen to be increased.

The dependency of the nosetip laminar region offset, cant and vehicle trim on σ_k is also presented in Table 15. Laminar region offset varies almost linearily (see Figure 64) with σ_k over the values investigated. Hence, reductions in material roughness element height variance can significantly reduce the asymmetry of the ablated nosetip shapes. Corresponding reductions in maximum and average trim angles at impact are also obtained at values of σ_k less than about 0.2; however, above that value, the rate of drop of trim angle is reduced.

3.3 CONCLUSIONS

The following conclusions summarize the results obtained in this study.

Asymmetric Nosetip Shape Change Modeling

It is feasible to model the development of asymmetric reentry

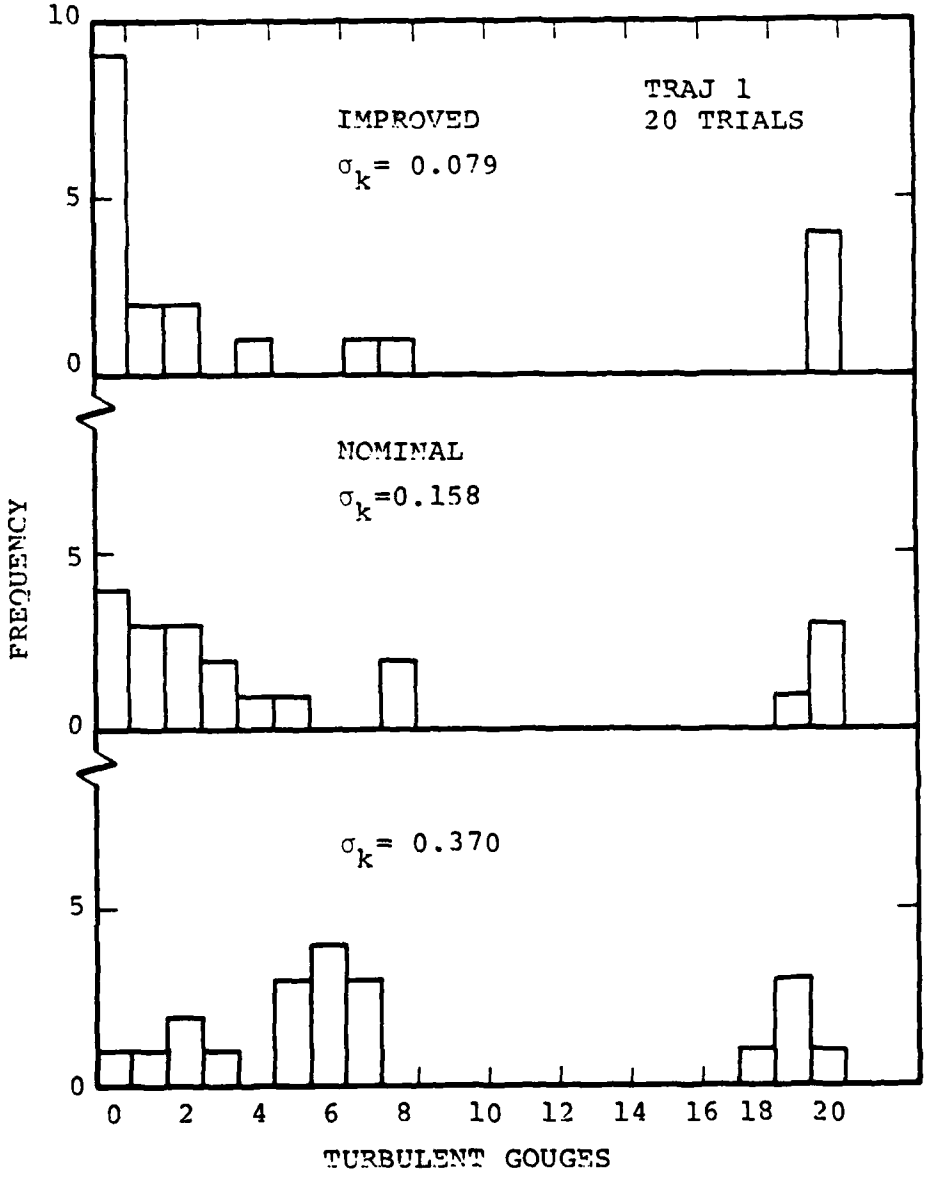

Figure 63. FWPF/PAN Nosetip Transition

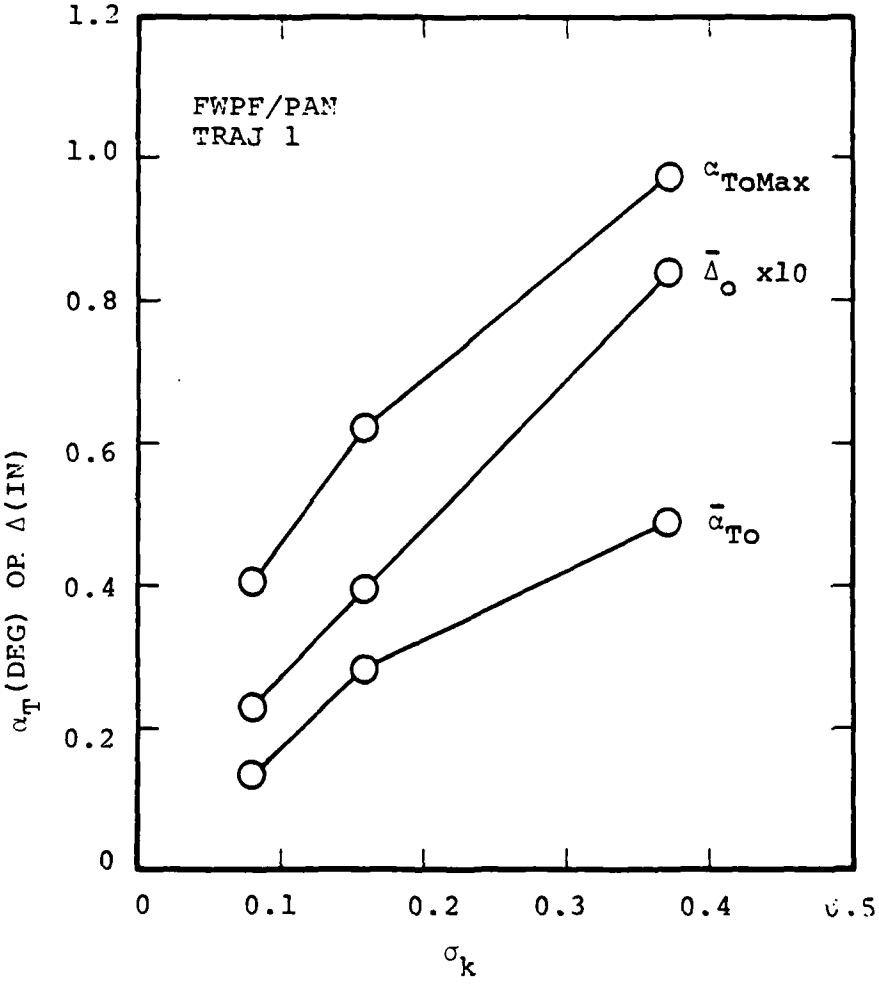

Figure 64. Effect of Roughness Element Std. Dev. on Entry Performance

vehicle nosetip shapes during entry using a multiple ray puesdo-random, statistical approach. Important features of the nosetip shape which must be considered are laminar region offset from the vehicle centerline, nosetip ray concavity and nosetip sharpening and the attendant influence of entropy swallowing on nosetip turbulent recession rate. Using the multiple ray approach, an asymmetric shape change model suitable for use in determining ballistic reentry vehicle aerodynamics and the contribution of nosetip asymmetric ablation to dispersion has been developed. The model uses approximate correlation equations for determining laminar and turbulent recession rates, boundary layer edge sonic point unit Reynolds number and momentum thickness, and laminar stagnation region wall temperature ratio and blowing rate. Each nosetip ray is assigned a time-varying roughness height which is determined randomly based on the roughness characteristics of the nosetip material. Using these roughness heights, detailed transition calculations based on boundary layer velocity and density profiles are used to predict transition onset and movement on each of the twenty nosetip rays describing the asymmetric nosetip shape. Hence, in the model, the variability of material surface roughness directly dictates the development of asymmetric nosetip shape change.

The analytical model developed has been verified by comparison of predicted results with flight test data measured for a range of reentry vehicle types, entry conditions, and nosetip materials. Using a consistent set of roughness characteristics derived for each material from surface roughness measurements on post-test ablation models and AFFDL 50MW arc-jet transition pressure data, good agreement between calculated and measured flight test data has been evidenced. In particular, measured nosetip recession and shape change has been correlated well by the model; vehicle trim angle magnitudes and behavior and windward meridian movement has also been well represented by the calculated results. In all cases, the analytical results demonstrate the stochastic nature of nosetip shape change and resulting vehicle aerodynamics.

Material Roughness Modeling

Important material laminar roughness characteristics include both the roughness element size distribution displayed by a given nosetip material sample and the variability of roughness characteristics evident on different samples of the same material; i.e., billet-to-billet (or sample-to-sample) variability. The former roughness property is characterized by the mean and variance of roughness element heights and determines the degree of asymmetry developed on a given nosetip flight realization. The later characteristic is defined by the variance of the average laminar roughness height measured on many material samples and determines the flight-to-flight variability of nosetip mean transition performance.

Another important parameter affecting nosetip transition and shape change performance is the time-varying nature of the surface roughness developed during material ablation. It was found that failure to account for this effect in the analytical modeling resulted in the persistent to very low altitudes of laminar segments (or ridges) on the nosetip which was inconsistent with flight observed nosetip shape change.

Preferential transition for orthogonal FWCC materials near the meridional rays 45-deg from the X-Y weave axes was found to influence asymmetric shape development but to be of lesser importance in determining vehicle trim angle magnitudes and behavior.

Material Effects on Nosetip Shaping

Three important material influences on nosetip shape change have been identified. First, the nosetip material's mean laminar roughness height controls the mean nosetip transition altitude for a given trajectory and, hence, the nosetip recession. Billet-to-billet variability, therefore, significantly influences the nosetip recession. For typical FWCC material variability, present results indicate that for some combinations of trajectory and material nosetip shape change histories typical of both all-laminar and fully-turbulent boundary layer flow may occur. Even on higher or lower pressure

trajectories, a significant variance in nosetip recession is predicted due to billet-to-billet variability effects on mean transition altitude and subsequent nosetip sharpening.

Second, asymmetric nosetip shape change is primarily controlled by the variance of the roughness element height distribution of the nosetip material. The laminar region offset developed which measures the "average" asymmetry of the nosetip shape change response is directly proportional to the roughness element height standard deviation. Vehicle trim angle-of-attack are correspondingly directly related to the roughness element height variance. Hence, the primary means of reducing nosetip asymmetries is by an increase in the uniformity of the roughness element heights developed during ablation. In this regard, it should be noted that apparently fine weave pierced fabric carbon-carbon is significantly more uniform and of lower average roughness than 3-D orthogonal 223 carbon-carbon materials.

Trajectory Sensitivities

Other than trajectories on which the nosetip material is capable of maintaining a high probability of nearly all-laminar nosetip ablation, little sensitivity of asymmetric shape change to trajectory parameters has been found. For the former trajectories, average nosetip asymmetries are reduced because of the frequency of occurrence of all-laminar nosetip shape change flights.

REFERENCES

1. E.A. English, Nosetip Recovery Vehicle Postflight Development Report. SAND75-8059, Sandia Laboratories, Livermore January 1976.

2. M. C. Fisher, Spreading of a Turbulent Distrubance, AIAA Journal, Vol. 10, No. 7, pps. 957-958, July 1972.

3. R. B. Dirling, Jr., A Method for Computing Roughwall Heat Transfer Rates on Reentry Nosetips, AIAA Paper No. 73-763, July 1973.

4. R. B. Dirling, Jr., Exploratory Development or Ablation MOdeling of Advanced Carbon-Carbon Composites, Fourth Quarterly Report, McDonnell Douglas Astronautics Company, Report MDC G4812, September 1973.

5. R. B. Dirling, Jr., C. E. Swain, and T. R. Stokes, The Effect of Transition and Boundary Layer Development on Hypersonic Reentry Shape Change, AIAA Paper No. 76-673, AIAA 10th Thermophysics Conference, Denver, Colorado, May 27-29, 1975.

6. T. J. Dahm, et al., Passive Nosetip Technology (PANT II) Program, Vol. I. Inviscid Flow and Heat Transfer Modeling for Reentry Vehicle Nosetips, SAMSO-TR-77-11, October 1976.

7. D. T. Hove and W. C. L. Shih, Reentry Vehicle Stagnation Region Heat-Transfer in Particle Environments, AIAA Journal, Vol. 15, No. 7, pps. 1002-1005, July 1977.

8. C. E. Swain, R. B. Dirling, Jr., and K. M. Kratsch, Erosion Mechanisms and Characterization of Graphitic Materials (U), AFML-TR-74-267, April 1975 (Secret).

9. J. C. Boison and H. A. Curtiss, An Experimental Investigation of Blunt Body Stagnation Point Velocity Gradient, ARS Journal, pps. 130-135, February 1959.

10. D. C. Reda, Correlation of Nosetip Boundary Layer Transition Data Measured in Ballistics-Range Experiments, AIAA Paper No. 80-0286, 18th Aerospace Sciences Meetings, Pasadena, California, January 1980.

11. A. D. Anderson, Analysis of PANT Series A Rough Wall Calorimeter Data. Aerotherm Report 73-81, Acurex Corporation, Mountain View, California, Part II, 1973.

12. E. R. VanDriest, C. B. Blumer, and C. S. Wells, Jr., Boundary-Layer Transition on Blunt Bodies - Effect of Roughness. AIAA Journal, Vol. 5, No. 10, pp. 1913-1915, October 1967.

13. Private Communication from D. C. Reda

14. D. C. Wilcox, Turbulence Model Transition Predictions: Effects of Surface Roughness and Pressure Gradient. AIAA Paper No. 75-857, 8th Fluid and Plasma Dynamics Conference, Hartford, Connecticut, June 1975.

15. R. B. Dirling, Jr., et al. Ablation/Erosion Evaluation of Reentry Vehicle Materials, Vol. I. Nosetip Materials. AFML-TR-76-2, McDonnell Douglas Astronautics Company, Huntington Beach, Ca., February 1976.

16. G. P. Johnson, C. L. Arne, and D. M. Yano, Maneuvering Reentry Control and Ablation Studies (MARCUS), Final Report, Vol. III (U), Report No. BSD-TR-65-312, July 1965 (S).

17. K. M. Kratsch, et al., Erosion Mechanisms and Improvement of Graphitic Materials, Vol. III, Hyperthermal Erosion Tests and Surface Roughness Characterization, Technical Report AFML-TR-70-307, Vol. II, June 1972.

18. R. B. Dirling, Jr., D. A. Eitman, and J. D. Binder, Evaluation of Post-Test Ablation Models, Technical Report AFML-TR-77-225, December 1977.

19. D. A. Eitman and J. E. DeMichaels, Performance Technology Program (PTP-S II), Vol. X, Material Characterization of Post-Test Ablation Models, BMO-TR-80-40, April 1980.

20. D. C. Reda, Measurements of Transition-front Asymmetries on Ablating Graphite Nosetips in Hypersonic Flight, AIAA J., Vol. 17, No. 11, pp. 1201-1207, November 1979.

21. R. B. Dirling, Jr., On the Relation Between Material Variability and Surface Roughness, AIAA Paper No. 77-402, 18th Structures, Structural Dynamics and Materials Conference, San Diego, California, March 1977.

22. E. W. Heinonen, and G. Y. Jumper, Jr., A Method for the Evaluation of Damage on the Surface of Carbon-Carbon Ablation Samples.

23. Reduced Data Report: ADCON-1/ANT-3 Nosetip Ablation Test Series in the AFWAL/AFFDL RENT 50 MW Arc Heater Facility, October 1977. Aerotherm Report TM-77-190, Project 7295.

24. AFML/SAMSO-ABRES 50 MW "June '75" Materials Screening Test Results, Acurex/Aerotherm.

25. Fine Weave Carbon/Carbon (FWCC) 50 MW Test Series, Preliminary Results Briefing, 20 September 1976, Acruex/Aerotherm.

26. SAMSO-ABRES Systems Test Missile (STM) Test Series in the AFFDL 50 MW Arc Facility, Reduced Ramp and Steady-State Test Data, May 1976, Acruex/Aerotherm.

27. D. W. Hall, C. L. Kyriss, and C. M. Dougherty, Performance Technology Program (PTP-SII), Vol. II, A Three- Dimensional Inviscid Blunt Body Code for Asymmetric Nosetips in Pitch and Yaw, SAMSO-TR-79-9, December 1978.

28. D. W. Hall, Performance Technology Program (PTP-SII), Vol. III, Invsicid Aerodynamics for Ballistic Reentry Vehicles with Ablated Nosetips, Final Report, BMO-TR-81-1, September 1979.

29. S. Taylor, et al., Performance Technology Program (PTP-SII), Vol. VII, Low Altitude Roll/Trim Dispersion Modeling for Ballistic Reentry Vehicles, Final Report, BMO-TR-to be published.

30. R. B. Dirling, Jr., Asymmetric Nosetip Shape Change During Atmospheric Entry, AIAA Paper No. 77-779, 12th Thermophysics Conference, Albuquerque, New Mexico, June 1977.

31. C. E. Swain, Aerodynamics of Reentry Vehicles with Asymmetric Nosetip Shape Change, AIAA Paper No. 77-782, 12th Thermophysics Conference, Albuqueque, New Mexico, June 1977.

32. A. M. Morrison, et al., Handbook of Inviscid Sphere-Cone Flow Fields and Pressure Distributions, NSWC/WOL/TR 75-45, December 1975.

DISTRIBUTION LIST

Ballistic Missile Office
BMO/SYDT
Attn: Maj. K. Yelmgren (2)
Norton AFB, CA 92409

Defense Technical Information Center (2)
Cameron Station
Alexandria, VA 22314

Air University Library
Maxwell AFB, AL 36112

TRW DSSG
Attn: W. Grabowsky (2)
P. O. Box 1310
San Bernardino, CA 92402

TRW Systems Group (2)
Attn: J. Ohrenberger
M. Gyetvay
1 Space Park
Redondo Beach, CA 92078

Headquarters, Arnold Engineering
Development Center
Arnold Air Force Station
Attn: Library/Documents
Tullahoma, TN 37389

Armament Development and Test Center
Attn: Technical Library, DLOSL
Eglin AFB, FL 32542

Air Force Wright Aeronautical Laboratories (3)
Air Force Systems Command
Attn: M. Buck (AFWAL/FIM)
R. Neumann (AFWAL/FIMG)
V. Dahlem (AFWAL/FIMG)
Wright-Patterson AFB, OH 45433

U. S. Army Ballistic Missile
Defense Agency/ATC-M
Attn: J. Papadopoulos
P. O. Box 1500
Huntsville, AL 35807

Director, Defense Nuclear Agency
Attn: J. Somers (SPAS)
Washington, DC 20305

Naval Surface Weapons Center
Attn: Carson Lyons/K06
White Oak Laboratories
Silver Spring, MD 20910

Acurex Aerotherm
Aerospace Systems Division
Attn: C. Nardo
485 Clyde Avenue
Mountain View, CA 94042

Avco Systems Division
Attn: N. Thyson
201 Lowell Street
Wilmington, Mass 01887

General Electric Company
Attn: R. Neff
3198 Chestnut Street
Philadelphia, PA 19101

Lockheed Missiles and Space Co.
P. O. Box 504
Attn: G. T. Chrusciel
Sunnyvale, CA 94086

McDonnell Douglas Astronautics Co.
Attn: J. Copper
5301 Bolsa Avenue
Huntington Beach, CA 92647

PDA Engineering
Attn: M. Sherman
1560 Brookhollow Drive
Santa Ana, CA 92705

Sandia Laboratories
P. O. Box 5800
Attn: Library
Albuquerque, NM 87115

Science Applications, Inc.
Attn: A. Martellucci
994 Old Eagle School Road
Suite 1018
Wayne, PA 19087


FILMEL
R-8